**UNIVERSITÀ DEGLI STUDI DI CATANIA**

**IN CONVENZIONE CON**

**UNIVERSITÀ DEGLI STUDI DI PALERMO**

---

**DOTTORATO DI RICERCA IN**

**SCIENZA DEI MATERIALI E NANOTECNOLOGIE - XXXIII CICLO**

---

GIOVANNI MAIRA

# FUNCTIONAL NEAR INFRARED SPECTROSCOPY OF HUMAN BRAIN TISSUES: STUDY OF MATERIALS, DEVICES AND SYSTEMS

TUTORS: DOTT. S. A. LOMBARDO, PROF.SSA M. G. GRIMALDI

COORDINATORE: PROF. G. COMPAGNINI

---

TESI PER IL CONSEGUIMENTO DEL TITOLO DI DOTTORE DI RICERCA

# Contents

# Introduction

Medical images of living tissues can be produced using any of the existing techniques such as CT (computed x-ray tomography), PET (Positron Emission Tomography), Ultrasound or MRI (Magnetic Resonance Imaging). All these techniques are powerful and have great advantages, but they suffer from some drawbacks limiting their use: CT and PET use ionizing radiations that are risky for health, while fMRI involves exposure to strong magnetic fields and induced electric fields, making it a contraindication in patients with implanted electronic devices (e.g., deep brain stimulators, pacemakers, and cochlear implants). Moreover, both the techniques are quite uncomfortable for the patient who is forced to lay within a small space. A continuous, non-invasive, portable and low cost medical monitoring cannot be based on these techniques.

Light is non-ionizing over many wavelengths and is known to function well as a medical probe. In particular, red and infrared light pass relatively easily through human tissues and structures as the skull, brain and breast, and is well tolerated in large doses.

Near-Infrared spectroscopy (NIRS) and diffuse optical tomography (DOT) are optical techniques that use near-infrared light to probe biological tissues. Near infrared light can penetrate deeply into tissues (some centimeters) and is sensitive to several tissue constituents. For this reason, NIRS techniques provide important physiological information on living tissues. Biological tissue is a complex random medium where light undergoes many scattering events, and its propagation is similar to a diffusion process. Although the interaction of near-infrared light with tissue is dominated by scattering effects (the distance between two subsequent scattering events is on the order of $\approx 100\ \mu m$), most of the physiological information is led by the absorption of chromophores like oxy- and deoxy-hemoglobin. Since biological tissues behave as a diffusive medium in the near-infrared spectral region, many applications in biomedical optics require an appropriate knowledge of photon migration through diffusive media.

The main challenge of NIRS and DOT is to achieve an accurate map of the optical properties (absorption and reduced scattering coefficients, used to reconstruct the molecular concentration of the chromophores involved in physiological and functional activities of the analyzed tissue) from measurements taken at the boundary of a target even in case of inhomogeneity of baseline optical parameters.

This work deals with the study and development of an optical medical diagnostic system for real-time monitoring of the human tissues oxygenation, using the fNIRS technique. The aim of this study is the deep knowledge of the light behaviour in different inhomogeneous scattering materials, in order to open the way for an extension of fNIRS and DOT techniques from human head to other areas of the human body, such as the chest, characterized by cavities similar to air gaps.

The two optical techniques are explained in chapter 1, which reports the physical principles involved in molecular concentration determination, the different approaches in light injection and collection, the geometrical configuration of the optical probes, and the physical, mathematical and computational aspects involved in tomographic images reconstruction carried out in DOT techniques.

In order to fully understand the behaviour of NIR light in scattering media, chapter 2 reports the main aspects of the Diffusion Theory and of the light transport occurring in case of heterogeneities, considering the spatial and temporal distribution of NIR photons when they are injected from the boundaries of a medium. Considerations on the construction of the model on which the "forward problem" of the DOT is based are also reported in this chapter.

In chapter 3, considering the state of the art, a recently developed category of photodetectors is presented, the Silicon Photomultiplier devices (SiPMs), capable to increase the portability and performances of fNIRS systems with the possibility of high-density light injection and collection probes. A flexible 6-channels Continuous Wave (CW) fNIRS system based on Silicon Photomultiplier is here presented and after the characterization of SiPMs performances and system SNR, the apparatus was compared through an in vivo experiment to a commercial system based on Laser Diodes, Photomultiplier Tubes (PMTs) and optical fibers.

Despite the very promising performances of SiPM in a fNIRS context, some artifacts have been observed in the output signals of the sensors, therefore a deep study of the SiPM issues and functioning characteristics consisting in afterpulsing effects, device transients, and the conditions to optimize the signal-to-noise ratio is presented in chapter 4.

In chapter 5 it is presented the activity on the fNIRS prototype system, that is the construction and characterization of a fiber-less optical system with 156 channels each one consisting of an optode made of a SiPM and a pair of LEDs operating at 700 nm and 830 nm. The system is intended for fNIRS and DOT imaging of the cortical activity of the human brain at frequencies above 1 Hz. Testing and system optimization are performed through measurements on a multi-layered optical

phantom with mechanically movable parts that simulate near-infrared light scattering inhomogeneities. The baseline optical characteristics of the phantom are carefully characterized by means of analytical and computational methods. Moreover, the behavior of NIR light traveling in inhomogeneous media with source and detector both placed on the medium surface has been studied by means of the Monte Carlo method. Such modeling was required to understand the photocurrent data as a function of time recorded during experiments performed on our dynamic phantom. For this purpose, a Monte Carlo simulation code has been realized. The simulations allowed in fact to understand the trends of the photodetector output signals as a function of time recorded on the dynamic phantom, as described in the chapter.

Furthermore, the chapter shows several technical aspects of the system development, such as LED light output drift and its possible compensation, SiPM linearity, corrections of channel signal differences, and signal-to-noise ratio (SNR).

Finally, an imaging algorithm that investigates large phantom regions is presented. The overall results demonstrate the high potentialities of a system based on SiPMs for fNIRS/DOT human tissues imaging applications.

# Chapter 1

# Biomedical Optical Techniques: functional Near Infrared Spectroscopy and Diffuse Optical Tomography

## *1.1 functional Near Infrared Spectroscopy (fNIRS)*

fNIRS is a neuroimaging technique for mapping the functioning of human brain cortex during normal activities by measuring hemodynamics related optical signals. This technology exploits the principles of near-infrared (NIR) spectroscopy (NIRS). Therefore, it is appropriate to start describing the main principles of NIRS.

The basics and main characteristics of NIRS can be summarized by 2 main principles:

1) human tissues are relatively transparent to light in the NIR spectral window (650 – 1000 nm);

2) NIR light is either absorbed by pigmented compounds (chromophores) or scattered in tissues;

From point 1 directly descends the fact that NIR light is able to penetrate human tissues, since the dominant factor in its tissue transport is scattering, which is typically about 100 times more probable than absorption [1].

Considering the point 2, it was seen that the relatively high attenuation of NIR light in tissues is due to the hemoglobin that is the main chromophore located in small vessels (< 1 mm in diameter) of the microcirculation, such as capillary, arteriolar and venular beds. The blood vessels >1 mm completely absorb the light.

Given the fact that arterial blood volume fraction is approximately 30% in humans brain [2], the NIRS technique offers the possibility to obtain information mainly concerning oxygenation changes occurring within the venous compartment.

The attenuation of NIR light in tissue is mainly due to the hemoglobin in its two molecular species, oxygenated ($O_2Hb$ or $HbO_2$) and de-oxygenated (HHb) hemoglobin.

The physical principle that allows us to quantify the two species of hemoglobin molecules by means of measuring the intensity of light is described by the Beer-Lambert's law. The Beer-Lambert's law relates the light attenuation, i.e. the ratio between the intensities of light transmitted and the light injected through a medium, with the material absorption coefficient. It can be expressed as:

$$\frac{I_1(\lambda)}{I_0(\lambda)} = e^{-\rho \cdot k_\lambda} \tag{1.1}$$

where $I_0$ is the known injected light intensity, $I_1$ is the transmitted light intensity, ϱ is the width of the medium, i.e. the light pathlength, and $k_\lambda$ is the attenuation coefficient of a the material, as illustrated by figure 1.1.

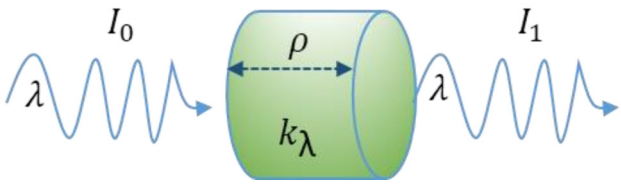


**Figure 1.1:** Graphical representation of the physical quantities involved in the Beer-Lambert law. The intensity of light decreases from $I_0$ to $I_1$ as it passes through a solution with attenuation coefficient $k_\lambda$ and length/thickness ϱ.

If the considered medium is a solution with two absorbing molecular species, the term $k_\lambda$ can be expressed as

$$k_\lambda = M_1 \cdot \varepsilon_{1,\lambda} + M_2 \cdot \varepsilon_{2,\lambda} \tag{1.2}$$

where $M_1$and $M_2$ are the molar concentrations of the first and the second molecular species respectively, while $\varepsilon_{1,\lambda}$ and $\varepsilon_{2,\lambda}$ are the wavelength-dependent molar absorption coefficients of the two molecular species. In short, the attenuation coefficient of a solution is the linear combination of the absorption coefficients of the abosrbing molecular species in the solution.

If in the considered medium the main absorbing species are two molecular species, as in the case of blood with oxy- and deoxy-hemoglobin, the equation 1.1 becomes:

$$ln\left(\frac{I_1(\lambda)}{I_0(\lambda)}\right) = -\rho \cdot \left(\varepsilon_{1,\lambda} \cdot M_1 + \varepsilon_{2,\lambda} \cdot M_2\right). \quad (1.3)$$

The term $ln\left(\frac{I_1(\lambda)}{I_0(\lambda)}\right)$ is the optical density, $\mathrm{OD}(\lambda)$.

The Beer-Lambert's law also applies in the case of scattering media. However, a measurement of the transmitted light is not possible in a configuration similar to the one shown in figure 1.1. In fNIRS, the light sources and the detectors are both positioned on the scalp and since the information comes from back-scattered photons, the light has not a straight path. Therefore a correcting factor has been considered in the equations. The differential pathlength factor (DPF) [3], depends on absorption, scattering and wavelength and is used to modify the Beer-Lambert's law in order to consider a banana shaped statistically probable path for the light from the source to the detector. By multiplying the DPF with the source – detector separation (SDS) measured on the scalp, the estimated pathlength of the light is considered in the equations and the Beer-Lambert's law is modified to be used in a back-scattering configuration [4].

Oxy and deoxy- hemoglobin have different absorption spectra. The two spectra cross each other in a particular point in NIR range, called "isosbestic point", approximately near 800 nm, as shown in figure 1.2.

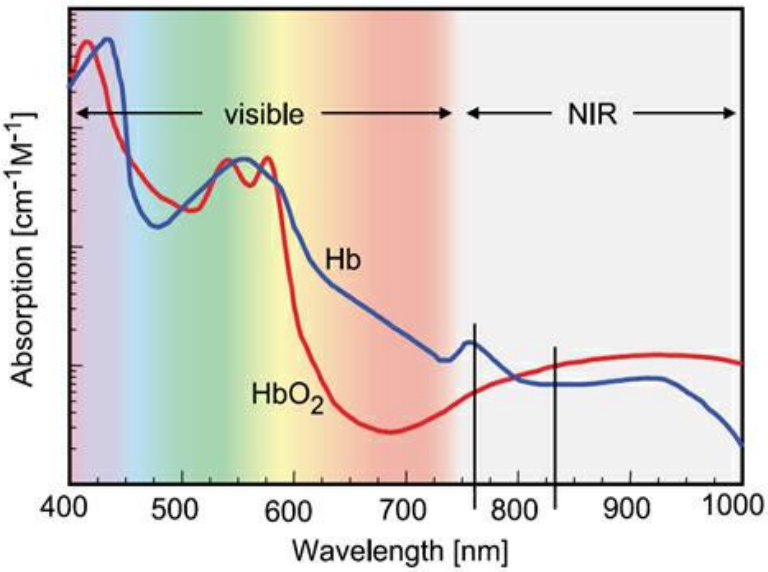


**Figure 1.2:** Absorption spectra of oxy- and deoxy-hemoglobin.

By the modified Beer-Lambert's law, the linear system in equation 1.4 can be defined and easily solved by choosing two different wavelengths straddling the isosbestic point:

$$\begin{bmatrix} O_2Hb(t) \\ HHb(t) \end{bmatrix} = \frac{1}{SDS} \begin{bmatrix} \varepsilon_{O_2Hb}(\lambda_1) \cdot DPF(\lambda_1) & \varepsilon_{HHb}(\lambda_1) \cdot DPF(\lambda_1) \\ \varepsilon_{O_2Hb}(\lambda_2) \cdot DPF(\lambda_2) & \varepsilon_{HHb}(\lambda_2) \cdot DPF(\lambda_2) \end{bmatrix}^{-1} \begin{bmatrix} OD(\lambda_1, t) \\ OD(\lambda_2, t) \end{bmatrix} \quad (1.4)$$

In this way it is possible to obtain the variation of the two molecular concentrations by solving, for each time instant *t*, a system of 2 equations and 2 unknowns if the optical density is measured at the two considered wavelengths. Further molecular species concentrations with known absorption coefficient can be obtained by adding further wavelengths in the NIR range. For example, Cytochrome c-oxidase, a large protein with an important role in ATP phosphorylation, has light absorption in the NIR range and can be detected by NIR measurements [5].

The SDS is a very important parameter in fNIRS context. The more SDS grows the deeper is the tissue under analysis but very sensitive photodetectors are required. Figure 1.3 shows the banana shaped statistical path of detected photons and how deep the detected light come from, depending on the SDS [6].

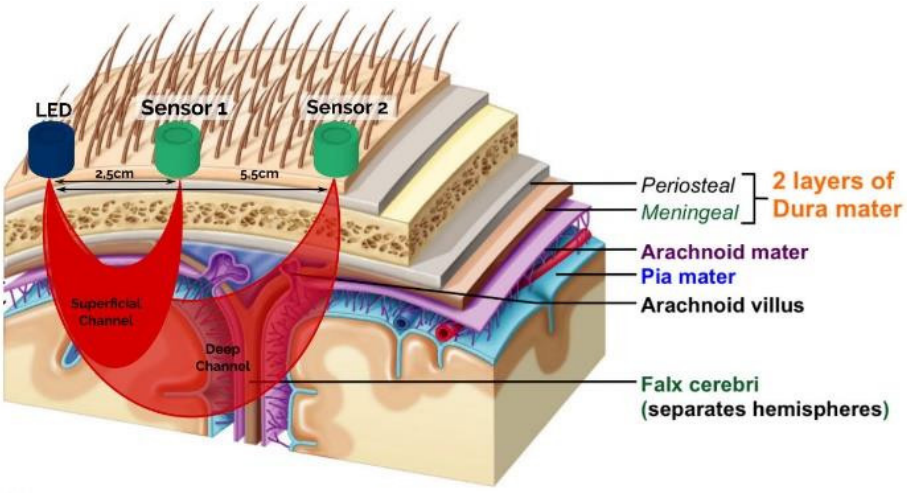


**Figure 1.3:** Banana shaped path of detected NIR light in scattering media.

However, the relation between SDS and depth of NIR analysis is a complex problem that will be addressed in the next chapters.

As mentioned before, it is possible to perform repeated and localized measurements of oxygenation of human cerebral cortex at different time instants.

In this way, the oxy- and deoxy-hemoglobin concentrations variation over time can be linked to cerebral activation or deactivation occurring during the functional activities of the brain. This technique is the functional NIRS, fNIRS.

In table 1.1. Ferrari and Quaresima [7] reported the overall chronology of the major events regarding the studies and the development of fNIRS and Diffuse Optical Tomography (DOT) techniques untill 2011.

**Table 1.1:** Overall chronology of the major events leading up to human functional cortical imaging by fNIRS [7]

| Year | Major Events |
|---|---|
| **1977** | • Jöbsis demonstrates the possibility to detect changes of adult cortical oxygenation during hyperventilation by near-infrared spectroscopy |
| **1985** | • First NIRS clinical studies on newborns and adult cerebrovascular patients (Brazy; Ferrari) |
| **1989** | • First commercial single-channel Continuous Wave clinical instrument: NIRO-1000 by Hamamatsu Photonics, Japan |
| **1992** | • First fNIRS studies carried out independently by Chance, Kato, Hoshi, and Villringer by using single-channel instruments |
| **1993** | • Publication of the first 6 fNIRS studies<br>• Simultaneous monitoring of different cortical areas by 5 single-channel instruments (Hoshi)<br>• First application of fNIRS on subjects affected by psychiatric disorders by using a single-channel system (Okada) |
| **1994** | • Hitachi company (Japan) introduces a 10-channel Continuous Wave system (Maki)<br>• First simultaneous recording of positron emission tomography and fNIRS data (Hoshi) |
| **1995** | • First evidence of a fast optical signal related to neuronal activity (Gratton)<br>• First two-dimensional image of the adult occipital cortex activation by a frequency domain spectrometer (Gratton) |
| **1996** | • First simultaneous recording of fMRI and Continuous Wave fNIRS data (Kleinschmidt)<br>• First simultaneous recording of fMRI and Time Resolved fNIRS data (Obrig) |
| **1998** | • First application of fNIRS on newborns using a commercial single-channel Continuous Wave system (Meek) |

| | |
|---|---|
| | • First images of the premature infant cortex upon motor stimulation by using a Continuous Wave -fNIRS prototype (Chance)<br>• First application of the Hitachi 10-channel system in clinics (Watanabe) |
| **1999** | • First introduction of a 64-channel Time Resolved system for adult optical tomography (Eda)<br>• First introduction of a 32-channel Time Resolved system for infant optical tomography (Hebden)<br>• First optical tomography Time Resolved images of the neonatal head (Benaron)<br>• Introduction of the first compact 8-channel Time Resolved system (Cubeddu)<br>• TechEn company (USA) starts to release its first fNIRS commercial system |
| **2000** | • Hitachi company starts to release its first commercial system: (ETG-100, 24 channels) |
| **2001** | • First fNIRS study using a single-channel Continuous Wave portable instrument and telemetry (Hoshi)<br>• Shimadzu company (Japan) starts to release its first commercial system: (OMM-2001, 42 channels)<br>• ISS Inc.(USA) starts to release the frequency domain system: Imagent (up to 128 channels)<br>• First three-dimensional Continuous Wave tomographic imaging of the brain (DYNOT, NIRx Medical Technologies, US) (Bluestone) |
| **2002** | • Hitachi company starts to release the ETG-7000 (68 channels) |
| **2003** | • Hitachi company starts to release the ETG-4000 (52 channels)<br>• Artinis company (The Netherlands) starts to release the Oxymon MkIII (up to 96 channels) |
| **2004** | • Shimadzu company (Japan) starts to release the NIRStation (64 channels)<br>• First simultaneous recording of DC-magnetoencephalography and Continuous Wave fNIRS data (Mackert) |
| **2005** | • Hitachi company starts to release the ETG-7100 (72 channels) |
| **2007** | • Shimadzu company starts to release the FOIRE-3000 (52 channels) |
| **2009** | • fNIR Devices company (USA) starts to release a wearable 16-channel system for adult PFC measurements<br>• Hitachi company starts to release a battery operated wearable/wireless 22-channel system for adult prefrontal cortex measurements |
| **2011** | • NIRx Medical Technologies company (USA) starts to release a battery operated wearable/wireless 256-channel system for adult frontal cortex measurements |

In recent years, the research and development groups involved in NIR optical techniques around the world focused their work on the possibility of extending the use of optical techniques and increasing their capabilities, usability and performances towards optical imaging and the development and optimization of Diffuse Optical Tomography.

Table 1.1. shows the development of different kinds of fNIRS techniques. The main fNIRS techinques are the Continuous Wave (CW-fNIRS), the Time Resolved or Time Domain (TR-fNIRS or TD-fNIRS). and the Frequency Domain (FD-fNIRS).

The three different NIRS techniques are based on a specific type of illumination:

1) the Contonuous Wave (CW) modality which, based on constant tissue illumination, simply measures light attenuation through the tissues;
2) the frequency-domain (FD) method which, illuminating the tissues with intensity-modulated light, measure both attenuation and phase delay of emerging light;
3) the time-domain (TD) technique which, illuminating with short pulses of light, detects the shape of the pulse after propagation through tissues in terms of photons arrival time.

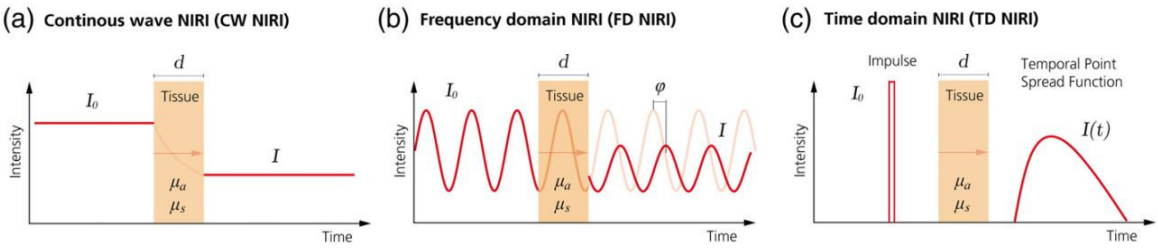


**Figure 1.4:** Illustration of the three different NIRI techniques. The continuous wave technology emits light at a constant intensity and then only measures the changes in the intensity of the light that passed through the tissue. The frequency domain technology modulates the emitted light intensity and then measured the intensity of the detected light as well as the phase shift, which corresponds to the time of flight. The time domain technology emits an extremely short pulse of light into the tissue and measures the arrival times of the photons that emerge from the tissue. This technology yields the highest amount of information, but it is also the most complex technology [8].

The quantitation of NIRS parameters depends on the NIRS technology adopted. The most commonly used CW-based NIRS instrumentation measures only oxygenation changes of $O_2Hb$ and HHb (with respect to an initial value arbitrarily set equal to zero) calculated using the above explained Beer-Lambert's law. In fact, the measurement of the injected light is not simple and, considering the optical

density formula, only the variations of the detected light can be recorded with sufficient precision.

The CW-based systems offer the advantages of low-cost and ease of transport. FD- and TD-based instruments increase in cost and technological complexity with the advantage of the possibility to absolutely characterize the optical properties of tissues (absorption and reduced scattering coefficients), from which it is possible to obtain absolute $O_2Hb$ and HHb concentrations.

This work deals with an absolute chracterization of diffusive media by means of TD techniques and Monte Carlo Simulations in order to optimize and validate a multichannel CW-fNIRS/DOT system.

Optical methods can be used to assess or monitor several neurological diseases manifesting as blood oxygenation related functional or metabolic alterations in the brain, including Alzheimer's disease [9], autism spectrum disorder [10], stroke [11], and multiple sclerosis [12]. Traditionally, brain function is imaged with positron emission tomography (PET) or with functional magnetic resonance imaging (fMRI). However, PET uses ionizing radiation, which is risky for health, while fMRI involves exposure to strong magnetic fields and induced electric fields, making it a contraindication in patients with implanted electronic devices (e.g. deep brain stimulators, pacemakers and cochlear implants). Moreover, both the techniques are quite uncomfortable for the patient who is forced to lay within a small space. Optical imaging is an alternative human brain mapping technique when both fMRI and PET are not indicated. Optical systems have, in principle, a much simpler hardware, therefore, they may be suitable for a more widespread use in medical care.

In NIR optical instrumentations the sources and the detectors are called "optodes". Traditionally, an optode consists of an optical fiber placed on the scalp and connected to the instrumentation for light injection and collection. The couple source-detector is the above mentioned "channel". It is important to note that a single source can be part of many channels, and viceversa a single detectors can be part of many channels, depending on the optodes location.

The number and the position of the optodes define the number of the channels of the system. The more channels the system si based on, the higher is the spatial definition of the optical instrumentation. Tipically, fNIRS measurements are recorded in particular anatomical references defined by the international 10-20 system, showed in figure 1.5, therefore the sources and detectors optodes have to be positioned so that the maximum sensitivity area of the source-detector couple intercepts these particular locations.

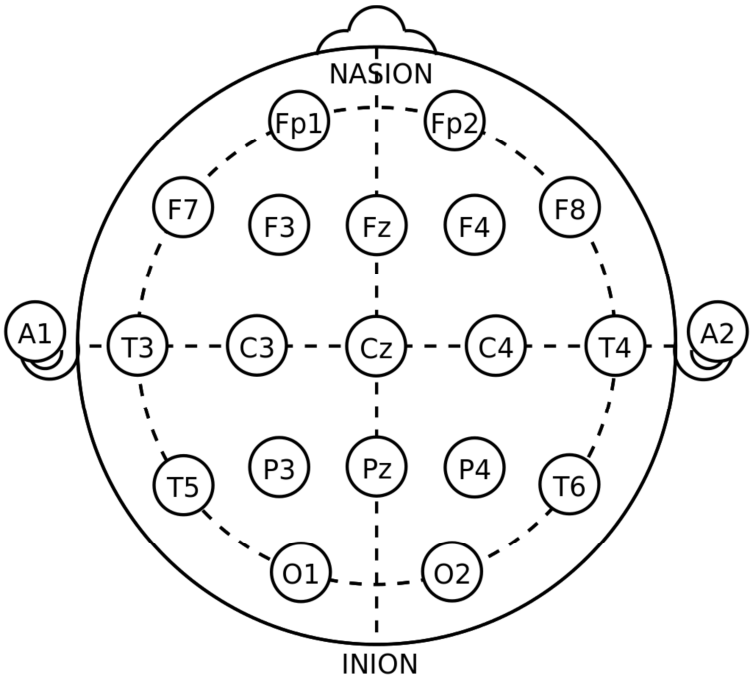


**Figure 1.5:** 10-20 system anatomical references.

## *1.2 Diffuse Optical Tomography (DOT)*

Traditional CW-fNIRS imaging instruments provide sparse arrangements of optodes with significantly lower spatial resolution than fMRI [13]. Sparse layouts of source-detectors are suitable to obtain functional traces rather than maps or images. However, recent developments in high-density diffuse optical tomography (HD-DOT) have broadened this perspective by providing a dramatically upgraded spatial resolution [14-17]. However, high-density arrays, particularly when covering a large portion of the head, present significant challenges in high-channel-count instrumentation, illumination interferences (separating signals detected from multiple sources), fiber-optic–scalp coupling, and lateral torqueing of the fibers.

Some recently developed systems are focused on solving these challenges through scalp-located semiconductor technology as it will be seen in the following chapters.

Since 1985 Simon Arridge (University College London) started his research work on diffuse optical tomography (DOT) for imaging the optical properties of biological tissue [18,19]. DOT operates by measuring light transmission through the body between many different points on the surface.

The high number of channels and the consequent high resolution is crucial, in fact the distribution of photons in the boundary measurements (CW-DOT), as well

as the temporal dispersion (TD-DOT) and spectral information (FD-DOT), can be used to reconstruct images of the internal distribution of optical absorption and scattering coefficients [20-22]. In other words, Optical Tomography is based on the general principle that a finite set of measurements of transmitted light between pairs of points on the surface of an object is sufficient to reconstruct a three-dimensional volume representing the distribution of internal scatterers and absorbers.

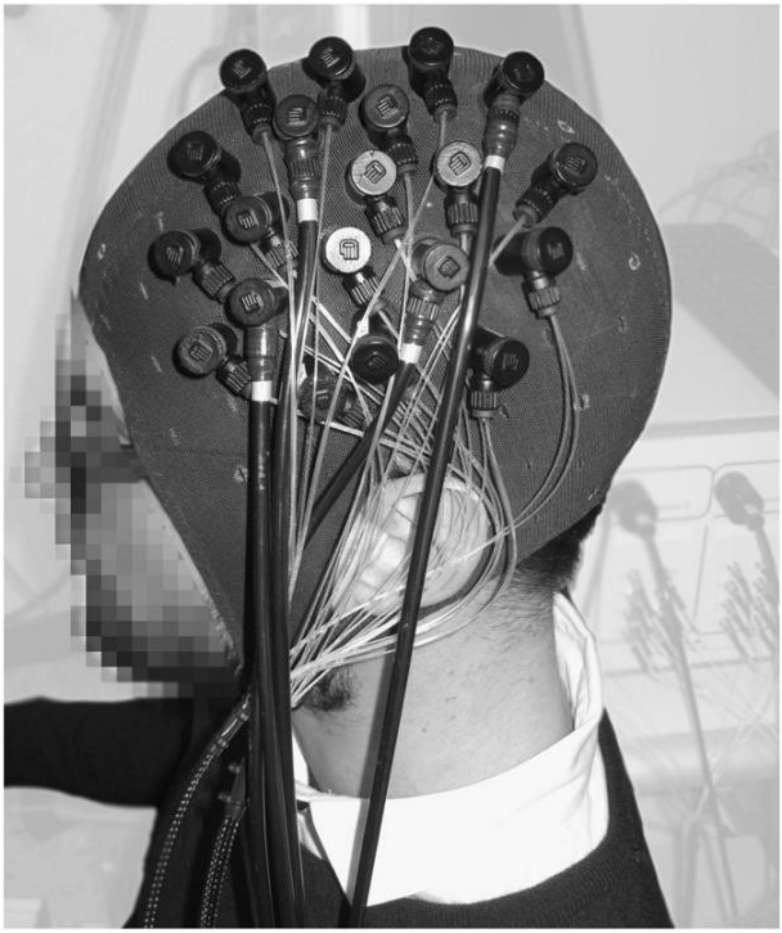

**Figure 1.6:** Example of an experimental probe developed at the University Zurich and ETH Zurich. Fiber holders are fixed in an EEG cap in order to transmit the light from the instrument to the head and back [8].

Therefore a typical DOT configuration is a matrix of optodes densely positioned on the surface of the medium under analysis, typically, the human head. In figure 1.6 is reported a photograph of a volunteer wearing an experimental high density optodes DOT probe develped by Zurich University and ETH Zurich [8].

DOT is generally recognized as a nonlinear inverse problem. A physically accurate model describing the progress of photons from the source optodes through the media and to the detector optodes, has to be constructed. This process is termed

the "forward problem". The definition of the forward problem will be discussed in the next chapter, however, considering a volume divided into small sub-volumes called *voxels*, the forward problem is the determination of a sensitivity matrix, the Jacobian matrix $A$, to put in relation the measured data of each channel ($y$ vector) with localized variations in optical parameters of the considered voxel in the volume of a medium:

$$y = Ax \tag{1.1}$$

where $x$ is the vector containing the optical parameter variations in each voxel and $y$ is the vector of the channels measurement. The size $m$ of vector $x$ is equal to the number of voxels forming the considered volume, while the size $n$ of the vector $y$ is evidently equal to the number of channels. The number of voxels is normally greater than the number of channels, therefore the matrix $A$ is a $n \times m$ generally non-square matrix, with $m >> n$. Clearly, a large number of measurements and consequently a larger $n$, means a larger number of equations in the system in equation 1.1, balancing the difference between the number of unknowns and the number of equations. This is not the only reason why a system having numerous channels is beneficial: the region covered by the matrix of sources and detectors can be wider, extending the total area under analysis, the spatial definition can be larger and if the sensitivity of the used sensors is appropriate, a large number of overlapping measurements can be collected, in which a detector may be required to measure signals from nearby and far sources simultaneously. Overlapping measurements have a crucial role in increasing the vertical spatial resolution and in the precision on localization of absorbing and scattering inhomogeneities, both in time domain [23, 24] and continuous wave [25].

The localization capabilities of DOT techniques are strongly linked to the physical modeling and mathematical approach in solving the inverse problem [26].

Generally, a problem with this logic, i.e. knowing the behavior of photons to define the matrix and then inverting it to know the localized optical properties, is that, in principle, this sensitivity matrix can change depending on the variations in absorption and scattering observed at each location of the medium. Thus, solving the forward problem requires knowing the solution to the inverse problem and vice versa. This issue can be overcome by assuming that, in the material under analysis, the absorption and scattering variations are incremental. This is what happens in human head, having variations of about 5% on optical parameters, therefore the

DOT techniques are taking increasing interest in the last years. In fact, under this hypothesis, it is possible to define the matrix $A$ considering the baseline optical properties of the medium, with a linearization of the problem.

Finding the vector x is not simple when the matrix A is not invertible. Moreover, the problem is "ill-posed" since, even when knowing the forward solution and the sensitivity matrix, the estimation of a large number of values inside the medium from a relatively small number of locations on the surface generate significant issues.

If the considered medium has baseline $\mu_s' \gg \mu_a$, in case of CW measurements, the equation 1.1 can be rewritten as:

$$\Delta OD = A_{[\mu_a(\vec{r}),\mu_s'(\vec{r})]}\Delta\mu_a(\vec{r}) \tag{1.2}$$

where $\Delta OD$ is the change in optical density due to a local variation in absorption $\Delta\mu_a(\vec{r})$ for each channel. The term $\Delta\mu_a(\vec{r})$ is a vector of absorption perturbations for each location, $A_{[\mu_a(\vec{r}),\mu_s'(\vec{r})]}$ is the rectangular Jacobian matrix depending on baseline optical parameters, optodes, and voxel locations defining the vector $\vec{r}$.

The inverse problem requires solving equation 1.2 for $\Delta\mu_a(\vec{r})$ based on a known $\Delta OD$ and $A$ (the Jacobian matrix). However, $A$ is generally not square, and therefore cannot be inverted.

In order to provide a unique and stable solution to the inverse form of equation 1.2, the Tikhonov regularization technique [27] the most common procedure employed. The vector $\Delta\mu_a$ of solutions can be obtained by solving the equation 1.3:

$$A^T(AA^T + \varepsilon I)^{-1}\Delta OD = \Delta\mu_a \tag{1.3}$$

where $I$ is the identity matrix and $\varepsilon$ is the Tikhonov regularization parameter, a positive element added to the diagonal of the matrix $AA^T$ in order to invert it. It is demonstrated that the found solution $\Delta\mu_a$ is the solution to the least square problem in equation 1.4:

$$O[\Delta\mu_a]A = ||A\,\Delta\mu_a - \Delta OD||^2 + \varepsilon\,||\Delta\mu_a\,||^2 \tag{1.4}$$

where $O[\Delta\mu_a]$ is the function to be minimized [26].

The two techniques above presented, fNIRS and DOT, are able to estimate the optical parameters variations linked to the variations in concentration of molecular species essential to normal vital functions, especially those linked to hemodynamic phenomena in soft tissues, i.e. cerebral cortex or breast. The fNIRS technique is capable of collecting traces of hemodynamic changes in localized areas near the surface. DOT technique enhances the capabilities of fNIRS by introducing the possibility of a 3D reconstruction of the optical parameter distribution in the volume under analysis.

Despite the recent evolutions in the field of optical instrumentation, there are still critical issues related to the sensitivity and portability of the systems. In the recent past, it always be chosen a tradeoff between portability and sensitivity and precision. Moreover, as mentioned above, the optical instrumentation usability is confined to soft, approximatively homogeneous tissues.

In this work, these issues are analyzed and addressed. In the next chapters, the theory underlying the scattering of light in homogeneous and non-homogeneous media is discussed, and a particular category of solid-state photodetectors is studied, analyzing their capability of overcoming the compromise between portability and sensitivity in the NIR range.

A fiber-less prototype of a multichannel optical system has been built and presented in the concluding chapters of this work. It is able to manage 156 channels each one operating in CW at 700 nm and 830 nm, by the use of the above mentioned solid state high sensitivity photodetectors. The system has been validated on a multilayered inhomogeneous optical phantom with an air gap and mechanically movable parts that simulated near infrared light scattering inhomogeneities. The signals have been predicted after an accurate optical characterization of the inhomogeneous phantom and a number of Monte Carlo simulation taking into account the air gap characterizing the phantom.

The optical definition of non-homogeneous materials, especially if characterized by an air gap, allows us to trace the way to extend the use of optical techniques to the inhomogeneous diffusive materials characterization.

Moreover the techniques based on the use of light in NIR range can be used to monitor other areas of the human body, such as the chest, helping in pathologies assessment or in therapies monitoring.

# Chapter 2

# Diffuse Light Transport: applications in CW - Diffuse Optical Tomography context

## *2.1 Optical Properties, Fluence rate, concentration of optical energy and transport function*

Light diffusion is well described by a more general transport theory. Such transport theory concerns the transport of particles through a background medium and is used in several applications, such as neutron transport in nuclear reactors, penetration of light through the atmosphere, diffusion of molecules in gases, diffusion of holes and electrons in semiconductors, and, as in the present case, photon transport through high scattering medium or biological tissues.

Despite the different kinds of particles (neutrons, gas molecules, electrons, photons) that may be involved in the transport processes, all these phenomena can be studied and described by using the same basic equation. When the transport process becomes diffusive, the transport equation can be simplified through the diffusion equation. Given a physical quantity $u$ representative of the physical process studied (for instance, the particle density), $u$ is described by the equation:

$$\frac{\partial}{\partial t}u(\vec{r},t) - k_1\nabla^2 u(\vec{r},t) + k_2\, u(\vec{r},t) = q_0(\vec{r},t) \tag{2.1}$$

The coefficient $k_1$ is related to the spatial and temporal scale of the diffusive phenomenon studied, and the coefficient $k_2$ is related to the probability that the transported particles will be absorbed. For neutron transport processes, $k_1$ will be related to the transport coefficient of neutrons through the medium. For the diffusion of electrons and holes in semiconductors, $k_1$ will be related to the electrical conductivity. For the diffusion of molecules in gases, $k_1$ will be related to the transport coefficient of the molecules through the gas [28].

In this work, $u$ represents the concentration of optical energy C [J/cm$^3$], $k_1$ will be related to the transport coefficient or diffusion coefficient of photons through the medium and both $k_1$ and $k_2$ are wavelength dependent coefficients. The term $q_0$ is

the source of particles. In discussing light transport in diffusion theory, some parameters and properties have to be defined and taken into consideration: they are summarized in tables 2.1, 2.2 and 2.3.

**Table 2.1**: medium optical properties.

| Quantity | Symbol | Units |
|---|---|---|
| Absorption coefficient | $\mu_a$ | $cm^{-1}$ |
| Scattering coefficient | $\mu_s$ | $cm^{-1}$ |
| Anisotropy of scattering | $g$ | Dimensionless |
| Refractive index | $n$ | Dimensionless |

**Table 2.2:** Transport properties used in diffusion theory.

| Quantity | Symbol | Units |
|---|---|---|
| Reduced scattering coefficient | $\mu_s' = \mu_s(1-g)$ | $cm^{-1}$ |
| Transport mean free path | $MFP' = 1/(\mu_a + \mu_s')$ | cm |
| Diffusion length | $D = MFP'/3 = 1/3(\mu_a + \mu_s')$ | cm |
| Optical penetration length | $\delta = \sqrt{D/\mu_a}$ | cm |
| Extinction Coefficient | $\mu_t = \mu_a + \mu_s$ | $cm^{-1}$ |
| Effective attenuation coefficient | $\mu_{eff} = \sqrt{3\,\mu_a\,\mu_s'} = \sqrt{\mu_a/D} = 1/\delta$ | $cm^{-1}$ |

**Table 2.3:** Parameters for light transport.

| Quantity | Symbol | Units |
|---|---|---|
| Radiant Power | $P$ | W, W/cm, $W/cm^2$ |
| Radiant Energy | $Q$ | J |
| Transport | $T$ | $cm^{-2}$, $cm^{-1}$, dimensionless |
| Fluence rate | $\varphi = PT$ | $W/cm^2$ |
| Fluence | $\psi = QT$ | $J/cm^2$ |
| Speed of light in the medium | $c = c_0/n$ | cm/s |
| Concentration of radiant energy | $C = \varphi/c$ | $J/cm^3$ |

The fluence rate $\varphi$ [$W/cm^2$] is defined as the total number of photons incident from all directions on a small sphere divided by the cross-sectional area of the sphere. It is proportional to the concentration of optical energy C [$J/cm^3$]:

$$\varphi = c\,C, \tag{2.2}$$

Where $c$ is the speed of light in the medium, $c = c_0 / n$ [cm/s], $c_0 = 2.998 \times 10^{10}$ cm/s, and $n$ is the refractive index of the medium.

Fluence rate can be regarded as a measure of concentration, and the diffusion of light as the movement of photons down concentration gradients. This gradient-

driven movement of light is described by the Fick's first law of diffusion, in which the flux $J$ [W/cm$^2$] down a concentration gradient $\partial C/\partial x$ [(J/cm$^3$)/cm] is:

$$J = -\chi\frac{\partial C}{\partial x} = -cD\,\frac{\partial C}{\partial x} = -D\,\frac{\partial \varphi}{\partial x} \tag{2.3}$$

Where $\chi$ is the diffusivity [cm$^2$/s] equal to $cD$ for light, with the diffusion length related to the transport mean free path (MFP') by the relation D = MFP'/3 [cm]. MFP' is the mean distance traveled by a photon before a scattering or absorption event. Considering a small incremental window of cross sectional area $dA$. The flux of light through the window is due to the scatter of light from two small hemispherical regions on either side of the window which scatter light thorough the window from both directions. For this example, isotropic scatterers are assumed, described by the reduced scattering coefficient $\mu_s'$ [cm$^{-1}$]. The reduced scattering coefficient is a lumped property incorporating the scattering coefficient $\mu_s$ and the anisotropy $g$. The purpose of $\mu_s'$ is to describe the diffusion of photons in a random walk of step size of $1/\mu_s'$ [cm] where each step involves isotropic scattering. Such a description is equivalent to description of photon movement using many small steps $1/\mu_s$ that each involve only a partial deflection angle $\theta$ if there are many scattering events before an absorption event, and $g$ is defined as the cosine of the average deflection angle, $g = \langle\cos\theta\rangle$. [29]

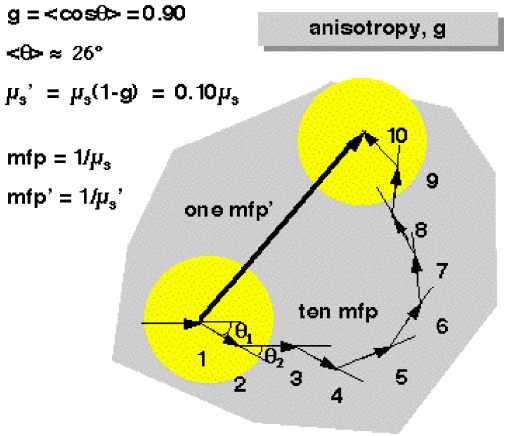


**Figure 2.2:** steps involving an isotropic scattering are equivalent to many small anisotropic steps [2].
MFP and MFP' are evaluated in the case of $\mu_a = 0$.

Light scattering originates from the interaction of photons with structural heterogeneities present inside material bodies at the wavelength scale. Therefore,

the optical properties of a material are wavelength dependent. The interaction between a photon and a molecule results in a photon moving in a different direction and a molecule that may maintain, increase, or decrease its energy. If the energy of the scattered photon is the same as the incident photon, the photon-molecule interaction is denoted as elastic scattering; while if the energy of the scattered photon is lower or higher than the incident photon, the interaction is denoted as inelastic scattering. Rayleigh scattering is an example of elastic scattering, which occurs when light propagates through gases, while Raman scattering is an example of inelastic scattering [28]. In this work, only elastic scattering is considered.

Since the photon flux of the diffusive phenomenon is related to concentration gradient, we can consider C:

$$C = \frac{\varphi}{c} = \frac{n\,\varphi}{c_0} \tag{2.4}$$

as the physical quantity representative of the diffusion process described by the equation (2.1).

The generic solution to the time resolved diffusion equation, for diffusion from a point source in both space and time is:

$$C(r,t) = Q\frac{\exp[-r^2/(4\chi t)]}{(4\pi\chi t)^{3/2}}, \tag{2.5}$$

where Q is the point source of photons, placed at r = 0 and at time t = 0. The second factor is a Green's function and it has units of $cm^{-3}$ hence, the concentration C at a distance r at a time t after the initial deposition of Q as an impulse, is expressed in [units/cm3]. Substituting the (2.4) in the (2.5) and replacing the diffusivity $\chi$ with cD, the fluence rate $\varphi(r,t)$ is obtained as expressed by the equation (2.6). The role of absorption is added by including the term $\exp(-\mu_a ct)$ where ct is the pathlength of photons at time t, and $\mu_a$ is the absorption coefficient [$cm^{-1}$]:

$$\varphi(r,t) = cQ\frac{\exp[-r^2/(4cDt)]}{(4\pi cDt)^{3/2}}\exp(-\mu_a ct). \tag{2.6}$$

This is the time resolved 3D diffusion equation for light in a medium with scattering and absorption. By integrating equation (2.6) over all time, the time-invariant radiant exposure $\psi$(r) (fluence) is obtained:

$$\psi(r) = \int_{t=0}^{\infty} \varphi(r,t)dt = Q\ \frac{\exp(-r/\delta)}{4\pi Dr}. \tag{2.7}$$

The integration is not straightforward, but becomes easier by considering conservation of energy [30]. The factor $1/\delta$ is called "effective attenuation coefficient" $\mu_{eff}$ [cm$^{-1}$]. The expression confirms the intuition that indicates that $\psi$ falls exponentially with distance from a source: it is the impulse response of radiant exposure to an impulse of energy deposition $Q$ [J]. The factor $\delta$ is called "penetration depth" [cm], a measure of how deep the light can penetrate into a material. This factor is not simple to obtain, since it depends on wavelenght, power and beam width of the irradiant wave, expecially in inhomogeneous materials or in multilaiered tissues [31]. In the case of homogeneous materials and single wavelenght point light source, it can be expressed in function of scattering and absorption as in table 2.2 as $\delta = \sqrt{D/\mu_a}$, where $D$, is the above mentioned diffusion length that can be expressed as $1/3(\mu_a + \mu_s')$.

The radiant power $P$ averaged over time of a repetitive sequence of impulses is: $P = fQ$ [W], where $f$ is the repetition frequency. In the limit of $f \to \infty$ and $Q \to 0$, $P$ is the expression of a radiant power with a constant average. The time-resolved impulse response $\varphi(r,t)$ becomes a steady-state fluence rate proportional to $\psi(r)$:

$$\varphi(r) = P\ \frac{\exp(-r/\delta)}{4\pi Dr}. \tag{2.8}$$

$P$ replaces $Q$ and the equation (2.8) describes the steady-state diffusion of light from a point source of radiant power P. The transport factor $T$ is defined as $\varphi/P$ and characterizes the light transport in a medium independent of the strength of the source. For a 3D spherical diffusion from a point source, the light transport is:

$$T_{sph}(r) = \frac{\exp(-r/\delta)}{4\pi Dr} = \quad 3(\mu_a + \mu_s')\frac{\exp\left[-\frac{r}{\sqrt{1/3\mu_a(\mu_a + \mu_s')}}\right]}{4\pi r} \tag{2.9}$$

## *2.2 Heterogeneities: the Perturbation Method*

A transport function as the (2.9) can be applied to assess the influence of a perturbing object within a medium. Such perturbing object has an influence on a distant point of observation and the steady-state diffusion equation can be used to

localize it and to evaluate its different absorption and/or scattering properties with respect to the background optical properties of the medium.

Figure 2.2 shows an absorbing object perturbing the field of light from a source to a detector [30]. The inhomogeneity of volume V has an incremental absorption $\Delta\mu_a$ above the background medium optical properties, but the same scattering properties as the background medium.

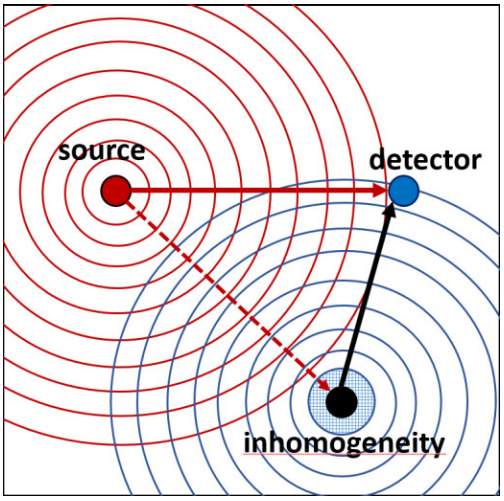


**Figure 2.2:** Light source, light detector and an inhomogeneity in a medium with background optical properties $\mu_{a0}$ and $\mu'_{s0}$. The perturbing object causes an incremental absorption $\Delta\mu_a$ with respect to the background properties [30].

Under these assumptions, if a power of light is launched isotropically by a light source at a position $x_s, y_s, z_s$, the transport to a detector at position $x_d, y_d, z_d$ is

$$T_{s\to d} = \frac{\exp(-r_{s\to d}/\delta)}{4\pi D r_{s\to d}} \tag{2.10}$$

where $r_{s\to d}$ is the source – detector distance.

The background optical properties are $\mu_{a0}$ and $\mu'_{s0}$, therefore the background diffusion constant and the background penetration depth are respectively $D = 1/3(\mu_{a0} + \mu'_{s0})$ and $\delta = \sqrt{D/\mu_{a0}}$.

At the inhomogeneity location $x_p, y_p, z_p$, the fluence rate is $\varphi_{obj} = PT_{s\to p}$, where P is the power of light injected in the medium from the source, and $T_{s\to p}$ is calculated by using the source – object distance in the equation (2.10). The extra energy dissipated by the absorbing inhomogeneity of volume V is the portion of fluence rate $\Delta\mu_a\varphi_{obj}$ and the total extra power is $\Delta\mu_a\varphi_{obj}V$ [W]. Since the optical energy is dissipated by the inhomogeneity, the object in the medium acts as a negative power source $P_p = -\Delta\mu_a\varphi_{obj}V$ propagating in a spherical symmetric manner in the

medium and reaching the detector. Therefore, the fluence rate at the detector can be expressed as:

$$\varphi_d = PT_{s\to d} + P_p T_{p\to d} = PT_{s\to d} - \Delta\mu_a \varphi_{obj} V T_{p\to d} \\ = P(T_{s\to d} - \Delta\mu_a V\, T_{s\to p} T_{p\to d}). \tag{2.11}$$

The first term on the right is always positive while the second term is negative if $\Delta\mu_a > 0$, and positive if $\Delta\mu_a < 0$, thus the perturbation is positive.

The application of perturbation method is very important in Diffuse Optical Tomography (DOT) applications as explained in the following sections.

## *2.3 Evaluation of medium material background optical properties by the combination of the steady-state transport equation and time of flight measurements (TOF).*

The Diffusion Theory provides the basic equations useful to evaluate the wavelength dependent optical properties $\mu_{a0}(\lambda)$ and $\mu'_{s0}(\lambda)$ of a material under the assumption $\mu'_{s0}(\lambda)/\mu_{a0}(\lambda) > 10 \div 20$, that is, on average, a high number of scattering events occurs before the absorption event at the considered wavelength $\lambda$ takes place.

A point light source of given wavelength and a photodetector are placed in a medium and continuous wave measurements of the detector photocurrent are performed at different source-detector distances. By fitting a number of the measured photocurrents with the equation (2.9), the effective attenuation coefficient $\mu_{eff} = 1/\delta = \sqrt{3\,\mu_a\,\mu'_s}$ or the factor $3\mu_a(\mu_a + \mu'_s)$ can be calculated, since the transport equation (2.9) is a decreasing exponential function of the source detector distance. The effective attenuation coefficient $\mu_{eff}(\lambda)$ and the diffusion length $D(\lambda)$ quantify the combined effect of both absorption and scattering.

However, to evaluate $\mu_a(\lambda)$ and $\mu'_s(\lambda)$ separately, time of flight measurement have to be performed. This is evident as we consider the time dependent equations. In fact, the solution of the equation (2.1), fixed a distance from the point light source $r$, is a time dependent Green function $g(t)$, expressing the time response to an impulse of light of a given wavelength. From the point of view of an optical spectroscopy of a material, the most important characteristic of $g(t)$ is the mean time delay defined as:

$$< t > = \int_{-\infty}^{+\infty} g(t)\, t\, dt \Big/ \int_{-\infty}^{+\infty} g(t)\, dt\,. \tag{2.12}$$

Arridge et al. [32] showed that for a point source and point detector separated by a distance $r$ in a semi-infinite homogeneous diffusing medium (where $r \gg 1/\mu_s'$ and $\mu_s' \gg \mu_a$), the average flight time of photons $< t >$ is expressed as:

$$< t > = \frac{r^2}{2(\gamma^2 + r\gamma\sqrt{c\,\mu_a})} \tag{2.13}$$

where $c$ is the velocity of light in the medium and $\gamma$ is:

$$\gamma = cD = \frac{c}{3(\mu_a + \mu_s')}. \tag{2.14}$$

The equations 2.13 and 2.14 are very important in optical characterization of materials. By using these equations and Time-correlated single photon counting measurements (TCSPC) it is possible to establish a relation between the average time of flight of photons at a certain wavelength and the optical characteristics of the medium in which photons travel. Equations 2.13, 2.14, and 2.9 can be compared to a set of experimental data consisting of (a) steady-state reflectivity data vs. source-detector distance (predicted by equation 2.9), and (b) average time-of-flight vs. source-detector distance (predicted by equations 2.13 and 2.14). From such comparison it is possible to extract the optical parameters of a homogeneus medium by fitting the data to the theoretical trends.

## *2.4 Light transport in Diffuse Optical Tomography*

In section 2.2 of this chapter, the perturbation method has been presented. The equation 2.11, reported below, represents one of the theoretical basis in the context of diffuse optical tomography.

$$\varphi_d = PT_{s\to d} + P_p T_{p\to d} = P(T_{s\to d} - \Delta\mu_a V\, T_{s\to p} T_{p\to d}). \tag{2.11}$$

Considering a homogeneus medium divided into small volumes (*voxels*) with incremental absorption variations, the equation states that the contribute of a voxel to the variation of the fluence rate from a light source to a detector is given by the

product of the two light transport coefficients (from the source to the voxel and from the voxel to the detector), multiplied by the absorption variation and the volume of the considered voxel.

In the DOT context, the forward problem is the determination of a Jacobian matrix $A$ to put in relation the measured data ($y$ vector) with localized variations in optical parameters of the considered volume of a medium respecting certain assumptions:

$$y = Ax \tag{2.15}$$

where $x$ is the vector containing the optical parameter variations in each voxel determining the variations in the CW measurements contained in $y$. The size $m$ of vector $x$ is equal to the number of voxels forming the considered volume, while the size $n$ of the vector $y$ is equal to the number of measurements, i.e. the number of valid channels, i.e. the source-detector couples giving valid measurements. Therefore, the matrix $A$ is a $n \times m$ generally non-square matrix, with $m >> n$.

If the considered volume of the medium is homogeneus, far from the boundaries, and the scattering dominates over the absorption, the matrix $A$ can be built from the second term of the equation 2.11 for each of the source-detector couples of the DOT system and for each of the voxels of the considered region of the medium.

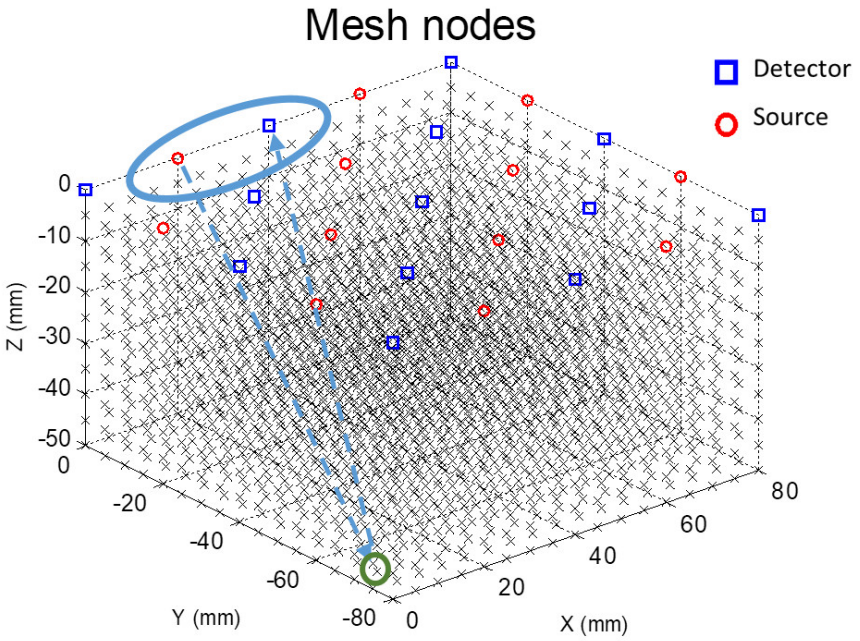


**Figure 2.9**: Mesh nodes defined for a 80 × 80 × 50 cm³ volume. Each node is the center of a *voxel*. The blue circle indicates a particular source-detector couple related to one of the measurements of the set. The green circle indicates a particular voxel located in $p$. Dashed blue arrows indicate the distances to obtain the light transports $T_{s\to p}$ and $T_{p\to d}$.

The figure 2.9 shows the mesh nodes defined for a 80 × 80 × 50 mm$^3$ volume. Each node is the center of a *voxel*. The sources and the detectors of a DOT system are represented as red circles and blue squares respectively. As mentioned before, the $A$ matrix is a jacobian, and each element of the matrix links a change in the amplitude of the measured photocurrent at the boundaries with a change in absorption coeffcient in a voxel. Therefore, if the aim of the experiment is to obtain the local variation of the absorption coefficient $\mu_a$, each element of the matrix is defined as:

$$a_{i,j} = \frac{\partial}{\partial \mu_{ai}} I_j \tag{2.16}$$

where $I_j$ is the intensity of the photocurrent obtained by the j-th measurement of the system and $\partial \mu_{ai}$ is the absorption variation in the i-th voxel. The element $a_{i,j}$ can be calculated considering the adjoint method [33], and since the photocurrent intensity is related to the light transport expressed in the equation 2.11, and deriving the term $-\Delta \mu_a V\, T_{s\to p} T_{p\to d}$ with respect to $\mu_{ai}$ at the i-th voxel, the term $a_{i,j}$ is given by the

$$a_{i,j} = -T_{s\to p} T_{p\to d} \tag{2.17}$$

and, since the medium is homogeneus, assuming the reciprocity principle within the adjoint method the terms $T_{s\to p}$ and $T_{p\to d}$ can be calculated by the equation 2.10, as explained in section 2.2.

The analytical method is extremely useful for a basic understanding of the image formation process (formally, to calculate the $y$ vector of the photodetector response corresponding to the $x$ vector of the variations of absorption in the voxels). However, such approach is not usable when the characteristics of the region under analysis are highly heterogeneous, and when large part of the volume under study has a light transport which is not light diffusion dominated. In such a case, instead, the Monte Carlo simulation can provide a much more correct method for specifying in a single framework (a) the motion of ballistic photons [34], (b) of photon diffusion in highly scattering media, and (c), to take into account reflection, refraction, total internal reflection, etc. at the interfaces between the various materials. In short, MC is much more suitable to treat the case of photon transport in hetereogeneous media.

In fact, Monte Carlo methods are also adopted to construct the Jacobian even in the case of a homogeneous medium. This is in particular the case of very short distances, that is, when the Diffusion Theory and the Monte Carlo simulations differ by one MFP' near the source [30]. Conventional adjoint Monte Carlo method typically compute the Jacobian by multiplying the photon density fields radiated from the source and from the detector at the considered wavelength assuming that the source and the detector in Green's function are reciprocal.

In this work a 13 detectors – 12 double wavelength sources DOT system has been built, using Silicon Photomultipliers. The prototype is presented in chapter 5. The spatial resolution of a DOT system depends on the number of valid measurments with different SDSs that can be overlapped. Since the silicon photomultipliers are capable to detect photons even at high SDS, a large number of overlapping measurements can be collected and the spatial resolution of the system is remarcable. In the case of homogeneus media with known background $\mu_s'$ and $\mu_a$ coefficients, a software has been developed in MATLAB®, using the analytical method to calculate and invert the matrix $A$. As it will be discussed in Chapter 5, this method is not applicable in case of inhomogeneous media characterized by high variations in optical parameters .

# Chapter 3

# Silicon Photomultiplier devices as detectors in CW-functional Near Infrared Spectroscopy: in vivo validation of a prototype

Diffuse Optical Tomography and functional Near Iinfrared Spectroscopy measurements on the human tissues are tipically performed by placing optical fibers on the skin for optical signal delivery and collection. Optical fibers are then connected to NIR sources and photodetectors. Optical fibers are useful since they can be used to electrically isolate the subject, or whenever the fNIRS instrument is cumbersome and must be placed at a certain distance. However, optical fibers introduce constraints to fNIRS. When employing optical fibers, it is difficult to keep a stable optode to scalp coupling and to dampen the effect of movement artifacts and ambient light. Moreover, a high number of fibers [35] make difficoult the fNIRS measurements reducing flexibility and often restricting the use of this technique to a laboratory environment. Moreover, the PMTs used in couple with optical fibers are extremely delicate and very expensive, limiting the number of channels to be measured simultaneously. Indeed, the ideal solution should be to place the detector directly in contact with the skin or the material under analysis in order to avoid the use of optical fibers [36]. The use of highly sensitive devices such as PMTs do not allow to place detectors directly on the scalp and is impractical in real-life operations since they are bulky, fragile and operate at very high voltages. Therefore the various types of photodetectors must be well studied and discriminated by a good classification including different properties, which are normally the average value of a statistical distribution [37]:

• *Quantum efficiency* (QE): it is the probability that a photon incident on the active surface of the detector generates a hole-electron pair. (0<QE<1).

• *Collection efficiency* (CE): it is the probability that a generated photoelectron start the electron amplification mechanism (0<CE<1).

- *Gain* (G): it is the mean value of the charge produced by the internal electron amplification mechanism per photoelectron generated.

- *Responsivity*: is defined as the ratio of output signal (e.g. the photocurrent) and the strength of the optical power impinging the detector.

- *Dark Current or dark noise*: it is the electrical current produced by the internal noise mechanisms of the photodetector in dark condition (i.e. when no photons strike the sensitive area of the detector).

- *Sensitivity*: in some cases its meaning is actually the responsivity of the photodetector. In other cases it is often understood as the ability to detect weak signals. Such ability is usually limited by dark noise.

- *Photon detection efficiency* (PDE) is often used for the combined probability to produce a photoelectron and to detect it (PDE = QE·CE).

- *Dynamic range* and *Linearity*: it is the maximum signal produced by the detector without a significant distortion with respect to the input signal.

- *Response time*: this includes the transit time, that is the time elapsed between the photon arrival time and the electrical output response of the detector, and the transit time spread, which contributes to the pulse rise time and the duration.

- *Rate Capability*: it is the maximum rate for photon detection and it is inversely proportional to the time needed, after the arrival of a photon, to get ready to detect the next, the *recovery time*.

- *Stability*: essential for long term operation at elevated counting rate

State of the art wearable CW-fNIRS systems employ photodiodes (PDs) for light detection, however their responsivity and dynamic range are poor and these systems are generally limited to few sparse optodes with fixed source detector distances also called "source detector separations" (SDSs) [38-40]. Avalanche Photodiodes (APDs), are detectors with internal gain (G ≈ 100) produced by the application of a reverse voltage not reaching the breakdown voltage. They

constitute an alternative to both PD and PMTs. Anyway the gain and the sensitivity of APDs are far from reaching those of PMTs.

Recently, high sensitivity solid-state detectors, such as single-photon avalanche diode (SPADs), have been applied for fNIRS but this solution is not optimal since the detector area is very small and the "digital" behaviour of these devices is not suitable for CW-fNIRS. In fact, the SPADs output is a current pulse emitted after a photon impinging its surface has triggered an avalanche. The light intensity, i.e. the number of photons impingig the sensor during a recovery time, has not effect on the output of the device and this behaviour limits the usability of these devices. Therefore, SPADs are better indicated for Time Domain systems [41] employing time-correlated single photon counting that needs particularly complex hardware.

In the last years, silicon photomultipliers (SiPMs), initially developed as a photon-number resolving detector for high energy physics applications (e.g., positron emission tomography scanners, Cherenkov telescopes) [42], have been proposed for biomedical applications [43] including fNIRS [44–46]. This kind of photodetector has been chosen for the development of a prototype system presented in this work.

Silicon photomultiplier devices are bidimensional arrays of SPADs, therefore the next session is dedicated to this particular kind of photodetectors.

## *3.1 Single Photon Avalanche Diodes (SPADs)*

The need to reveal very weak light and single photons with an output signal sufficiently high to be processed, the need to have robust, low cost and very sensitive photodetectors with low voltages conditioning, drove to the development of the technology for the fabrication of devices with a CMOS compatible process favoring their dissemination.

SPADs are p–n junctions operating in Geiger mode biased at a voltage above the breakdown voltage [47]. At this bias, the electric field is sufficiently high that a single charge carrier injected in the depletion region can trigger an avalanche. The current quickly rises with a risetime of the order of nanosecond or subnanosecond to a macroscopic steady level in the milliampere range, which can be easily discriminated by electronic circuits. If the primary carrier is photogenerated, the leading edge of the avalanche pulse marks the arrival time of the detected photon and then the current keeps flowing until the avalanche is quenched by lowering the bias voltage down below the breackdown voltage. Tipically the avalanche is self-quenched by the voltage drop due to the avalanche current flowing across a resistor

mounted in series to the diode (passive quenching). The avalanche can also be quenched by means of active circuits (active quenching). The nominal bias voltage is then restored in order to detect another photon. The time between the detection and the restoring of the bias voltage is the above mentioned recovery time, depending on the quenching approach, tipically of the order of nanoseconds. In this way, in SPADs the weak light detected is internally amplified with an high intrinsic gain, of the order of $10^6$: the avalanche multiplication by impact ionization is the mechanism that allows the photogenerated carriers amplification. In fact, When a photon impinging on the open window of the device is absorbed, it creates an electron-hole pair. The high electric field accelerates the photogenerated carriers, raising them to a kinetic energy large enough to ionize the crystal lattice with the subsequent production of electron-hole pairs. The new pairs are accelerated and multiplied as well, originating a process named avalanche multiplication.

### *3.1.1 SPADs Dark Count*

In SPAD devices, the thermal generation of charge carriers produce current pulses even in the absence of illumination, and the Poissonian fluctuation of these dark counts represents an internal noise source. The dark-count rate includes primary and secondary pulses [48]. Primary dark pulses are due to above mentioned carriers thermally generated in the SPAD junction, so that the count rate increases with the temperature. The rate also increases with the overvoltage, because of two effects: 1) the enhancement of the emission rate from generation centers due to the high electric field [49] and 2) increase of the avalanche triggering probability [50]. Secondary dark pulses are due to *after-pulsing* effects that may strongly enhance the total dark count rate. During the avalanche, some carriers are captured by defects in the lattice, related to deep levels in the junction depletion layer, and subsequently released with a statistically fluctuating delay [51]. Released carriers can trigger a new avalanche, generating afterpulses correlated with a previous avalanche. The number of carriers captured during an avalanche pulse depends on the lattice defectiveness and increases with the total number of carriers crossing the junction, that is, with the total charge of the avalanche pulse. Therefore afterpulsing increases with the current intensity, which is proportional to the overvoltage.

### *3.1.2 SPADs Photon Detection Efficiency (PDE)*

The measurement principle usually adopted for evaluating the quantum detection efficiency (QE) of photodetectors is a direct comparison with a calibrated photodiode that receives the same photon flux. The PDE of a SPAD is remarcable, as reported in figure 3.1.

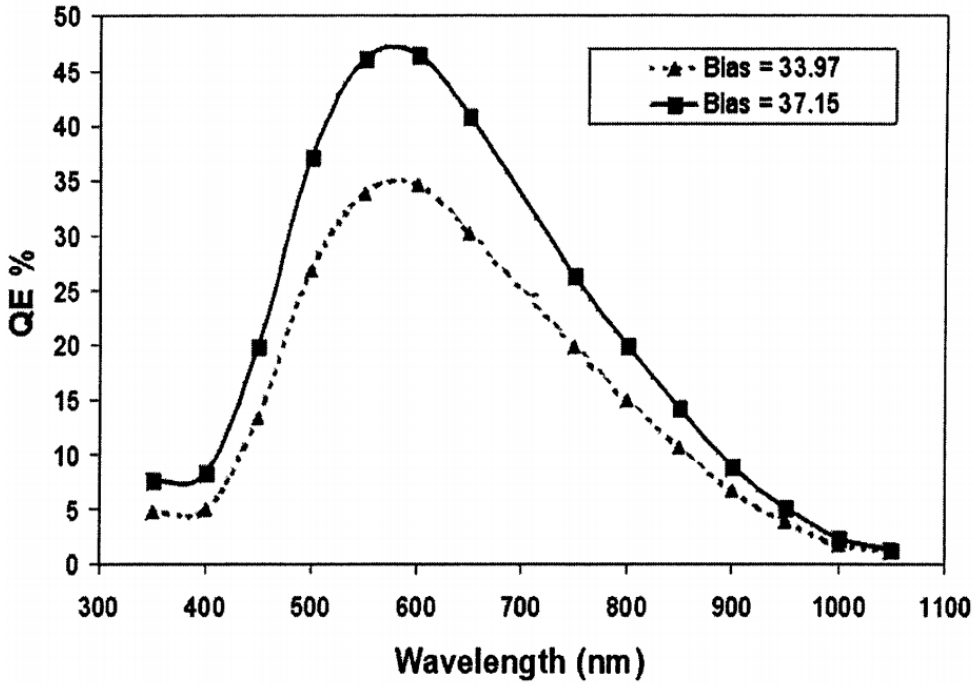


**Figure 3.1:** Measured quantum detection efficiency versus wavelength of a SPAD with 50 μm diameter, operated at 5 and 8 V overvoltage [47].

As mentioned before, a SPAD sensor operating in Geiger-mode functions as a photon-triggered switch, in either an "on" or "off" state. The high sensing capability of this kind of photodetector can be better exploited in a bidimentional array structure of SPADs connected in parallel. Such composite structure gives a much larger total sensing area and overcomes the lack of proportionality of the SPADs output with respect to the magnitude of a photon flux impinging the sensing area. This kind of photodetectors are defined Silicon Photomultipliers. The intrinsic characteristics of these devices, expecially the output proportional information on the input optical power, make the Silicon Photomultipliers very promising in application such CW-fNIRS.

## *3.2 Silicon Photomultipliers (SiPMs)*

As mentioned above, the Silicon Photomultiplier (SiPM) is constituted by a dense array of small, independent SPAD sensors, each with its own quenching resistor. Each independently operating SPAD and quench resistor is referred to as a "microcell". It is important to note that the Geiger avalanche will be confined to the single microcell it was initiated in. During the avalanche process, all other microcells will remain fully charged and ready to detect photons.

A typical SiPM has microcell densities of between hundreds and several thousands per $mm^2$, depending upon the size of the microcell. An example of simplified electric circuit to illustrate the concept is shown in Figure 3.2 [52]

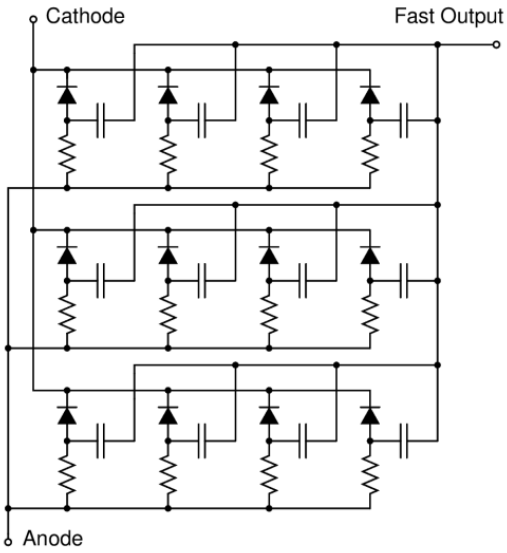


**Figure 3.2:** Scheme of a SensL SiPM used in this work (chapter 5) for time-of-flight measurements. The device has a summed output proportional to the number of photons impinging. The Fast output signal is the derivative of the internal fast switching of the microcell in response to the detection of a single photon [52].

The SiPMs used in this characterization are fabricated by STMicroelectronics, and each one consists of 50 × 50 pixels. The pixel active area is 40 × 40 $\mu m^2$, the filling factor (FF) is 62%, and the total device area is 6.45 $mm^2$ [22, 23]. The quenching resistor of 220 kΩ, needed for device Geiger mode operation, fabricated in doped polycrystalline silicon, is integrated directly in contact to the cathode. Figure 3.3 reports a schematic cross section of a SiPM single pixel in n-on-p configuration [53].

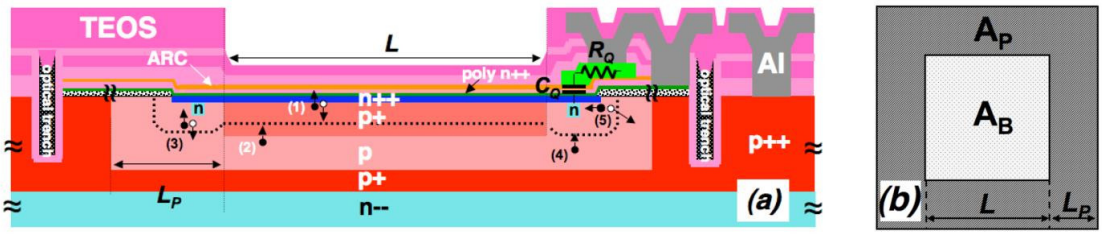


**Figure 3.3:** (a) Schematic cross section of a SiPM pixel. The dotted line is the boundary of the depleted region. L is the active area length, and $L_P$ is the perimeter length extension. (1) – (5) are the current components. (b) Front-side view of the SiPM pixel. $A_B$ and $A_P$ are the active and the perimeter areas of the pixel, respectively.

The optical trenches reported in the cross section of figure 3.3 constitute a technology solution to the cross-talk issue of pixelated photodetectors [54]. This additional component of SiPM noise is due to secondary photons that can travel to neighboring microcells and cause the triggering of avalanches.

The total responsivity of the SiPM biased at -30 V (OV = 2.2 V and G ≈ $6 \times 10^5$) is shown in figure 3.4, compared to those of a silicon APD (Hamamatsu S3884) operating at -141 V (G ≈ 100) and of a silicon photodiode (Hamamatsu S1337–1010BQ) operating at 0 V (red line). The SiPM shows the maximum responsivity in the red region (peaked at 670 nm with a value of $2.3 \times 10^5$ $AW^{-1}nm^{-1}$) and an excellent response in the NIR wavelength region of interest (700 – 900 nm), larger than $5 \times 10^4$ $AW^{-1}nm^{-1}$. SiPM responsivity is comparable with that of traditional vacuum tube PMTs (not reported) and not reachable by other silicon detectors, thanks to its high internal gain and good quantum efficiency . [55]

The SiPM responsivity measurements were compared with those of a commercial PD (Hamamatsu S1337–1010BQ – 100 $mm^2$) and of an APD (Hamamatsu S2385 – 19.6 $mm^2$). Responsivity measurements were carried out with a Bentham PVE330 in the 300 - 1100 nm spectral range. To prevent SiPM saturation neutral optical filters (OD = 5dB) were employed to limit the source light intensity.

The very promising characteristics and capabilities of Silicon Photomultiplier devices constitute the the encouragement for their use within the fNIRS and DOT.

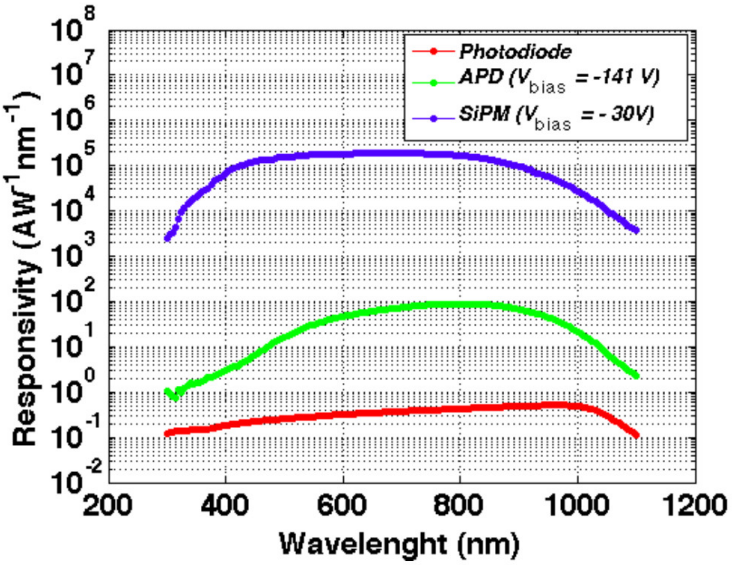


**Figure 3.4:** Comparisons of the responsivity vs. wavelength at -27°C of some silicon detectors (blue line STMicroelrctronics SiPM, green line Hamamtsu S3884 APD, red line Hamamatsu S1337–1010BQ Photodiode) [55].

## *3.3 Application of SiPM devices in an fNIRS prototype*

In this section is presented the development of a multi-channel, multi-distance, source time multiplexed, Continuous Wave (CW)-fNIRS prototype that relies on an optical probe constituted of 3 SiPM detectors and 4 LED sources (2 injection points, 2 sources for each light injection location at 735nm and 850nm wavelengths)[56]. Although the limited number of optodes, the prototype encompassed the required characteristics of a SiPMs based CW-fNIRS system. To validate the system, the sources and detectors were placed directly on the scalp of a volunteer, in a multidistance configuration. The overall optical probe covered 30 cm$^2$. The system was firstly characterized and then tested in vivo on a subject undergoing a motor task (Right Hand Finger Tapping). The probe was located over the contralateral primary sensorimotor cortex and the retrieved hemoglobin changes were compared with results obtained using a commercial system (ISS Imagent™, Champaign, Illinois) with an identical optical probe geometry.

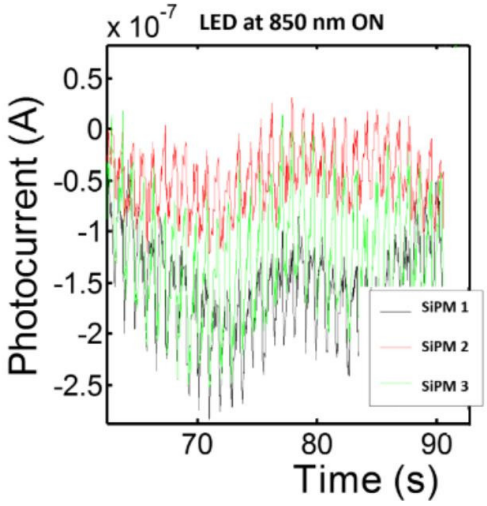


**Figure 3.5**: Example of signals from 1 LED at 850 nm recorded by the 3 SIPMs of the optical probe. The data were taken in vivo and at rest. They were estimated with an integration time of 10 ms. The average signal was subtracted to expose physiological signals such as heart rate and pressure waves (Mayer waves).

The commercial system employed laser diodes and multi-mode fibers for light injection and fiber bundles and high voltages PMTs for light detection.

Signal to noise ratio (SNR) in experimental conditions was evaluated directly in vivo (figure 3.5) and it was estimated to be ~65 dB with the considered optodes geometry.

Large area N-on-P SiPM detectors fabricated at STMicroelectronics clean room facilities were used for the measurements (Figure 3.6) [57].

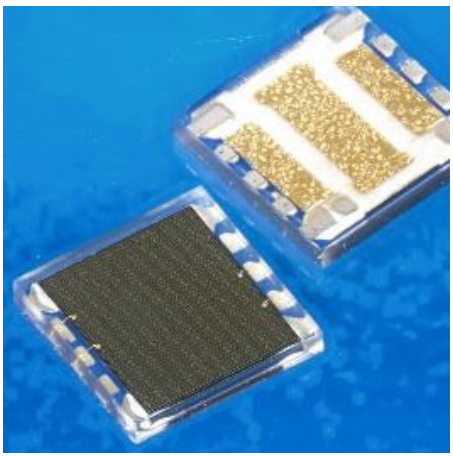

**Figure 3.6:** Example of two large area N-on-P SiPM detectors manufactured at ST (front and back view). The devices are packaged in a surface mount device (SMD) housing with 5.1x5.1 mm2 total area.

These devices were integrate thin optical trenches into their technology in order to decrease the cross-talk effects, especially for high overvoltage (OV) values applied to the detectors.

The SiPMs used for the measurements had a total area of 4.0 × 4.5 mm², 4871 square microcells and 60 μm pitch. The devices had a geometrical fill factor of 67.4% and were packaged in a 5.1 × 5.1 mm² area surface mount housing (SMD) sealed by a transparent epoxy resin. An Edmund Optics optical cast plastic CR-39® (Allyl Diglycol Carbonate) NIR long-pass filter with 700 nm cut-on wavelength and an optical transmission higher than 90% in NIR pass band range was glued on the SMD package [58]. The effect of filters glued on the SiPM surface is reported in figure 3.7 [59]. AlGaAs LEDs in SMD package emitting at 735 nm and 850 nm wavelengths were used to illuminate the interested area on the subject head. The LEDs had an area of 2.6 × 4.5 mm², a viewing angle of 55°, an average spectral bandwidth of about 30 nm and a power emission in the range from a few to at most 15 mW at both the emission wavelengths.

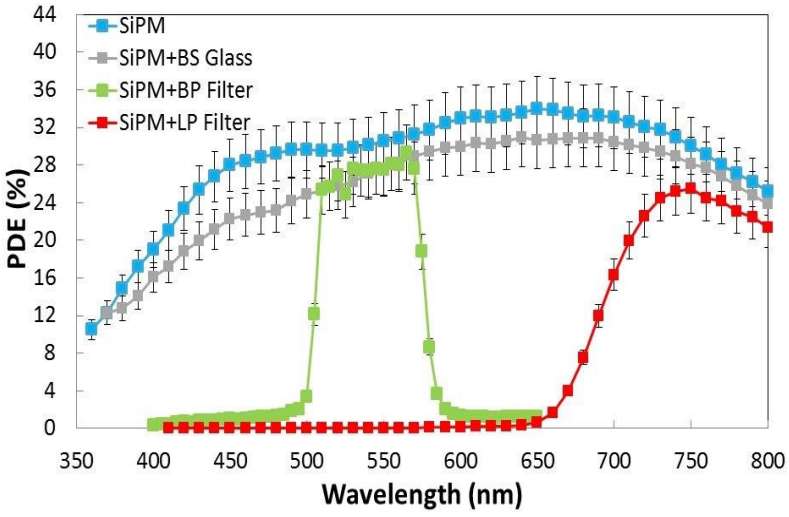


**Figure 3.7:** Effect of band-pass 500-600 nm and long-pass optical filters on total PDE of SiPMs

The SiPMs were mounted on a 1 cm² large PCB containing only the detector and passive electrical components (a 1 kΩ sensing resistor and a 100 nF filter capacitor). These small boards were connected to the acquisition electronics with flat cables about 2 meters long. Likewise, each dual wavelength LED was mounted on a small PCB, with the same connection layout (figure 3.8). Then, the two different boards were glued on a piece of black fabric with the optode layout shown in figure 3.10,

center. In order to have a probe with a smooth front surface, a sheet of black rubber was used, with appropriate holes in correspondence of light sources and optical detectors positions.

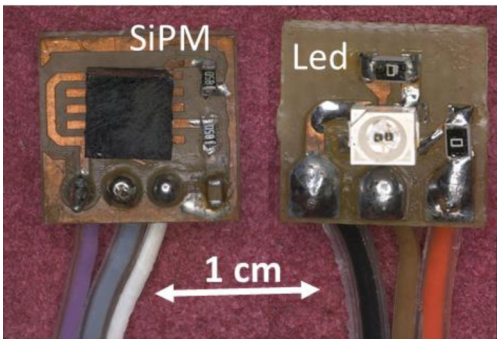


**Figure 3.8:** Sensor plus optical filters and double-wavelength LED small PCB boards implemented in the experiment

The thickness of the rubber, even compressed, was higher than those of LEDs and SiPMs, to ensure an effective optical isolation between sources and detectors. This simple probe layout resulted highly flexible and comfortable. LEDs were switched on and off at a frequency of 20 Hz.

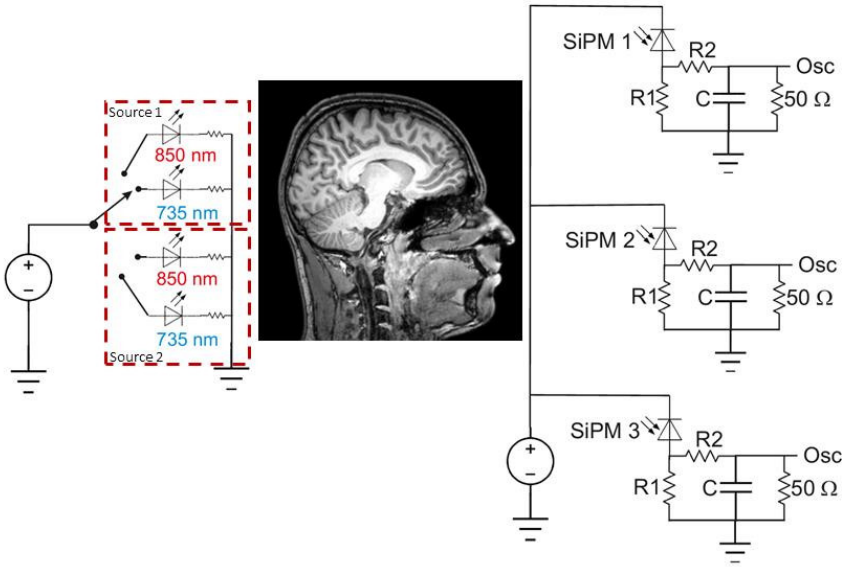


**Figure 3.9:** Experimental Setup

For each cycle, in which either only one colour LED was on and all the others were off, or the LEDs were all off for the dark current measurement, the same time interval was used. The time dedicated to each phase per cycle was 10 ms. The detectors were biased with the cathode at +30 V (3V-OV) while the anode was

connected to the parallel of a 15 kΩ resistor and of an RC integrator with a 0.15 ms time constant.

The voltage signals were recorded by a 1 GHz bandwidth digital oscilloscope, with a sampling frequency up to 20 kHz. The SiPM signals recorded in the oscilloscope were averaged in each phase of the cycle, i.e., in 10 ms time intervals.

The scheme of the experimental environment is shown in figure 3.9. The SiPMs-LEDs system was compared with the commercial fNIRS oxymeter through an in vivo experiment. Two in-vivo recording procedure were performed with the two systems. The subject (right-handed) C3 location (based on the 10-20 system) was identified and the optical patches located as reported in figure 3.10.

The subject set comfortably on a chair and performed a right-hand finger tapping task locked to an auditory stimulation ("start", "stop" commands). The task was performed for 4 consecutively runs. Each run was constituted of 40 seconds of rest and alternating 20 seconds for task and 20 seconds for rest trials.

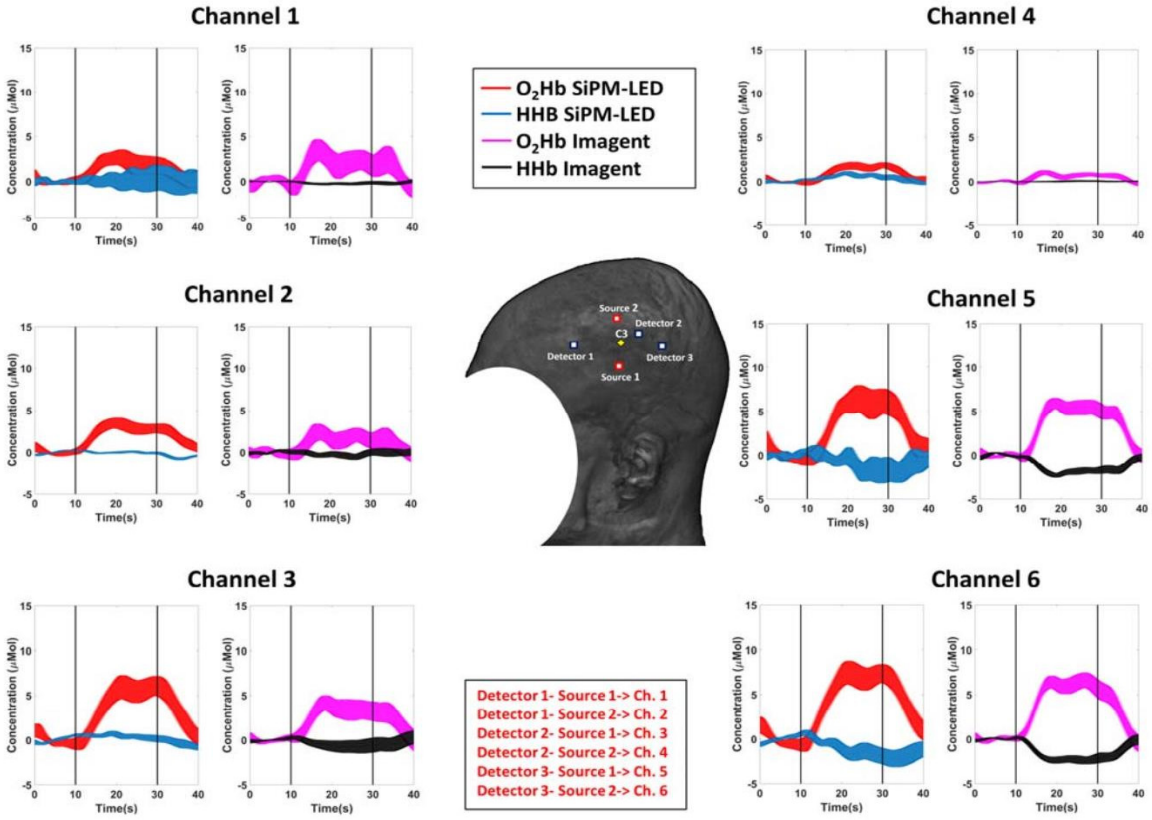


**Figure 3.10:** $O_2Hb$ and HHb responses to the motor task for the systems employed (6 channels each). The task period is identified by the two vertical lines. Optodes on the scalp and the subject's C3 (10-20 system) are reported on the rendered T1w Image of the subject [56].

The procedure was repeated for the two different systems. The overall experiment involved 32 finger tapping tasks (16 per system).

Average $O_2Hb$ and HHb responses to the motor task and related standard errors for the 6 channels employed and the two system are reported in figure 3.10 (based on the Modified Lamber Beer Equation [3], raw signals were filtered at 0.2 Hz using a zero-lag, 5th order Butterworth digital filter). The task period is identified in time by the two vertical black lines. Clear similarities are visible between the estimated hemoglobin responses of the two systems.

The results of this experiment showed the capabilities of SiPM sensors to be integrated for fNIRS imaging and their possibility to represent future state of the art detectors for wearable high numerosity and density optical neuroimaging. Further, scalp located light sources and semiconductor detectors may be of great help for expanding fNIRS as a neuroimaging tool.

In this validation experiment, N-on-P SiPMs were used because of their higher sensitivity for longer wavelenghts. In fact, since electrons have a higher probability than holes of initiating an avalanche, better efficiency can be achieved when the initial photon interacts in the p-type layer [52] and the photons have higher probability to reach such deeper layer if their wavelenght is in the infrared range in N-on-P configuration (figure 3.12), as it can be seen considering the aborption lenght of Silicon in figure 3.11.

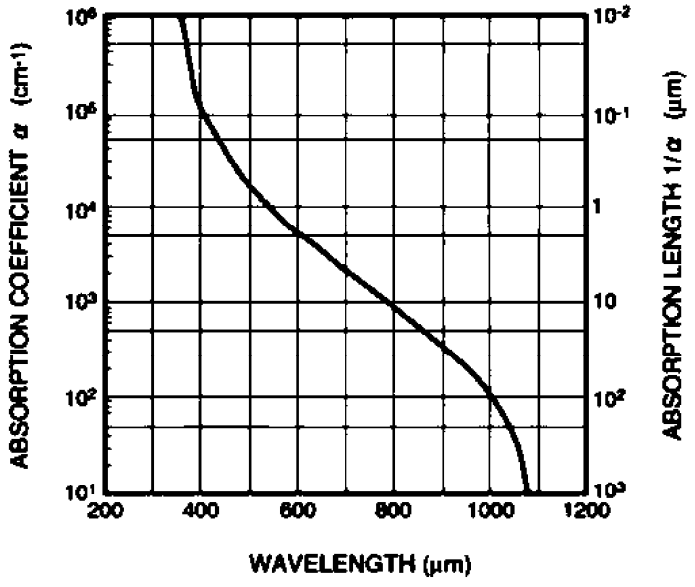


**Figure 3.11:** Absorption coefficient and absorption length in silicon semiconductors.

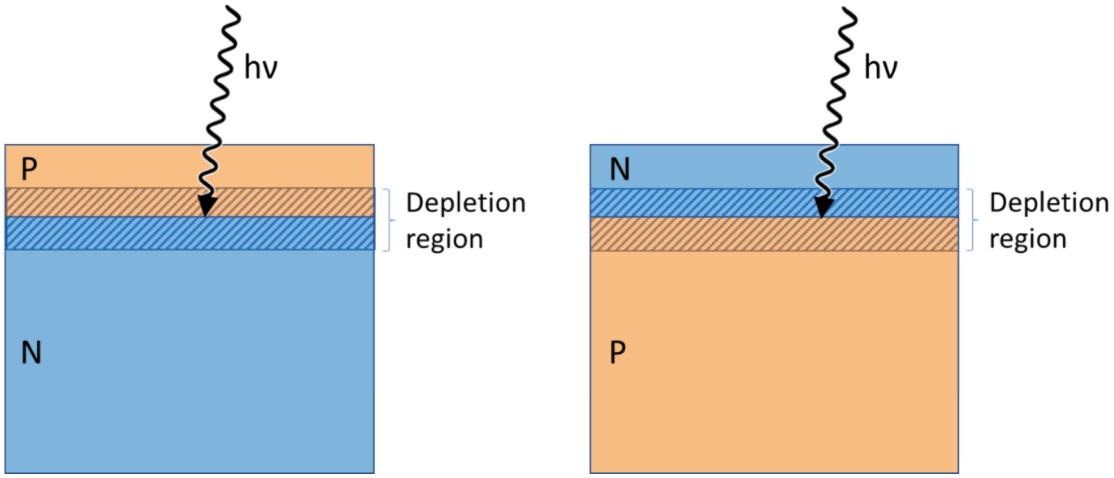


**Figure 3.12:** different diode structures: P-on-N gives best sensitivity to shorter wavelengths, and N-on-P for longer wavelengths.

However, the infrared photons that reach the p region in P-on-N devices, generate carriers that are likely to be trapped by Boron-oxygen related defects, causing afterpulsing effects and limiting the blinking frequency of LEDs in multichannel fNIRS/DOT systems. The sensitivity of P-on-N SiPM devices still remains remarkable in the NIR range, as it will shown in the following chapters, therefore they will be studied and employed in the experimental section of this work. In fact, despite the good results obtained integrating SiPM devices in an fNIRS prototype shown in this experiment, some artifacts were observed since the sensors performance came out without a significant characterization of the photodetectors behaviour in the NIR range, and without any system optimization in order to better exploit their very promising characteristics.

The next chapter addresses the above mentioned topics.

# Chapter 4

# Crucial aspects for the use of Silicon Photomultiplier devices in Continuous Wave functional Near-infrared Spectroscopy and Diffuse Optical Tomography.

The previous chapter described a successful integration of SiPMs in an fNIRS prototype and an in vivo comparison with a commercial system relying on laser diodes, PMTs, and optical fibers for light probing and detection. As seen before, the prototype system provided a correct estimation of brain hemodynamics [60]. However, some artifacts were observed and, to implement a real-time SiPM based fNIRS system, these need to be carefully analyzed and understood. For this purpose, this chapter is dedicated to the investigation of some major issues for the use of Silicon Photomultiplier (SiPM) devices in Continuous Wave functional Near Infrared Spectroscopy (CW fNIRS) and in Diffuse Optical Tomography (DOT). The attention has been focused on the analysis of the after-pulsing effect, on the physical mechanism causing it, and on determining its relevance for CW fNIRS/DOT. Here is presented a study about the SiPM transients occurring as the SiPM device goes from the dark (LED in off state) to the illumination (LED in on state) conditions, and vice-versa. Finally, the SiPM Signal to Noise Ratio (SNR) in standard CW fNIRS/DOT operation and the SiPM linearity range have been brought under observation.

## *4.1. Experimental*

In chapter 3 it is described how n-on-p silicon photomultiplier devices has been integrated in a multichannel fNIRS system. In this chapter, p-on-n SiPM detectors instead of n-on-p ones have been used for the argumentation about the main issues of these devices in an fNIRS/DOT context.

The large area p-on-n SiPM detectors used in this section are manufactured at STMicroelectronics clean room facilities [61].

The SiPM structure, formed from planar $p^+$–n microcells, was fabricated onto a low doped n-type silicon epitaxial layer grown onto a highly doped n-type CZ substrate. An implanted n-layer forms an enrichment region, which defines the active area and breakdown voltage of the junction. The anode is given by the diffusion of boron from a doped in situ thin polysilicon layer deposited on the top of the structure. The $p^+$ layer overlaps the enrichment region to form a virtual guard ring in order to reduce the electric field at the edge of the diode and ensure a uniform breakdown region in the central area of each microcell. The quenching resistor, made from low doped polysilicon, is integrated on the anode of the cell itself. Thin optical trenches, filled with oxide and metal, surround the pixel active area in order to reduce electro optical coupling effects (crosstalk) between adjacent microcells. The SiPMs used for the characterization have a total area of 4.18 × 4.68 $mm^2$ and 4871 square microcells with 60 μm pitch. The devices have a geometrical fill factor of 67.4% and are packaged in a surface mount housing (SMD) with 5.1 × 5.1 $mm^2$ total area. The SMD package is sealed by an epoxy resin transparent in the visible and near infrared wavelength ranges with a refractive index of about 1.5 at room temperature. The SiPM devices have a breakdown voltage of about 28 V at room temperature, and a photon detection efficiency (PDE) of about 12% and 8% measured at 529 nm and 700 nm and 4V-Overvoltage (OV).

Roithner LaserTechnik SMC700 and SMC830 AlGaAs LEDs in SMD ceramic package emitting respectively at 700 nm and 830 nm wavelengths, was used as optical light sources. The LEDs have an area of 2 × 2 $mm^2$, viewing angle of ± 55°, average spectral bandwidth of 20 nm and 35 nm at 700 nm and 830 nm emission wavelengths respectively. The average power emission ranges from 0 to at most 3 mW and 10 mW, for 700 nm and 830 nm, respectively, in the standard LED operation range. A further Osram LT M673 InGaN LED at 529 nm wavelength with a luminous intensity from 0 to 160 mcd has been used. Further features are the average spectral bandwidth of 33 nm and a viewing angle of ± 60° in standard LED operation range. LEDs were biased using a Tektronix AWG2005 programmable voltage function source with a time resolution of 20 MS/s, 12-Bit (1/4096) vertical resolution. LED rise and fall times are of some tens of ns, up to about 100 ns. Such times are close to the rise and fall time of the AWG2005 programmable voltage function source, and it has been verified that in all the cases the overall LED plus function generator switch on or off times are well below 200 ns. The time scales of

the phenomena investigated here are much longer, above 0.5 μs, so they are not influenced by the LED rise and fall times.

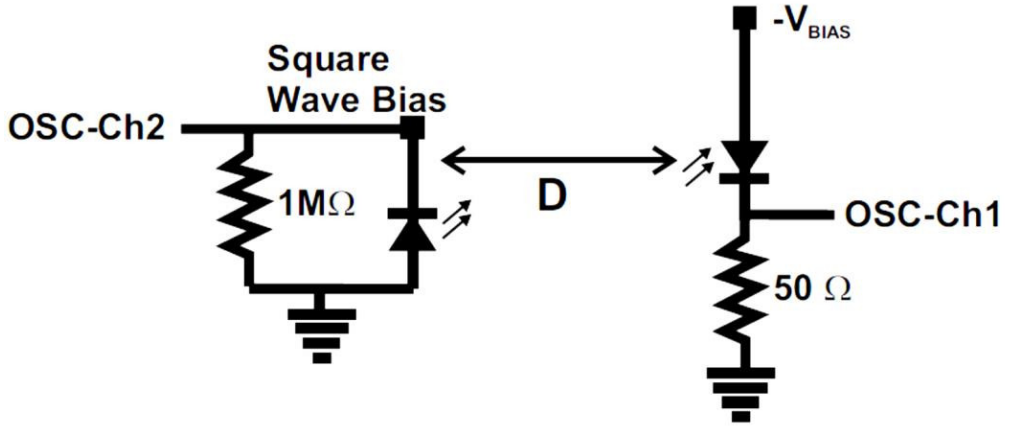


**Figure 4.1:** Scheme of the experimental set-up used to measure SiPM after-pulsing, SiPM temperature transients and signal-to-noise ratio. The distance D was about 10 cm for the first two measurements and about 80 cm for the SNR.

The SiPM current transients were measured in a Tektronix DPO7104, 1 GHz analog bandwidth digital Phosphor Oscilloscope with up to 20 GS/s real-time sample rate on one channel. The attention is focused on various aspects of SiPM operation in typical CW fNIRS/DOT conditions. Figure 4.1 reports the scheme of the experimental set-up used to measure the SiPM characteristics under observation. The distance D was about 10 cm for afterpulsing and thermal transient measurements and about 80 cm for measuring the SNR. SiPM devices were contacted in a Cascade Microtech probe station equipped with an ERS Electronic AC3 thermal chuck. The device temperature was controlled by the thermal chuck, and since the SiPM is in package, its temperature was evaluated through the measurement of the I-V characteristics. In the case of forward bias the SiPM temperature can be evaluated by considering that the SiPM current grows as $\exp(qV/nk_BT)$ where q is the elementary charge, V is the voltage, n is the ideality factor, $k_B$ is the Boltzmann constant, and T is the device temperature. In reverse bias in Geiger mode, the SiPM temperature was estimated by the temperature dependence of the dark current, as described in the following section.

## *4.2. After-pulsing effect*

The first source of artifacts when using SiPM in CW fNIRS is the SiPM after-pulsing phenomenon. It has been from long time recognized as a major problem for the application of SiPM and SPAD devices in measurement systems. Therefore, large efforts were spent to characterize this parameter, to understand the physical mechanisms underlying this phenomenon, and reduce or possibly suppress this spurious noise effect [63–64]. The afterpulsing is attributed to defects, which trap carriers produced by the avalanche, and release them with delay triggering correlated avalanches [65]. Figure 4.2 reports the SiPM transient after the LED switch off averaged on 500 traces with a 100 MHz sampling frequency. Both red (700 nm) and a green (529 nm) LED sources are compared. In both cases, when the LED is in the on state, the optical power incident on the SiPM under test was of about 60 nW. After 700 nm illumination, three peaks at about 1, 1.5, and 4.5 μs delay are clearly visible. Results similar to those obtained at 700 nm were collected at 830 nm, hence they will not be shown for brevity. After 529 nm illumination, only one peak at about 1 μs is detected. These peaks are detectable after the LED is switched OFF, with an intensity considerably lower with respect to the ON state photocurrent one. They are attributed to an after-pulsing / delayed detection effect.

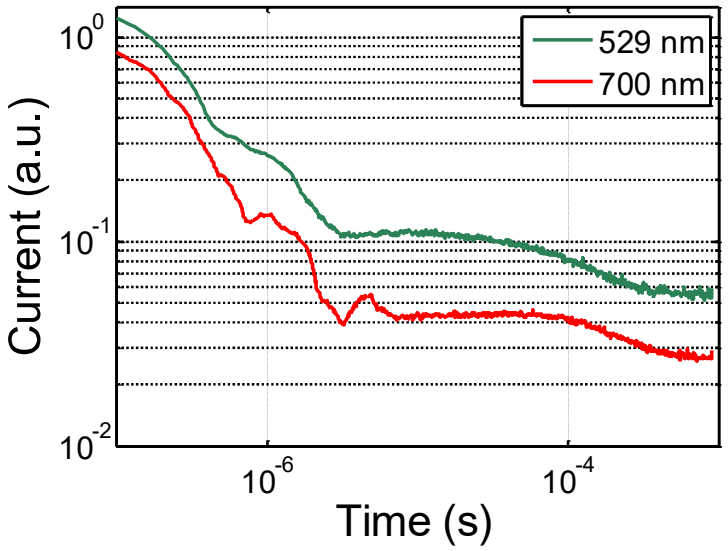


**Figure 4.2:** SiPM transient after 529 nm and 735 nm wavelength LED switch-off, averaged on 500 traces, 100 MHz sampling frequency

It is important to underline that the time scale of the peaks observed here (1-10 μs) completely rules-out a mechanism involving the diffusion of photons. In 1 μs a

photon in Si travels to a distance of about 85 m, much larger than both the SiPM device size and the light absorption length, being the last of the order of a few microns. Therefore, to explain their presence, it is needed to consider other mechanisms.

The inspection of figure 4.2 clearly indicate the presence of numerous peaks after 700 nm illumination, while only one peak is observed, at the shortest delay (about 1 μs), after the 529 nm LED illumination. Such circumstance suggests that the observed peaks are due to emission of minority carrier (holes) from defects located at large depths in the device. Such holes travel by diffusion to the surface reaching the multiplication region and triggering the avalanches, thus producing a time-delayed detection. Some arguments in favor of the above hypothesis are discussed in the following. The SiPM is a p-on-n device illuminated from the front side, i.e. from the p + anode side, hence, the light penetrates quite deeply in the detector. The absorption coefficient in silicon ($\alpha$) is ~3 × $10^3$ and ~8 × $10^2$ $cm^{-1}$ at 529 and 700 nm [66], corresponding to absorption lengths of ~3.3 and ~12.5 μm, respectively.

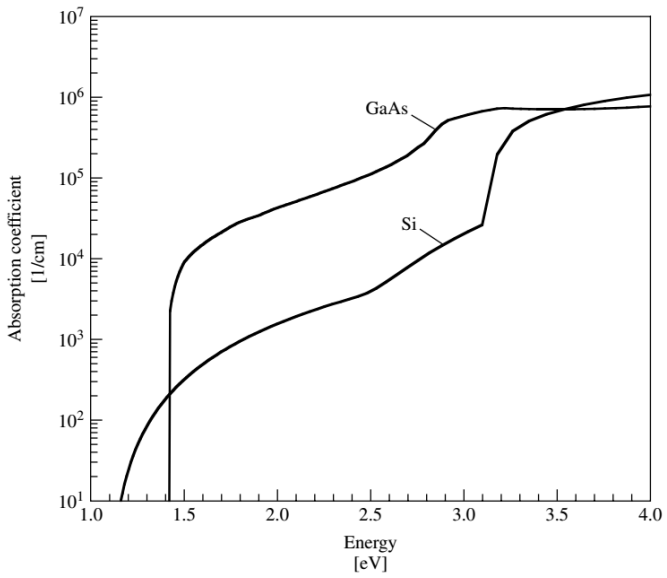


**Figure 4.3:** Absorption coefficient as a function of photon energy for Si (indirect band gap) and GaAs (direct band gap) at 300 K. Their band gaps are 1.12 and 1.4 eV, respectively. The wavelength of a photon is given by $\lambda = hc/E_{ph.}$

Since 95% of the light is absorbed within a $3/\alpha$ thickness, the "illuminated" region, i.e. the detector absorption region, is estimated as about 10 μm and 37.5 μm at 529 nm and 700 nm, respectively. Therefore, when the LED is ON, the SiPM device contains minority carriers (holes) in the n-region, which diffuse towards the multiplication region, where they have a high probability to trigger the avalanche.

For p-on-n SiPMs this is the "normal" detection mechanism, which requires holes diffusion. It is a quite slow mechanism, but for the CW fNIRS application, where the device speed is not a crucial feature, SiPMs can still be used. The results are, indeed, excellent, since the gain due to the avalanche allows a very large device responsivity. In addition to the "normal" mechanism, a parallel one is proposed in this work, involving defects located at large depths, tens of microns, responsible for a delayed detection/afterpulsing effect. The proposed mechanism provides that such defects can trap some minority carriers (holes) and release them with a delay. Like in the normal detection mechanism, holes will travel by diffusion to the multiplication region and trigger the avalanche. The explanation proposed is that the peaks shown in Figure 4.2 are, then, due to the time needed by the minority carriers to diffuse from the defect location to the avalanche region. The presence of peaks can be ascribed to the fact that defects are present only starting from certain depths. In fact, if the light has an absorption length able to reach such depths, the defects will then emit minority carriers, but it will be required some time for such carriers before they can actually reach the multiplication region near the surface. So for "deep" defects, i.e. located at large depths, and not close to the surface, a delay has to be observed. It should be reminded that the same conclusion drawn for 700 nm can be extended to 830 nm illumination.

At 700 nm the peaks are at t = 1, 1.5 and 4.5 μs, which correspond to depths, estimated as $\sqrt{(D \times t)/3}$), where D is the hole diffusivity, of 20, 25, and 43 μm, respectively. In fact, the holes are emitted at the depth at which the defect are located, and then such emitted carriers, to be detected, have to reach the multiplication region of the SiPM, located near the surface. The diffusion is isotropic, then $D \times t = \sigma^2 = \sigma_x^2 + \sigma_y^2 + \sigma_z^2 = 3\sigma_z^2$, since $\sigma_x = \sigma_y = \sigma_z$, where $\sigma^2$, $\sigma_x^2$, $\sigma_y^2$, and $\sigma_z^2$ are the total variance and the variances in the x, y, and z directions.

The $\sigma_z$ values (equal to $\sqrt{(D \times t)/3}$), i.e., 20, 25, and 43 μm, are perfectly compatible with the "illuminated" depth, estimated as $3/\alpha$, equal to 37.5 μm at 700 nm. On the other hand, at 529 nm wavelength, the "illuminated" depth is shallower, i.e. 10 μm, and it is consistent with the presence of only a single peak at the shortest delay, about 1 μs, with a $\sqrt{(D \times t)/3}$) of 20 μm.

Such depths correspond to the n + CZ substrate, where the presence of defects is likely since there are high P and O concentrations and, consequently, a large probability of generating impurity complexes and precipitates [67–69]

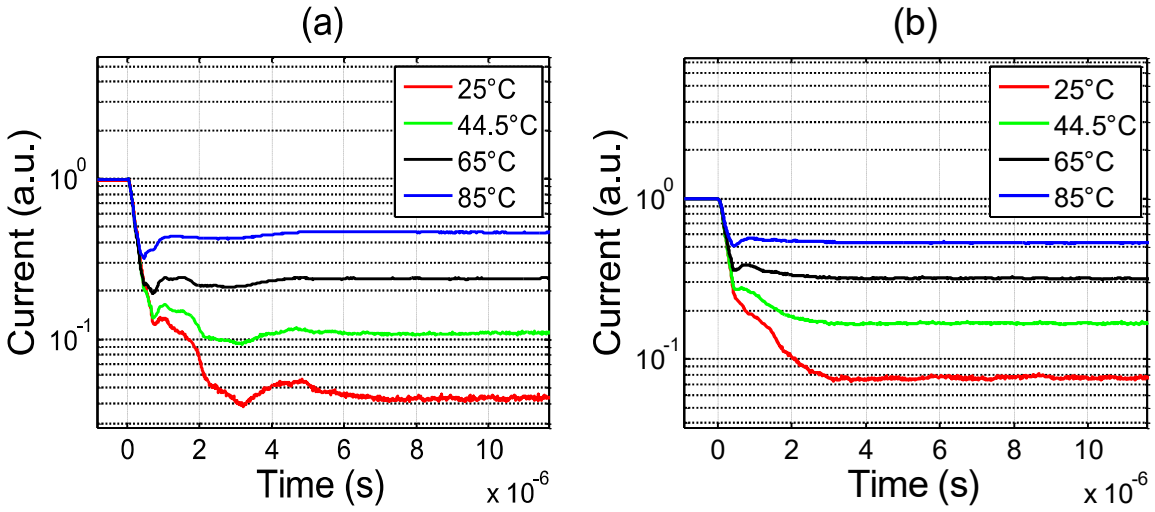


**Figure 4.4:** SiPM transient after 700 nm (a) and 529 nm (b) LED switch off, averaged on 1000 traces measured at 5 GHz sampling frequency.

By changing temperature, all the peaks at 700 and at 529 nm are still well visible, as shown by the data reported in Figure 4.4. This is well explained by the proposed mechanism, since the holes diffusivity has a relatively weak temperature dependence in the investigated range. In ref. [70] time constants of the same order of magnitude are observed, though no peaks are found. This suggests that in the SPADs studied in ref. [70], similar defects are present but they are uniformly distributed in depth.

## *4.3. Thermal transients*

In figure 4.2, after the regions of the peaks, a current transient is still present, whose duration is of the order of a few hundreds of microseconds. These transients are quite visible in figure 4.4 (a) and (b), where a linear time scale is used.

Clearly, the presence of current transient during SiPM operation has an impact in CW-fNIRS/DOT applications and requires a detailed understanding. The first possible explanation is the emission of the trapped holes, which follows an exponential behavior with a characteristic time $\tau$. According to the Shockley-Read-Hall (SRH) model, $1/\tau$ is equal to $\gamma T^2 \sigma \times \exp(-E_T/kT)$, with $\gamma$ an universal constant, T the absolute temperature, $\sigma$ the hole trap cross section, k the Boltzmann constant, and $E_T$ the trap energy, i.e. the distance in energy between the valence band edge and the trap energy. Therefore, by increasing the temperature, according to the SRH model, the emissivity $1/\tau$ should increase. To verify this point, the temperature

dependence of the SiPM photocurrent transients after the LED switch off has been focused. The results are summarized in figure 4.6. A negligible temperature dependence is observed, allowing us to conclude that $E_T$ should be essentially zero. In such hypothesis, $1/\tau$ should be equal to $\gamma T^2 \sigma$. Therefore, by considering a typical value of $\sigma = 1 \times 10^{-15}$ cm$^2$, $E_T = 0$ eV, the SRH model would predict that $\tau$ should be of the order of 10 ps, i.e. about 7 orders of magnitude faster than what it is observed. Then, an explanation based on the SRH model for the slow part of the transient is ruled-out. To summarize, the observed after-pulsing peaks observed at times in the range 1 – 5 μs are due to defects in the $n^+$ CZ substrate which emit holes, the estimated distance traveled by the holes before triggering the avalanche is 20 μm or more. The defects must be shallow in terms of $E_T$, since a negligible temperature dependence is observed for the emission transient. The slow transient, well visible in figures 4.5 (a) and 4.5 (b) is not related to the holes emission from the defects. The explanation proposed in this work involves a thermal effect: when the SiPM device switches off, the temperature decreases and the SiPM current decreases too. To estimate the SiPM temperature decrease, the temperature dependence of the SiPM leakage current has to be considered. From figure 4.5 (a) and (b), it can be observed that the current transients at the LED switch-off correspond to a decrease of a factor 2 – 3 for chuck temperatures in the range 25 – 50 °C.

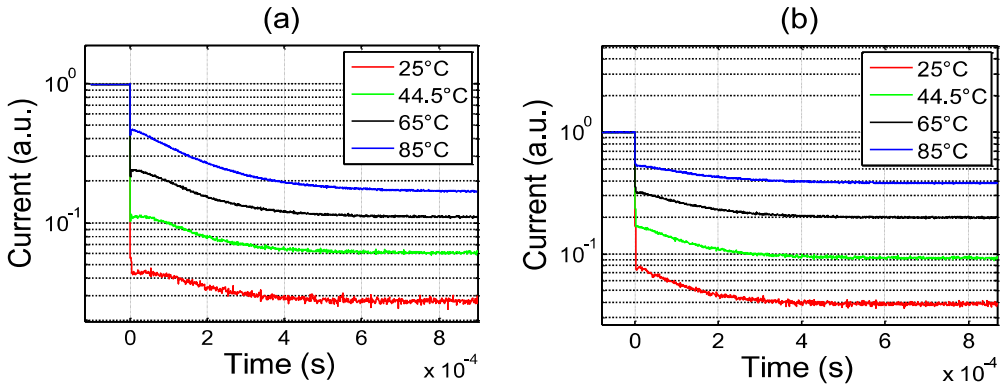


**Figure 4.5:** (a) averaged SiPM response after 700 nm LED switch off; (b) averaged SiPM response after 529 nm LED switch off. All signals averaged on 500 traces, 100 MHz sampling rate)

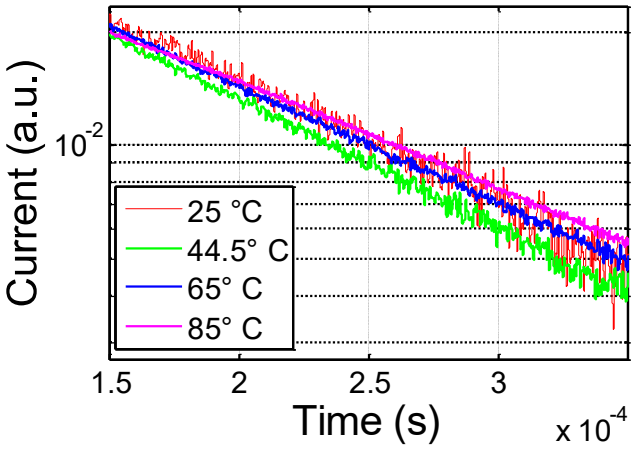


**Figure 4.6:** Normalized SiPM switch off transient (after 700 nm LED switch off) at various temperatures. The figure legends indicate the SiPM device temperatures measured in forward bias. See section 4.1. for further explanations.

Considering the temperature dependence of the steady-state SiPM dark current (figure 4.7), it can be observed that a change of the SiPM current of a factor 2 – 3 corresponds to a change of device temperature of about 10 – 20 °C.

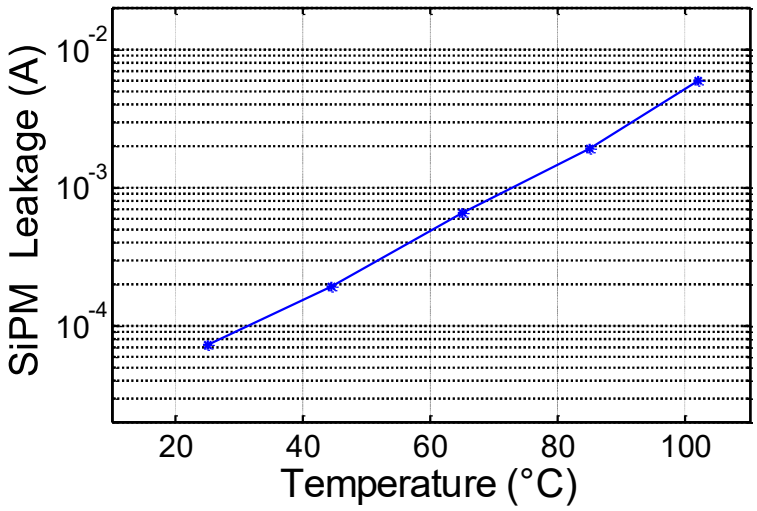


**Figure 4.7:** SiPM Dark Current temperature dependence (V bias = 32.5 V).

Therefore, the SiPM current transients at the LED switch-off may be explained in terms of a device cooling of 10 – 20 °C when the LED is switched off. In fact, when the LED is on, for the SiPM illumination conditions used in the experiments here reported, the power dissipated in the SiPM is of about 0.4 W, in the presence of an optical pump power of about 60 nW. By switching off the LED, the dissipated power

becomes suddenly small, a thermal transient takes place, and SiPM temperature decreases of 10 – 20 °C. Such explanation is well supported by considering the thermal resistance expected for a device of about 20 mm² in an SMD package, as we have. In such a case, the thermal resistance $R_T$ is expected to be in the range 10 – 100 °C/W [71], and therefore the expected device temperature change ΔT is 0.4W × $R_T$ = 4 – 40 °C, i.e. a temperature variation in good agreement with our conclusions.

According to the above explanation, the exact opposite thermal effect, i.e. a SiPM warming, should take place when the LED is switched on. In this case, the power dissipated in the SiPM goes from almost zero to some tenths of Watts, according to the optical signal level we used, in the range from 20 nW to 60 nW. This should increase the SiPM temperature in the same time scale, i.e., in some hundreds of microseconds.

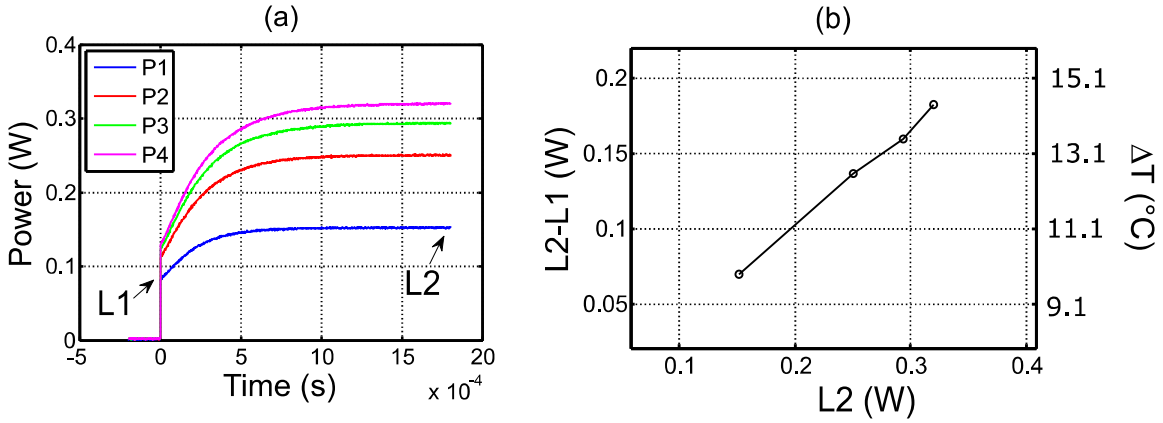


**Figure 4.8:** (a) SiPM dissipated power as the 700 nm LED is switched on at various levels of LED illumination. When the LED is switched on, the SiPM current and dissipated power rise to a level (L1), and then slowly increase to a steady state L2; (b) reports the temperature rise ΔT as function of steady state SiPM power dissipation (SiPM biased at 30.5 V). ΔT can be estimated from the difference L2-L1, since ΔT is expected to be an increasing function of L2-L1. Figure 4.6 (b) reports the difference L2-L1 as a function of the steady-state dissipated power L2. By considering the temperature dependence of the SiPM dark current reported in figure 4.5, and by assuming the same temperature dependence for the SiPM current under illumination, we can also evaluate the corresponding temperature change in °C, and this is reported on the right axis.

This is what can be observed: figure 4.8 (a) reports SiPM photocurrent transients as the LED is switched on, at various levels of LED illumination. When the LED switches on, at t = 0 in figure 4.8 (a), the SiPM current and power increase to a high

level (L1), but then there is a slow further increase to a steady state level (L2), in some hundreds of microseconds. The difference of dissipated power L2-L1 is an increasing function of the final temperature increase reached by the SiPM, while the steady-state power L2 is proportional to the illumination level. The plot of L2-L1 as a function of L2 is reported in figure 4.8 (b). A nice linearity is clearly observed. We can also estimate the temperature rise $\Delta T$, by considering the temperature dependence of the SiPM dark current reported in figure 4.7, and by assuming the same temperature dependence for the SiPM current under illumination. Through this hypothesis, we evaluate the corresponding SiPM temperature change in °C, and this is reported on the right axis of figure 4.8 (b).

## *4.4. Linearity range*

Thanks to the high gain of the SiPMs, it is possible to foresee different and high Source-Detector Separations, defining different depths of analysis and allowing the design of systems for Diffuse Optical Tomography. However, when the light source (LED) and the photomultiplier (SiPM) are placed on a volume under analysis, or on the scalp, the optical power reaching the SiPM can vary with relation to many factors: SDS, hair color, tissue properties, etc. These variations can cause non-linearity issues in a high-gain device. In fact, SiPMs have a relatively modest linearity region if compared to most of the other semiconductor photodetectors. A SiPM is an array of SPADs with resistors or active quenching circuits in series. Since the quenching time, though short, is finite, the maximum photon flux in the linear regime that can impinge the SiPM active area can be estimated as $N_{pixel}/(EQE \cdot T_{quench})$, where $T_{quench}$ is the average avalanche quenching time for each pixel, of the order of nanoseconds, $EQE$ the external quantum efficiency i.e. the ratio of the number of charge carriers to the number of incident photons, and $N_{pixel}$ is the number of SiPM pixels, ranging from hundreds to thousands, in commercial devices. Vice versa, the minimum limit of detectable photon flux is 3 dB above the level of the dark current related to the dark count, equal to $N_{pixel} / t_{dark}$ where $1/t_{dark}$ is the dark count rate of a single pixel of the device. [72]. The time scales of these phenomena (avalanche quenching and dark count) are relatively close, and therefore substantially limit the useful range of impinging optical power for the linear SiPM operation.

The operative linear range of the SiPMs used in this work is evaluated by measuring the photocurrent as a function of the optical intensity incident on the photodetector (figure 4.9). A SiPM was biased by using 28 V, 29 V, and 30 V

stabilized power supply, and its output current was measured by the voltage drop across a 1 kΩ resistor to reconstruct the typical operative conditions.

The lower limit of the data points in figure 4.9 for the incident optical power is approximately in correspondence with a SiPM photocurrent about equal to the dark current. Therefore, this is the lower limit of usable incident optical power. As far as the upper limit is concerned, taking as reference the case of 30 V SiPM bias, as shown in figure 4.9, a saturation of the SiPM photocurrent at about 1 mA is evident. Therefore, the corresponding optical power, of the order of $10^{-7}$ W/cm$^2$, represents the incident power upper limit.

It should be noted, however, that such onset for the sub-linearity regime is not due to the above mentioned SiPM avalanche pile-up effect, which takes place at a higher optical power for the used devices, but it is rather due to the use of the 1 kΩ resistor put in series in our system scheme. That is, the used resistor causes a reduction of the linear range compared to the native linear range of the detectors showed in figure 4.10 [52].

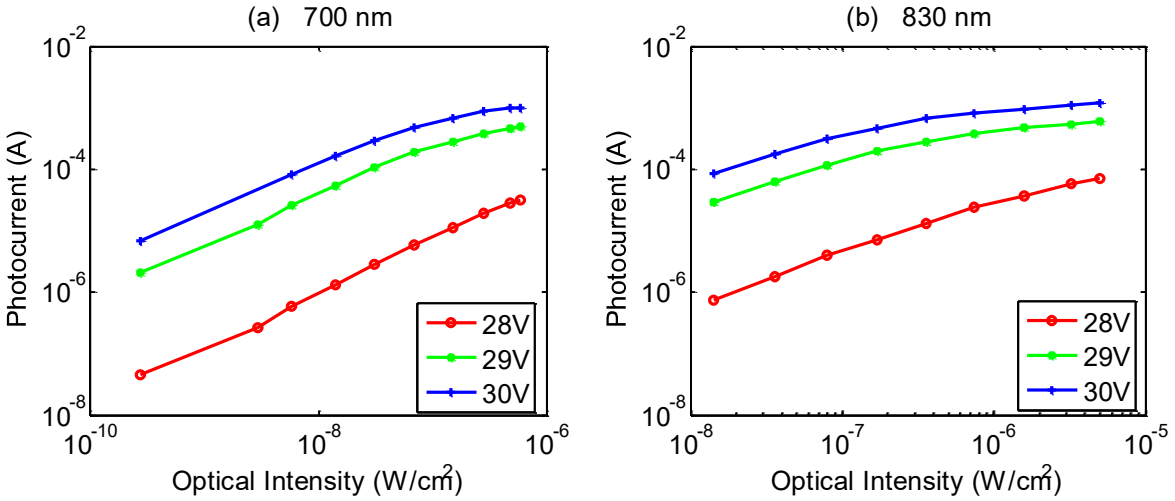


**Figure 4.9:** Operative range of used silicon photomultipliers with 1 kΩ resistor in series, measured under (a) 700 nm and (b) 830 nm irradiation.

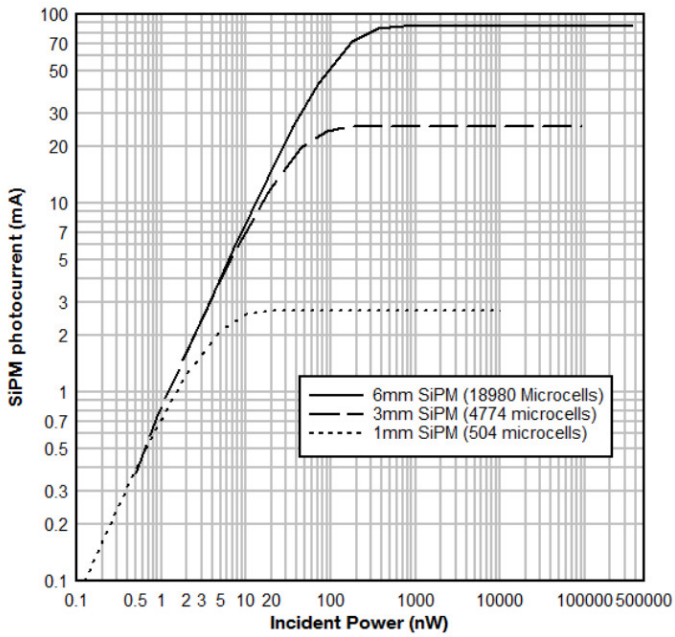


**Figure 4.10:** The SiPM Photocurrent as a Function of Incident Power on a Log-log Scale. The SiPM Maintains a Linear Response at Higher Levels of Incident Light when there are more Microcells [52]

In fact, if both the value of the resistance and the value of the photocurrent are high, the voltage drop on the resistor causes a shift of the SiPM working point during illumination, and consequently non-linearity is generated. For example, under about $5 \times 10^{-7}$ W/cm$^2$ illumination, the 1 mA output current of the SiPM on 1 kΩ resistor causes a reduction of the overvoltage of 1 V.

## *4.5. Signal-to-noise ratio*

The factors affecting the Signal-to-Noise ratio (SNR) of SiPM devices are essentially the crosstalk, the above-mentioned after-pulsing effect, and the dark count. Optical trenches between the pixels constitute the technology solution to the crosstalk related noise. The dark count has been thoroughly characterized in the recent past and it can be stated that the dark current rate of the single pixel at any temperature is due to the diffusion of minority carriers in the perimeter area of the pixel and to the SHR generation inside the depleted region of the active area of the pixel [53]. In this section, the SNR is evaluated for the whole system considering a single channel functioning in normal conditions at room temperature.

The system SNR is evaluated by performing measurements of the SiPM photocurrent signal under LED illumination [55, 73, 74] with a square wave of 17

Hz and 50% duty cycle. The experimental setup is a dark chamber with a LED and a SiPM placed opposite to each other at a distance of 80 cm. The signal (S) is the difference of the average photocurrent when the LED is on and the average dark current when the LED is off, while the noise (N) is the root-mean-square (RMS) of the photocurrent, thus, since the signal we measured is a voltage difference (current through a resistor), the SNR in dB is defined as $20 \log_{10}(S/N)$.

The data used to evaluate the SNR is an average of 10 on-off cycles of the LED, acquired by the oscilloscope with a constant sampling frequency of 1 MHz. To reduce the noise in a system channel, an integration can be performed with different time windows depending on the number of available samples. The blinking frequency of the LED, i.e. the overall refresh rate of a system channel, is the result of a fixed ADC sampling frequency and the number of samples in a temporal window to obtain the desired integration. In short, fixed a sampling frequency for the single ADC channel, the overall refresh rate is related to the maximum blinking frequency of the LED to obtain the desired number of samples useful for an integration in order to increase the SNR.

The data, obtained at 1 MHz sampling frequency, have been and integrated in a time range going from 100 μs (corresponding to an effective channel refresh rate of 10 kHz) to 10 ms (corresponding to an effective channel refresh rate of 100 Hz). The minimum optical power delivered to the SiPM by the LED sources was, both at 700 nm and 830 nm, of about 1 nW. Figures 4.11 (a) and (b) report the data of SiPM SNR as a function of the SiPM bias at two LED wavelengths, 700 and 830 nm, typical of fNIRS/DOT operation.

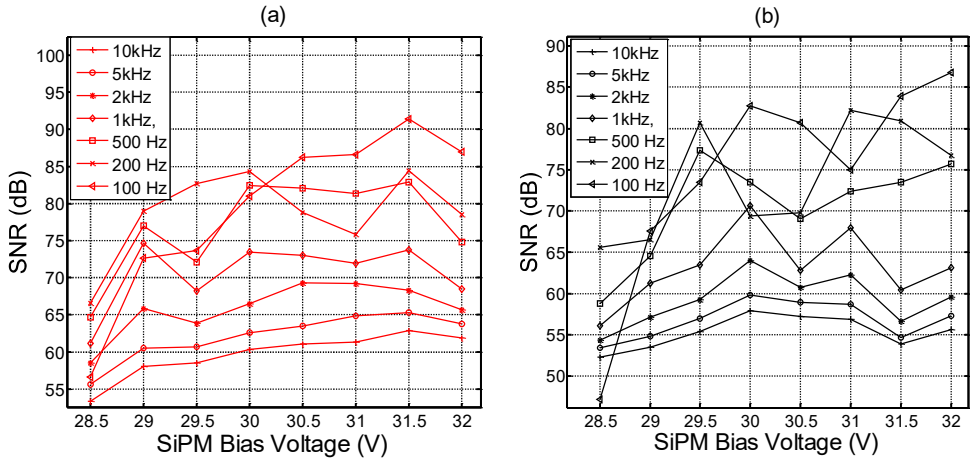


**Figure 4.11**: Signal to Noise Ratio as a function of bias voltages of the SiPM. Photocurrent measured under LED illumination with a square wave of 17 Hz and 50% duty cycle; (a) 700 nm LED; (b) 830 nm LED.

As the effective channel refresh rate decreases, or equivalently as the integration time increases from 100 μs to 10 ms, an evident improvement of the SNR is observed. The largest SNR is found at voltages of about 31.5 V, i.e. for ~3 V overvoltage.

Figure 4.12 reports the measured SNR at 31.5 V as a function of the effective single channel refresh rate. At 100 Hz, the SNR is above 80 dB, and the extrapolated SNR at 10 Hz is close to 100 dB, both at 700 and 830 nm.

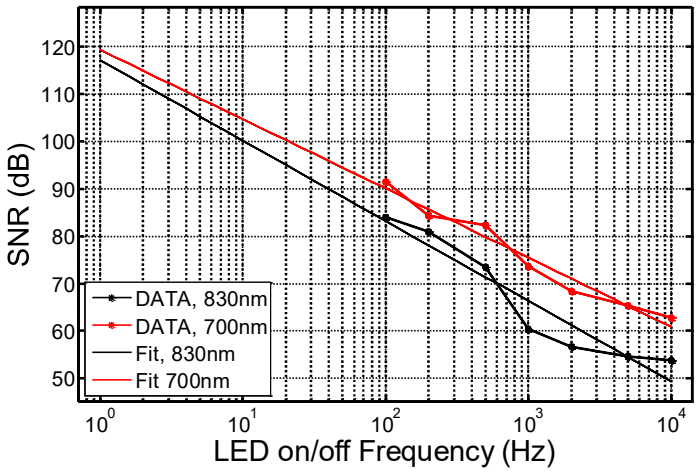


**Figure 4.12:** SNR at 31.5 V bias voltage measured (dots) and extrapolated (lines, linear fit) as function of the effective single channel refresh rate.

The SNR has been evaluated even in a multichannel system at different SDSs on a phantom made of a high scattering medium with $\mu_s' = 1$ cm$^{-1}$ and $\mu_a = 0.05$ cm$^{-1}$. In such a system, the ADC works in time division mode and the LEDs have to be triggered sequentially one at a time to avoid optical interferences.

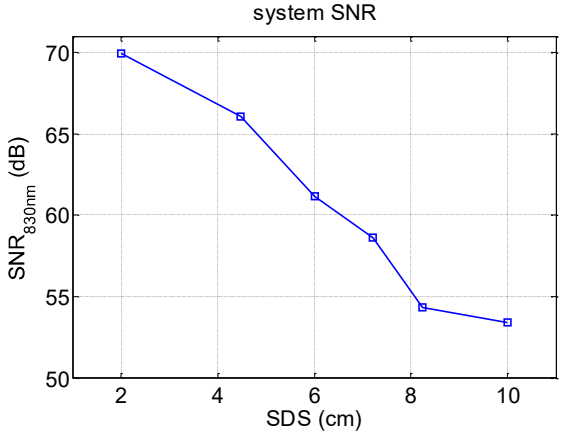


**Figure 4.13:** Single channel signal to noise ratio (SNR) vs. SDS measured on a phantom at 830 nm illumination

Nevertheless, using SiPMs biased at 30V, for a total effective acquisition time of 65 ms on 13 SiPMs, 24 LEDs, and 1 dark phase for all the photodetectors, the SNR values for a single channel, reported in figure 4.13, are quite remarkable. At 830 nm illumination wavelength, the SNR at 2 cm SDS results about in 70 dB and remains quite high, resulting in 53.4 dB at SDS equal to 10 cm.

## *4.6. In vivo results*

Taking into account all the considerations exposed in this chapter, a single-channel Continuous Wave fNIRS system relying on a SiPM, and two LED at 700 nm and 830 nm wavelengths respectively, has been tested in vivo on the author's head in C3 position of the international 10-20 system. The system refresh rate was of about 8 Hz to have a dark phase and the photocurrents related to each of the two wavelengths at every cycle. The dark current and the photocurrents have been obtained as the average of 500 samples each. The ADC sampling rate was set at 100 kHz. This sampling frequency would have allowed higher refresh rate, however, to avoid all the transients due to LED switch on and off and to the SiPM alfter-pulsing and thermal transients [75], waiting times of some milliseconds has been considered and a much larger time window is needed, and the overall refresh rate is reduced down to 8 Hz.

The dark current is subtracted to the two photocurrents at each cycle and the results are used to calculate in real time the molar variation of oxygenated and non-oxygenated hemoglobin by means of formulas explained in chapter 1.

Figure 4.14 shows the molar variation of the two molecular species obtained in real time by the prototype during an experiment.

The subject, with the LEDs and the SiPM placed on the scalp on position C3 of the 10-20 system with an SDS of 3 cm, was at rest for 80 seconds. After this time, the subject held his breath for about 20 seconds and then he resumed breathing. The variation in terms of blood oxygenation is clearly visible in figure 4.14 considering the major variations on the trends. It can be noticed that not only the major variations, but also the minor variations on oxygenation trend can be detected: heartbeat, and Mayer waves (a blood pressure related phenomenon with about 10 seconds period) are evident in the obtained signals.

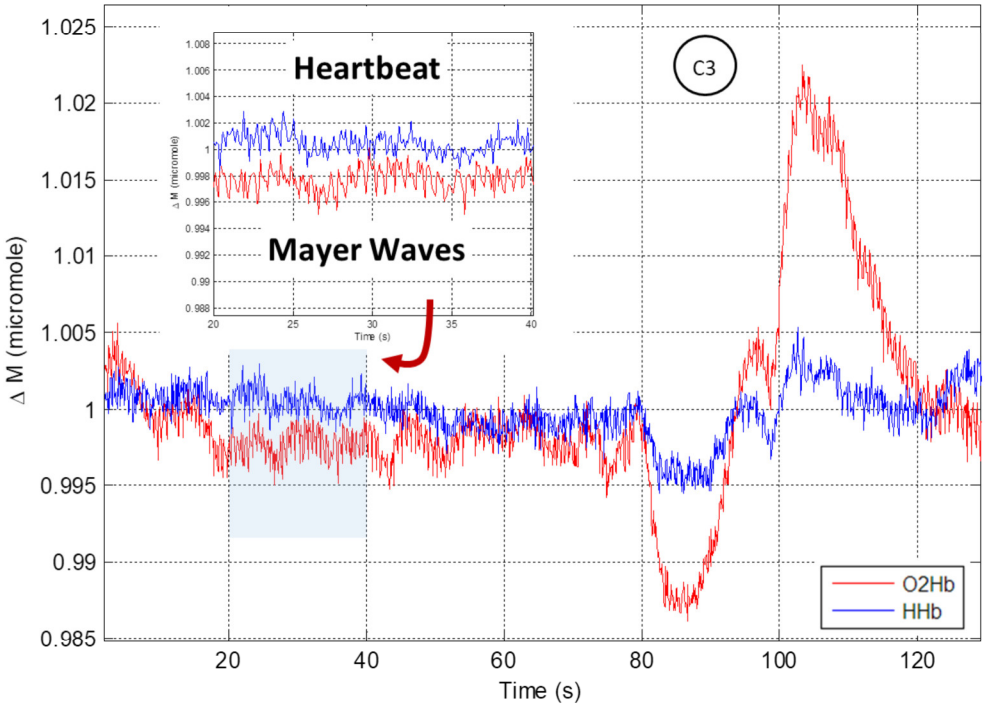


**Figure 4.13:** Single channel signal output of the fNIRS prototype. The software developed in LabVIEW® calculates in real time the molar variation of oxygenated (in red) and non-oxygenated hemoglobin (in blue) using the SiPM response to 700 nm and 830 nm illumination.

In conclusion, Silicon photomultiplier devices are very promising in the context of fNIRS and DOT. The intrinsic characteristics of SiPMs allow the development of very sensitive multichannel systems capable of analyzing different depths with overlapped measurements very useful in a Diffuse Optical Tomography context. On the other hand, they may present some issues such as the after-pulsing, the thermal transients and linearity with respect to the detected optical power. Therefore, it is necessary to optimize the systems in order to exploit all the advantages of this kind of photodetectors.

In the next chapter, a fiber-less prototype of an optical system will be presented. The prototype, built taking into account all the presented considerations, is equipped with 24 LED sources (12 at 700 nm and 12 at 830 nm, arranged in couples) and 13 SiPM detectors composing 156 channels.

# Chapter 5

# Imaging experiments: sensors, electronics, test materials, phantom, simulations, and results

## *5.1. The System Hardware: sensors and electronics*

The proposed CW system is equipped with 24 LED sources (12 at 700 nm and 12 at 830 nm, arranged in couples, with each 700 nm/830 nm LED couple mounted with an inter-LED distance of 2 mm) and 13 SiPM detectors, alternatively arranged in a checkerboard of 8 cm × 8 cm area and first nearest neighbor SiPM-double LED distance of 2 cm shown in figure 5.1. As explained before, the system is intended to detect oxy- and deoxy-hemoglobin concentrations, therefore the two wavelengths were chosen to straddle the isosbestic point of the two molecular species absorption spectrums located at ~800 nm [76]. The system is able to acquire 325 independent time averaged measurements [77], that is 13 measurements of 13 SiPMs dark currents, plus the signals under light, which are 13 SiPMs, multiplied by 24 LEDs (12 LEDs for each of the two wavelengths).

Large area p-on-n MICROFJ-60035 SiPM detectors manufactured by ON Semiconductors were used for the measurements here presented [78]. The SiPM structure is formed by planar p+ / n microcells with a total area of 6.07 × 6.07 $mm^2$, 22292 square microcells, geometrical fill factor of 75%, packaged in a surface mount housing (SMD), sealed by transparent glass with a refractive index of about 1.53 at 436 nm. The SiPM devices have a breakdown voltage of about 24.5 V at room temperature, and a photon detection efficiency (PDE) of about 10% measured at 700 nm and 6V-Overvoltage (voltage above the breakdown, OV). Roithner LaserTechnik SMC700 and SMC830 AlGaAs LEDs in SMD ceramic package emitting respectively at 700 nm and 830 nm wavelengths, were used as optical light sources. The LEDs have an area of 2 × 2 mm2, viewing angle of ± 55°, average spectral bandwidth of 20 nm and 35 nm at 700 nm and 830 nm emission wavelengths respectively. SiPMs were biased by using a 30 V stabilized power supply. In each cycle, the acquisition software subtracts each dark current from the relative SiPM photocurrent measured at the two wavelengths.

The overall measurement refresh rate of the complete system is about 2.1 Hz. The system is able to acquire 156 optical channels (LED pair source; SiPM detector couple).

In Figure 5.1 (a), the red circles represent the LED holders and the blue squares represent the SiPM holders. The 700 nm/830 nm LED pairs and each SiPM are mounted on a board and encapsulated in a holder of about 2 cm in diameter.

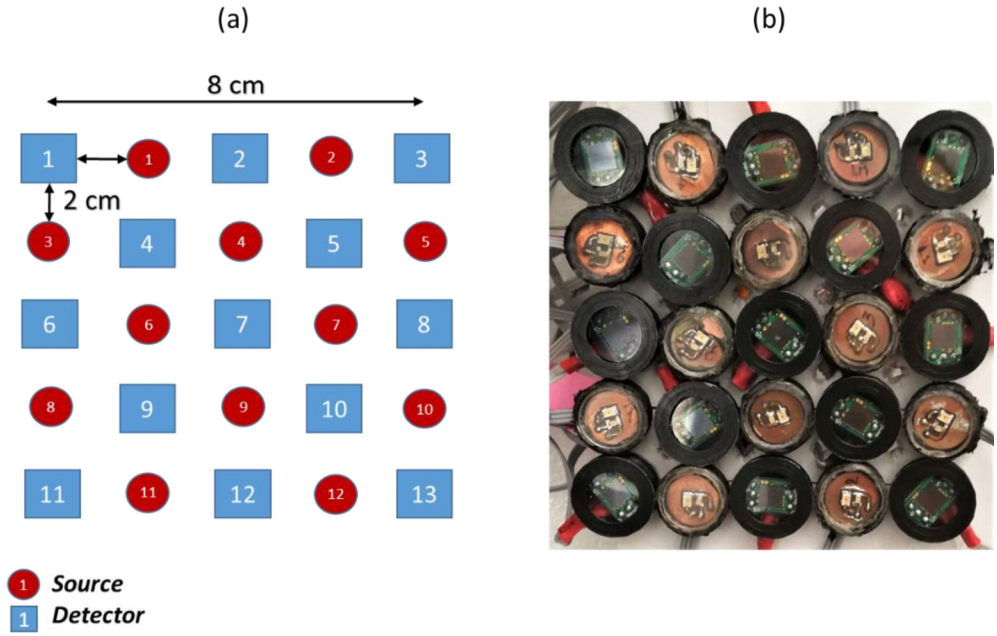


**Figure 5.1.** (**a**) Arrangement scheme of light source and detectors (top view). (**b**) Silicon photomultiplier (SiPM) and light emitting diode (LED) holders (bottom view).

The output currents of the photodetectors are measured by the voltage drop across readout resistor (1 kΩ) mounted on each SiPM board. A transparent filter (polycarbonate) is mounted on the top of the holders so that SiPMs and LEDs are optically well coupled and electrically insulated as seen in Figure 5.1 (b). The geometry of this arrangement is characterized by SDS distances of 2 cm, 4.47 cm, 6 cm, 7.21 cm, 8.24 cm, and 10 cm. Through the chosen placement of LEDs and SiPMs, it is possible to obtain various overlapping measurements at different SDSs in numerous points.

All the 13 SiPMs boards were connected to the analog inputs of a data acquisition system (National Instruments USB-6255 Multifunction device). The NI USB-6255 board is an USB high-speed Multifunction programmable Data Acquisition (DAQ) module with a 16 bit, 1.25 MS/s ADC, optimized for high accuracy at fast sampling rates. It also can drive 24 digital lines at a maximum of 24

mA for LEDs control as fast as 10 MHz. The LEDs are connected to the 24 Transistor-Transistor Logic Complementary MOS (TTL/CMOS) digital input/output lines of the NI-6255 through 0 – 5 kΩ resistive trimmers mounted on an auxiliary board. A further 0 – 900 kΩ trimmer is mounted to adjust the optical power of all the LEDs simultaneously. All the trimmers have been regulated to get the SiPMs output close to the upper limit of their linear range considering an SDS of 6 cm, to obtain high sensitivity at large source-detector separations. As shown in the previous chapter, the SiPM device has a *sub-linear* range due to the read-out resistor mounted on the board. In this portion of the range over the linearity, the photodetector is far from its saturation and is still capable to detect light power variations at the channels characterized by lower source-detector separation.

## *5.2. The System control software*

The system is governed by a software developed in the National Instruments LabVIEW® environment. A branch of this software is dedicated to the LEDs calibration and to the single channels output inspection. The main module of the software controls the system in order to manage the acquisition of data by setting the LEDs status, defining the channels, and acquiring the analog output of each single SiPM, avoiding optical interferences between different channels. During operation, time division measurements of all the SiPMs outputs are performed on the active input channels of the acquisition board at 1.25 MHz sampling frequency. The system starts performing a measurement of the dark current of all the SiPMs when all the LED are in off state. Then the 700 nm LED of the first LED couple is turned on and the system reads all the channels and calculates each point as the average of 250 measurements on the SiPM output. Then the 700 nm turns off and the 830 nm LED of the couple turns on, the system acquires all the SiPMs currents and repeats this operation for all the LEDs couples. After that, the cycle restarts from the beginning. This procedure prevents illumination interferences and ensures the correct definition of the channels. As far as the time resolution is concerned, the photocurrent signals are acquired on a 13 channels, 1.25 MHz frequency ADC, that is, each photocurrent is monitored for $1/1.25 \times 10^6$ s ( = 0.8 μs) on every $13/1.25 \times 10^6$ s (= 10.4 μs). The system performs 250 acquisitions, corresponding to a total measure time on all SiPM channels with only one LED on of 2.6 ms. Such operation is repeated for all LEDs, plus one dark phase. Hence, one complete measurement cycle may be performed in principle in 25 × 2.6 ms = 65 ms. However, we need to avoid all the transients due to LED switch on and off and to SiPM thermal transients [75].

For such reason we used a much larger time window, with a minimum cycle time of 476 ms and an overall frequency of about 2.1 Hz.

## *5.3. The Data Correction algorithm*

Though, as shown in the previous chapter, the SNR values are quite promising, and despite the above described regulation of LEDs to guarantee the output current of the SiPMs being at the upper limit of their linear range, the photocurrent signals still show instability and inhomogeneity effects. In Figure 5.2 (a) the photocurrents recorded on a static and homogeneous phantom (13 time traces for 830 nm light and 13 time traces for 700 nm light) related to the fourth nearest-neighbor source-detector distance (SDS = 7.21 cm) are reported. Figure 5.2 (b) reports in detail one of the photocurrent time traces related to 830 nm light.

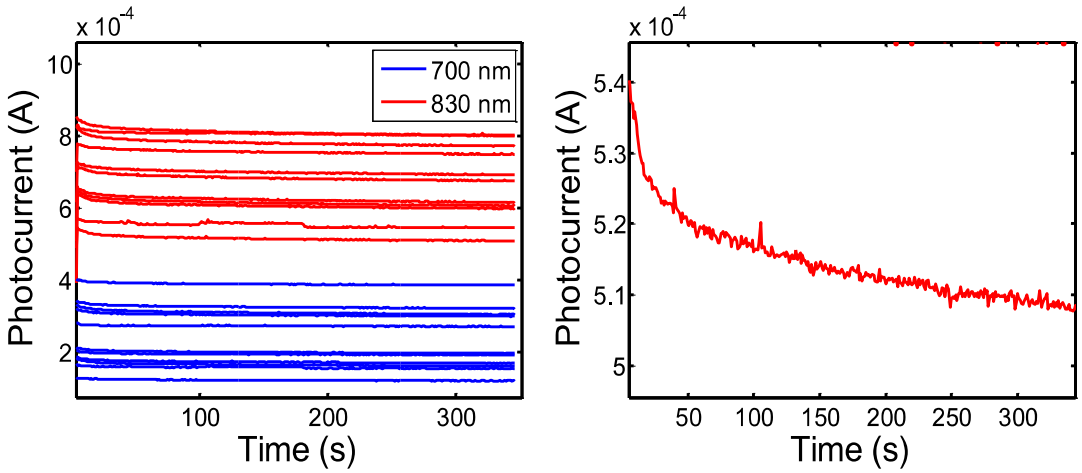


**Figure 5.2**: (a) Photocurrents (13 time traces for 830 nm light in red and 13 time traces for 700 nm light in blue) related to the fourth nearest-neighbor source-detector distance (SDS = 7.21 cm). (b) Detail: one of the photocurrent time traces related to 830 nm light.

It is possible to observe two types of phenomena affecting the measurement:

1. Differences on the value of the photocurrents related to channels with the same SDS, as shown in Figure 5.2 (a). They are due to little displacements of the LEDs or of the SiPMs, small differences in the EQE of the different SiPMs involved, or to differences among the LEDs' brightness.

2. Drifts over time of the photocurrents, as shown in Figure 5.2 (b). To explain the decrease over time of the photocurrents recorded on the static phantom, it is important to consider that we subtract the dark current to determine the SiPM signal. In general, at a constant bias voltage, as SiPM temperature increases, both the photocurrent and the dark current in a SiPM increase while the gain slightly decreases. Moreover, the light output of an LED at a constant current also decreases with the increase of its junction temperature [79]. All these instability effects sum up giving rise to the overall slow drift effects shown in Figure 5.2.

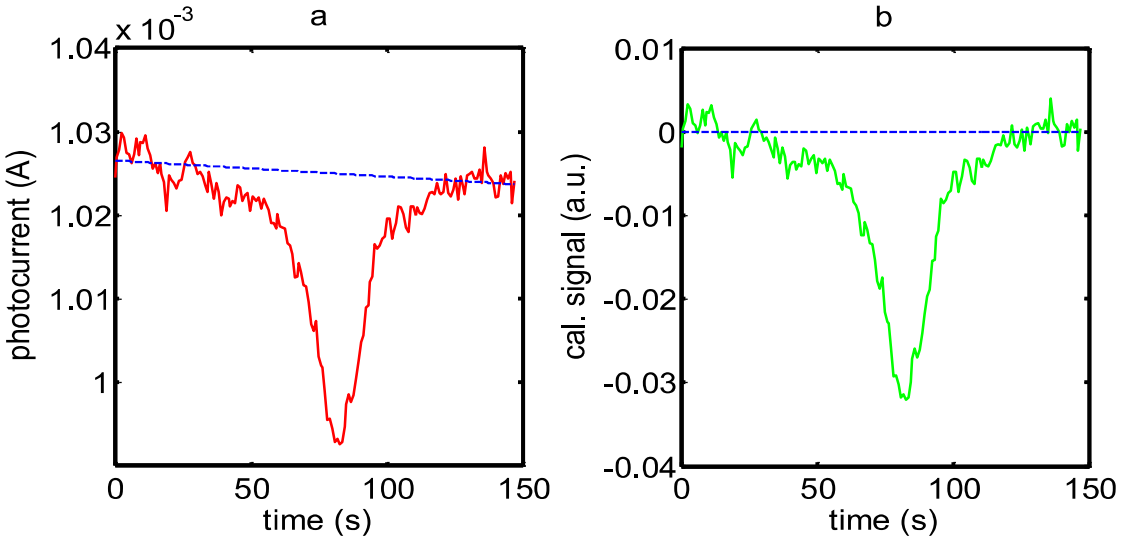


**Figure 5.3:** (a) uncalibrated photocurrent signal from one of the channels recorded during an experiment; (b) same signal after the calibration procedure.

To correct such issues we performed a calibration procedure off-line directly on recorded data. Figure 5.3 (a) shows an uncalibrated signal from one of the channels recorded during an experiment. If the status of the phantom is the same at the beginning and end of an experiment, the photocurrent is expected to have equal value in these two moments. Therefore, the calibration software implemented calculates the slope of the straight line connecting the average of the signal at the beginning and the average of the signal at the end of the experiment. Then, each sample of the signal is corrected with a compensation of this slope. The result of this procedure is shown in figure 5.3 (b). At the end of this procedure, all the signals have the same average value at the beginning and at the end of the experiments.

## *5.4 The dynamic Phantom*

A multilayered phantom made of a medium providing high light scattering has been built to test the proposed system. The medium is expanded polyethylene (EPE). Starting from the base at the bottom (Figure 5.4), the phantom is constituted by a 50 cm × 40 cm × 3 cm EPE layer, and a 3 cm thick layer of air in which a Newport step motor moves a stainless steel rectangular bar. In all cases the bars have a 1 mm thickness and a 20 cm length, and we have used three with different bar widths: 0.2 cm, 0.5 cm, and 1 cm. On the top, we placed a second 3 cm thick EPE layer on which the black patch with sensors and LEDs is positioned. The stepper motor rotates 1 degree in about 2 s (0.5 deg/s). Thanks to the motion driven by the stepper motor, the phantom is dynamic and constitutes a tool to test our system with good reproducibility.

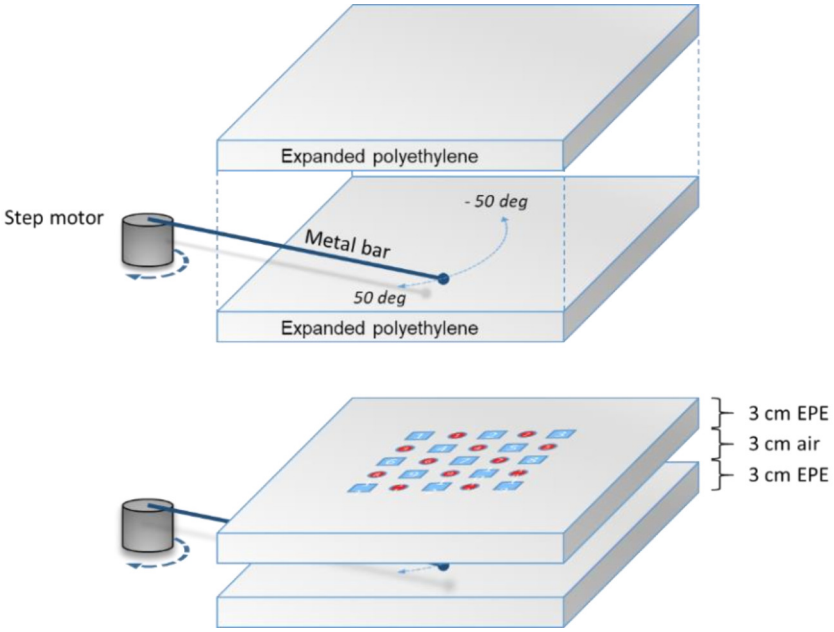


**Figure 5.4.** Scheme of the three-layer phantom with a mobile metal bar.

The phantom has two scattering media (the two EPE layers) and one non-scattering medium (the air gap). The optical characteristics of EPE are relatively close to those of human brain tissues and this was the reason to choose such material. In fact this in an uncommon choice: generally in the fNIRS literature other type of materials are used, such as milk [80] or intralipid®[81]. However, these are materials tipically showing instability over time, and this feature was unsuitable for

our experiment, since the whole experiment took a few months of work. For this reason we have preferred to fabricate our dynamic phantom by using stables materials (EPE, air, and stainless steel), to have good reproducibility of the experimental tests.

In any case, a good understanding of the optical data obtained on such phantom requires a detailed characterization of the light scattering phenomena in the EPE media. To investigate such aspect we performed reflectivity and time-of-flight measurements of the EPE phantom by varying the SDS. In the following we describe the performed experiment and the data analysis procedures.

## *5.5 Time-correlated single photon counting technique (TCSPC)*

Time-correlated single photon counting (TCSPC) is based on the detection of single photons of a periodically pulsed light signal, the measurement of the detection times, and the reconstruction of the waveform from the individual time measurements [82, 83].

TCSPC technique is based on the fact that for low-level, high-repetition rate signals the light intensity is low enough that the probability to detect more than one photon in one signal period is negligible. The situation is illustrated in figure 5.4 for the case of a fluorescence signal [84].

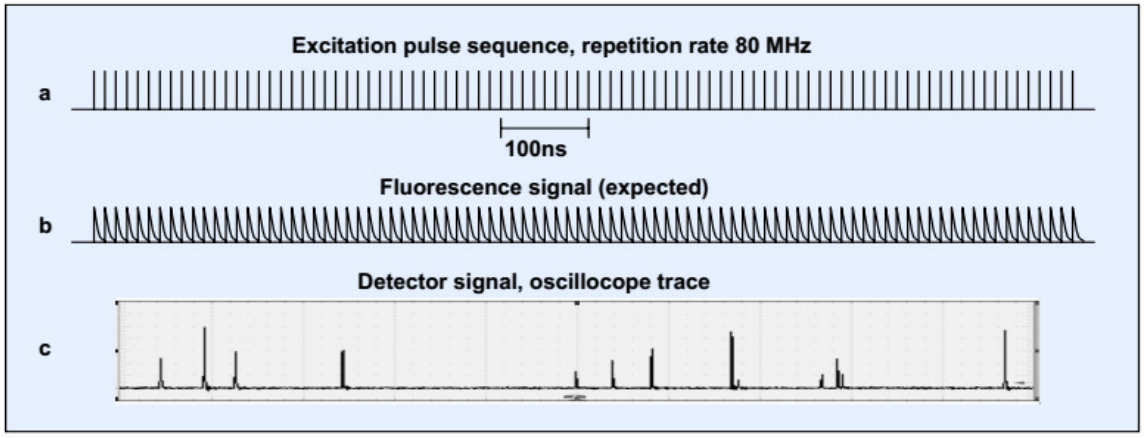


**Figure 5.4:** Detector signal for fluorescence detection at a pulse repetition rate of 80 MHz. See the text for further explanation of sub-figures a,b,c. [84]

Fluorescence of a sample is excited by a laser of 80 MHz pulse repetition rate as in figure 5.4 (a). The expected fluorescence waveform is shown in figure 5.4 (b). However, the detector signal, (as measured by an oscilloscope) has no similarity

with the expected fluorescence waveform. Instead, it is a sequence of extremely narrow pulses randomly spread over the time axis as shown in figure 5.4 (c). There is a simple explanation to the odd signal shape: the pulses represent single photons of the light signal arriving at the detector. The shape of the pulses has nothing to do with the waveform of the light signal: it is the response of the detector to the detection of a single photon. The amplitude jitter, or *gain noise*, clearly visible in figure 5.4 (c), is a result of the random amplification process in detectors such as PMTs. It is present in all high-gain detectors such as SiPMs.

In analog techniques the gain noise contributes to the noise of the measurement. Photon counting results are free of gain noise, because the final waveform is built up from the photons time distribution after an exitation pulse. Therefore, the waveform of the optical signal is not the detector signal. Instead, it is the distribution of the detector pulses over the time in the excitation pulse periods. The detection of a photon within a particular excitation pulse period is a relatively unlikely event. The detection of two or more photons is even more unlikely. Therefore, only the first photon within a particular pulse period has to be considered. The process of the building-up of the photon distribution over the pulse period is shown in figure 5.5.

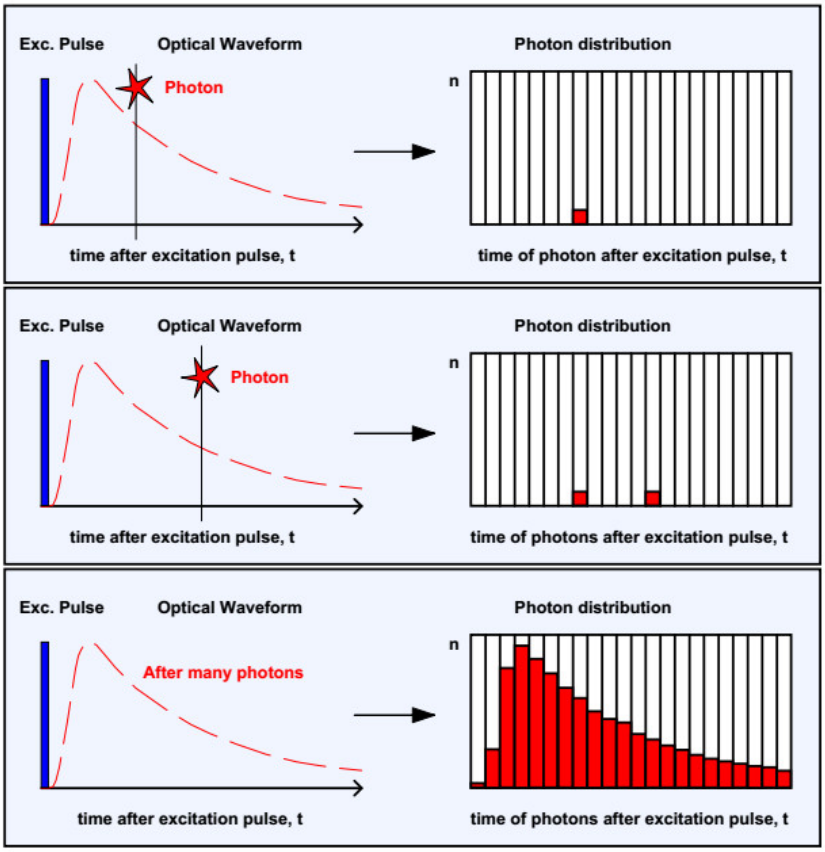


**Figure 5.5:** Principle of TCSPC. The recording process build up the distribution of the photons over their times after the excitation pulse [84]

When a photon is detected, the arrival time of the corresponding detector pulse in the signal period is measured. The events are collected in memory by adding a '1' in a memory location related to the detection time. After many signal periods a large number of photons has been detected, and the distribution of the photons over the time in the signal period builds up.

By dividing the period in a large number of narrow instants, the arrival time of a photon pulse can be determined with high precision. The bandwidth of a photon counting experiment is limited only by the transit time spread of the pulses in the detector, not by the width of the pulses which can depend on the detector characteristics. The transit-time distribution is usually an order of magnitude narrower than the width of the single-photon pulses. For the same detector, photon counting therefore obtains a significantly higher time-resolution than any analog recording technique. This feature is more or less inherent to all photon counting techniques, but is found in extreme form in time correlated single photon counting, or TCSPC.

In this work the SPC-130 board from Becker & Hickl (Germany) has been used for time of flight measurements (TOF). The board, shown in figure 5.6, is a single channel board with a first input for the reference trigger and a second input for the detector.

**Figure 5.6**: SPC-130 board

The architecture of the board can be semplified and explained by means of a blocks diagram, shown in figure 5.7. The two inputs of the board are monitored by dedicated "Constant Fraction Discriminator" (CFD) blocks to determine the timing of the pulses minimizing the timing jitter typical of classic leading-edge discriminators. The CFD triggers at a constant fraction of the pulse amplitude, avoiding pulse-height induced timing jitter.

The output pulses of the two CFDs are used as start and stop pulses of a time-to amplitude converter (TAC). The TAC output is a voltage proportional to the time between the start pulse and the stop pulse.

The board supports the Reversed start-stop configuration for TCSPC. In this configuration, the TAC is started when a photon is detected and stopped with the next reference pulse from the light source. Throug this optimization, the TAC has to work only at the rate of the less likely photon detection events, not at the much higher rate of the exitation pulses. The TAC output voltage decreases for increasing arrival times of the photons, then it is amplified (by the AMP block) and read by the ADC (Analog to Digital converter) which addresses the counting to the right time slot in memory.

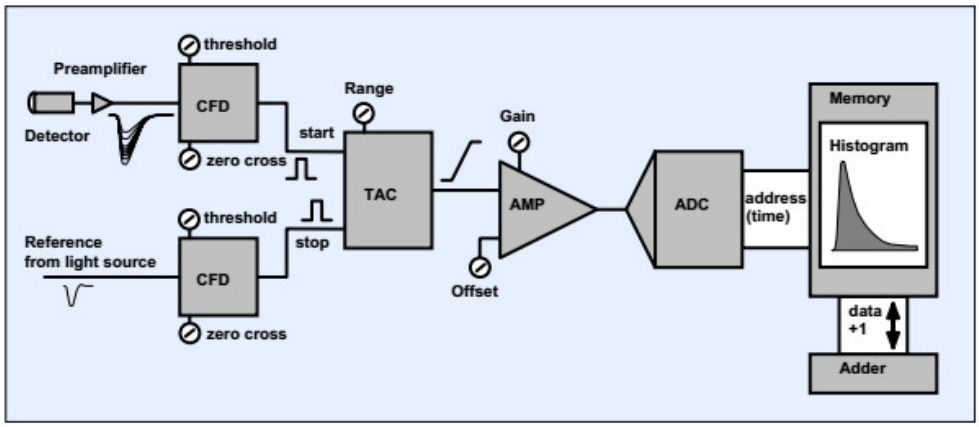


**Figure 5.7**: Block diagram of the used TCSPC module architecture in reversed start-stop configuration [84].

For the TOF measurements presented in this work, a MICRORB-10035 SiPM by ON Semiconductor [85], mounted on a printed circuit board (MICRORB–SMA) has been used (figure 5.8). The fast output pin of the RB10035 has been connected to a 26 dB preamplifier (figure 5.9) and the output of the preamplifier has been connected to the dedicated input of the TCSPC module. A 760 nm pulsed laser by PicoQuant with < 90 ps pulse Full Width at Half Maximum (FWHM) was used as light source. Its trigger has been connected to the dedicated input of the TCSPC board.


**Figure 5.8**: On Semiconductor MICRORB-10035 SiPM mounted on the MICRORB–SMA printed circuit board [85]


**Figure 5.9**: Becker & Hill HFAC preamplifier. Main characteristics of this device: 26 dB amplification with cutoff frequency of 1.6 GHz [84]

The time resolution of an analog signal recording technique is limited by the bandwidth of the detector. The width of the instrument response function cannot be shorter than the 'single electron response', or 'SER' (represented in figure 5.10, center). For TCSPC the time resolution is much better. The explanation is given in figure 5.10.

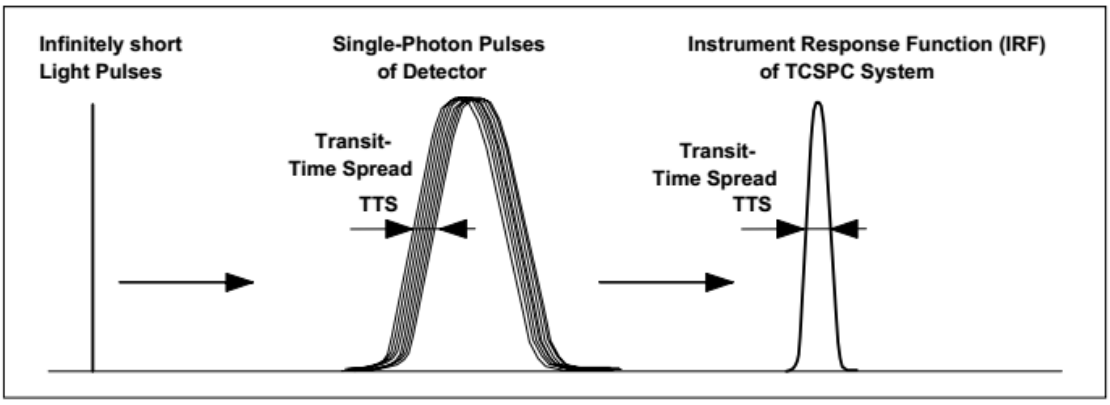


**Figure 5.10**: Response of detector to infinitely short light pulses and instrument response of TCSPC system [84]

The times of the photons are derived from the arrival times of the detector pulses. These times can be measured at an accuracy much better than the width of the pulses. Thus, the 'instrument response function', or IRF, of a TCSPC system is essentially given by the transit time dispersion (or transit time spread, TTS) of the photon pulses in the detector. The TTS can be more than 10 times shorter than the single photon response of the detector. The IRF is therefore much narrower than the SER, see figure 5.10, right.

To prove the above argumentation, an experiment has been carried out using the presented instrumentation. In figure 5.11, four different curves are shown in logarithmic scale to facilitate the visualization. In green is represented the IRF of the instrument, considering the hardware configuration, the used laser and the used photodetector. The total IRF is the convolution of all component IRFs. The approximation of the IRF with a Gaussian curve is shown in blue. Time of flight measurements has been performed on a phantom made of a scattering medium and the results are shown in red. This curve is the convolution of the IRF and the effective data to be measured. Since, as mentioned above, the IRF is much narrower, the deconvolution of the measured data, considering the IRF approximation (shown in black) does not add any particular information since it is very similar with the raw data.

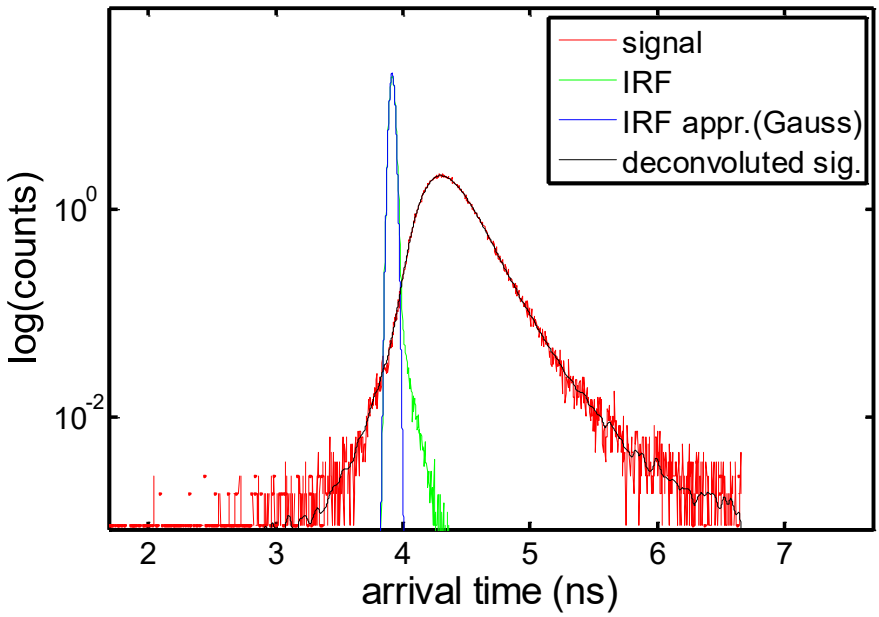


**Figure 5.11**: recorded IRF (green) and Time of Flight measurement (red) on an EPE slab. The IRF gaussian approximation (blue) has been used to calculate the deconvolution of the signal (black).

The red curve is a photon distribution typical of a diffusive medium. As shown in figure 5.12, scattering and absorption have a characteristic effect on the shape of the response to a pulse transmitted through a thick medium.

The sketch of Fig. 5.12 provides a graphical explanation on why the TOF measurements, contrarily to the steady-state reflectivity measurements, can distinguish very well among light scattering and light absorption: On the left,

scattering increases and therefore the photon arrival time distribution function shifts towards increasing times and larger full widths at half maximum. On the right it is the light absorption which is increasing, and it is evident that the photon distribution peak intensity decreases.

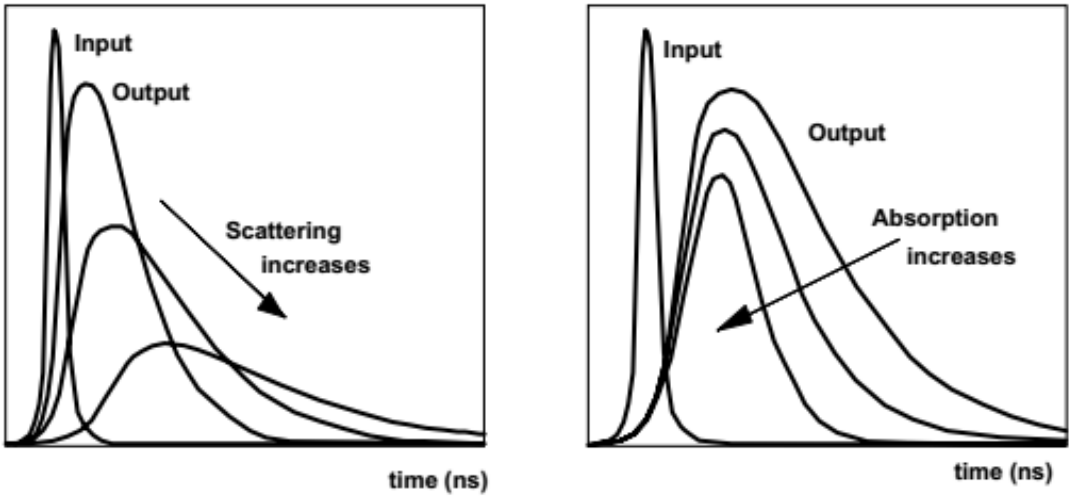


**Figure 5.12**: Effect of scattering and absorption on the shape of a pulse transmitted through a thick medium [84].

## *5.6 Measurement of the Optical Properties of the EPE layer*

Reflectivity measurements have been performed on two phantoms: phantom 1 is a 50 cm × 40 cm × 6 cm EPE slab with no air gap while phantom 2 is the multilayer phantom used in other sections of this work, made of an EPE slab of 50 cm × 40 cm × 3 cm, on a 3 cm air gap, and on a second EPE slab of 50 cm × 40 cm × 3 cm. The scheme of the setup used in reflectivity and TOF measurements is shown in figure 5.13. A NIR light source has been positioned on the surface of the phantoms, far from the other boundaries. The detector is positioned near the source at a different distance for each measurement.

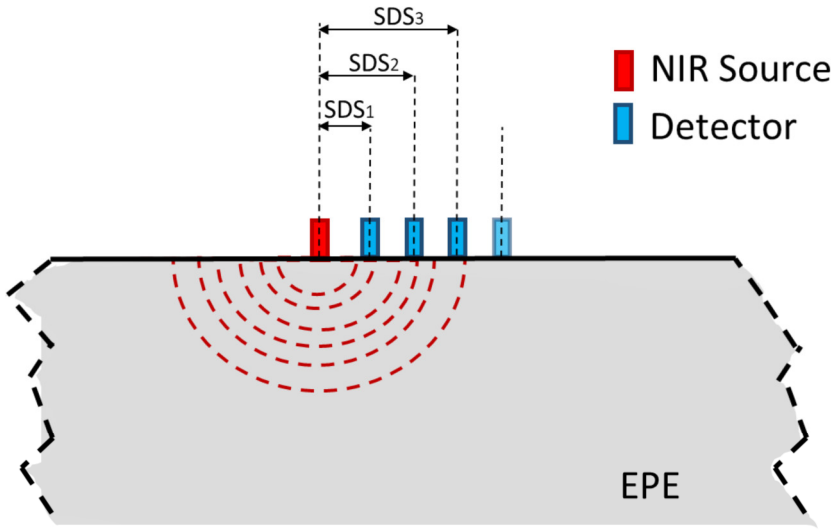


**Figure 5.13.** Scheme of the setup used for reflectivity and time-of flight measurements. In the case of reflectivity, LEDs at 700 and 830 nm has been used as sources. In the case of TOF measurements, the light source used is a 760 nm pulsed laser.

Figure 5.14 reports the comparison of near-infrared light back diffusion for the two types of phantom. The measurements were taken by the voltage drop across a 50 Ω resistor in series to a single SiPM detector illuminated alternatively by two LEDs (700 nm and 830 nm wavelengths) both biased at a fixed current of 1.40 μA and mounted on a board with an inter-LED distance of 2 mm. The comparison of the measurements taken at different SDSs on phantom 1 and phantom 2 shown in Figure 5.14 confirms that the air gap does give a contribution in terms of optical power reaching the photodetector: the CW photocurrents in phantom 2 are in fact somewhat lower.

The data of Figure 5.14 in the case of the phantom 1 (compact EPE slab with no air gap) can be analyzed with a simple analytical model. In particular, from these data, we can obtain the effective attenuation coefficient using the photocurrent slope [86].

In back-scattering measurements, on which the CW-fNIRS principle of operation is often based, the light diffusion transport is modeled by using the modified Lambert–Beer law:

$$I(\lambda) = I_0(\lambda) \exp[-\mu_\alpha(\lambda) \cdot SDS \cdot DPF(\lambda) + G(\lambda)] \quad (5.1)$$

where $I(\lambda)$ is the measured wavelength-dependent diffused reflected light intensity, $I_0(\lambda)$ is the incident light intensity, $\mu_a(\lambda)$ is the absorption coefficient,

*DPF(λ)* is the differential path length factor, and *G(λ)* is a wavelength-, medium-, and geometry-dependent constant.

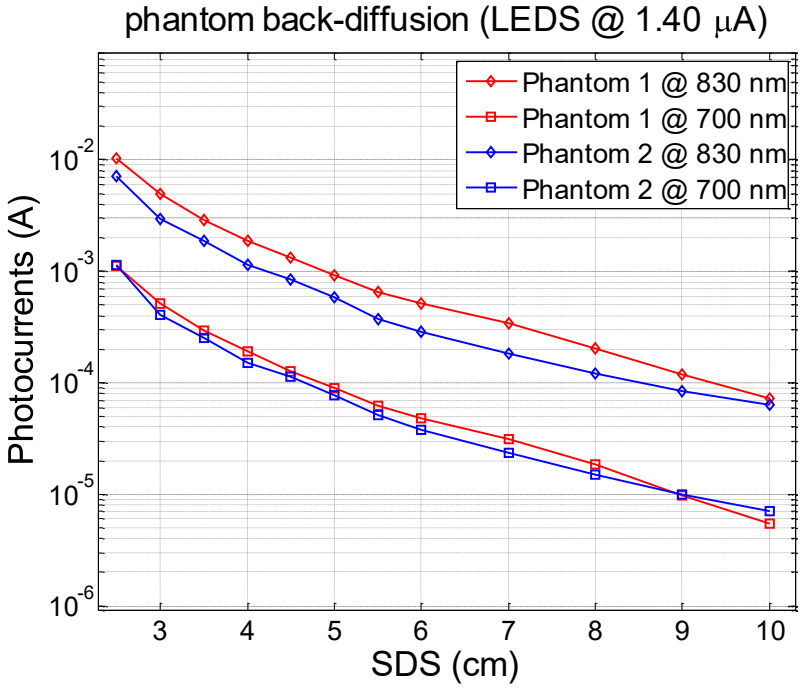


**Figure 5.14.** SiPM photocurrents measured on the phantoms at multiple source detector separations (SDSs) under 700 nm and 830 nm illumination.

*DPF(λ)* is a scaling factor shown to be approximately equal to $\frac{1}{2}\sqrt{3\mu_s'/\mu_a}$ [26]. Hence, $I(\lambda)$ can be rewritten as

$$I(\lambda) = k \cdot \exp\left[-\sqrt{3 \cdot \mu_a(\lambda) \cdot \mu_s'(\lambda)} \cdot \frac{SDS}{2}\right] \tag{5.2}$$

a decreasing exponential function of SDS.

Therefore, thorough the Beer-Lambert model, we estimate that the EPE layer $\sqrt{\mu_a \cdot \mu_s'}$ is approximately 0.53 cm$^{-1}$, relatively close to the human brain cortex tissues for which the $\sqrt{\mu_a \cdot \mu_s'}$ values are about 1 cm$^{-1}$ in the near-infrared (NIR) range.

Such evaluation of the $\sqrt{\mu_a \cdot \mu_s'}$ is clearly very useful to have first evaluation of the EPE material scattering properties, but it is insufficient. In fact, the knowledge of the two separate parameters $\mu_a$ and $\mu_s'$ is necessary, since the light scattering properties of the EPE material are determined by the separate contribution of these two parameters. The separate measurement of the two parameters $\mu_a$ and $\mu_s'$ is

possible by coupling the reflectivity data as a function of SDS of Figure 5.14 to measurements of time-of-flight (TOF) in phantom 1.

For this purpose, we collected TOF data at nine different SDS values measured on phantom 1 considering the experimental setup shown in figure 5.13. The TOF measurements instrumentations and setup is expounded in the previous section.

Figure 5.15 reports the <t> vs. $d$ data measured on phantom 1 (black connected points). In the same graph, we also report theoretical <t> vs. d curves evaluated by Equations (2.13) and (2.14) shown in chapeter 2 (Arridge et al. [32]) for $\mu_a$values varying from 0.01 $cm^{-1}$ to 10 $cm^{-1}$ at a step of 0.01 $cm^{-1}$, and by imposing that $\sqrt{\mu_a \cdot \mu_s'}$ = 0.53 $cm^{-1}$, as required by the data of Figure 3 (colored continuous lines). The best fit of the model to the data occurs for $\mu_a \approx 0.1$ $cm^{-1}$ and $\mu_s' \approx 2.8$ $cm^{-1}$.

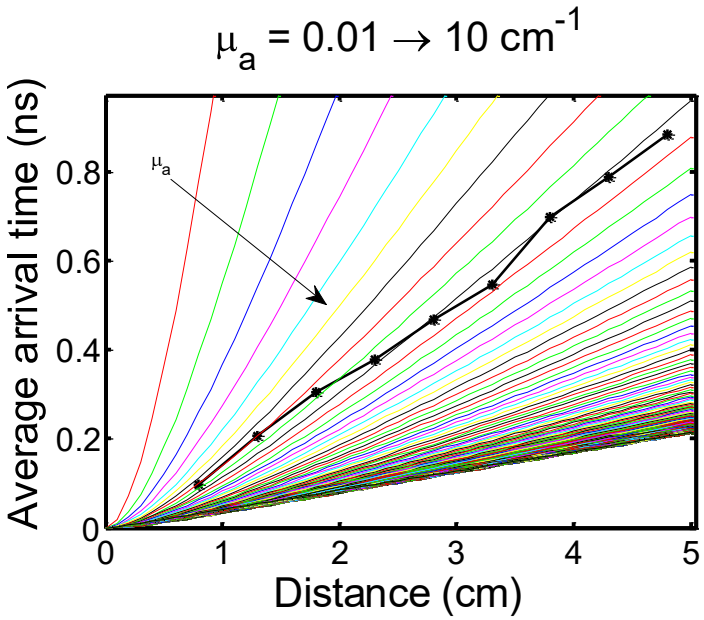


**Figure 5.15:** Average arrival time of photons: theoretical (colored continuous lines) and measured in back diffusion configuration on the phantom (black connected points).

The shown method is useful to provide the evaluation of absorption and scattering values of a material with certain characteristics and under certain hypoteses. Despite this, the method presents some critical points. First of all, the use of approximate forms for the expression of photon density in function of distance from light source, scattering and absorption in a material leads to errors in the determination of $\sqrt{\mu_a \cdot \mu_s'}$.

Furthermore, small errors in the estimation of the slope of a photon density curve, leads to large errors on the estimation of $\mu_a$ and $\mu_s'$ parameters. Finally, the

hypotheses necessary for the use of an approximate form such as the Beer-Lambert law, or an ideal form such as the more general Diffusion Theory equations, limit the use of this method to homogeneous materials with $\mu_s' >> \mu_a$ and force reflectivity and time-of-flight measurements to be performed in difficult conditions such as the immersion of the light source and the photodetector in the medium under analysis.

Moreover, in the case of dishomogeneous materials, such in the case of our dynamic phatom, which has an air-gap in the middle where no light scattering takes place, light trasport deviates very heavily from the condition of scattering dominated transport.

For these reasons, we need a more robust model of light transport, which takes into account both the regions dominated by scattering (the EPE layers) and the regions where no light scattering takes place (the air gap). This is a Monte Carlo model, defined in the MATLAB® environment, described in the next section.

## *5.7 Light transport in the dynamic phantom analyzed by using the Monte Carlo method*

The Photon migration in a scattering medium is a typical example of complex problem to be solved with statistics based computational methods. When the volume in wich photons move has a complex inhomogeneous structure, the Monte Carlo method represents a preferential way to generate solutions to photon distribution problems [87]. The algorithms generally work by launching a large number of indipendent threads each one simulating the behaviour of a single photon with its statistical distributed parameters. In this work, a custom Monte Carlo algorithm is presented in order to find photon distribution solutions in different cases occurring in a complex multilayered phantom when NIR light sources and photodetectors are located on its surface. The implemented simulation works as illustrated by the block diagram in figure 5.16.

The geometrical characteristics and the spatial dependent optical definition of the phantom in terms of refractive index, absorption and reduced scattering coefficients (considering a fixed wavelength in NIR spectrum) are passed to the algorithm. This algorithm launches a given number of threads, each one simulating the sequence of a photon migration from the photon initial status to a final status characterized by an absorption event or by the exit from the phantom geometrical borders.

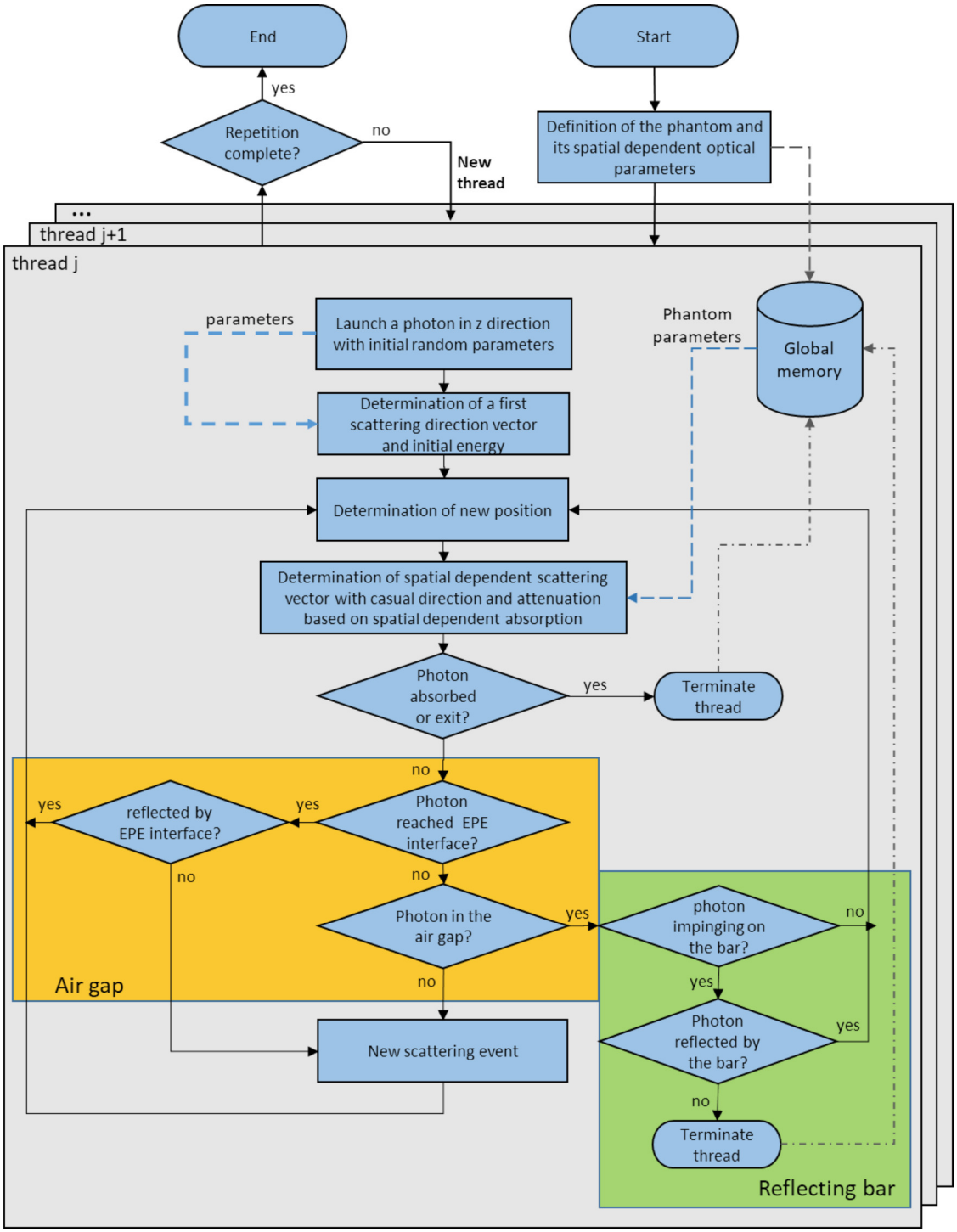


**Figure 5.16.** Block diagram of the implemented Monte Carlo simulation.
Yellow rectangle contains the instructions related to the air gap managing.
Green rectangle contains the instructions about the partially reflecting bar managing.
The instructions in colored rectangles can be skipped depending
on the phantom geometrical – optical definition.

The light source is located on the first EPE layer surface of the phantom. At launch, the algorithm assigns to the photon its initial direction (z), and a casual exponential distributed value for initial absorption length and initial scattering vector, based on the optical characteristics $\mu_s'$ and $\mu_a$ assigned to the phantom first layer. The value of the assigned initial attenuation is 1. By these parameters, the algorithm determines a new geometrical position of the photon in the phantom volume. Considering the phantom optical and geometrical definition stored in memory, the optical parameters in the new location in the phantom are calculated and the new status for the photon is determined. The intensity of the photon is updated considering the attenuation occurring during the movement in a medium characterized by a certain absorption coefficient. A scattering vector is assigned considering a casually determined scattering angle and the reduced scattering coefficient of the medium in the new position in the phantom. If this new position is located outside the phantom borders and the photon is not reflected by the boundaries, or if the photon intensity has reduced to a value lower than a random number extracted in the 0-1 interval, the thread ends and the final position and final status of the photon are stored in the global memory, in terms of attenuation, angle of exit, time of flight, number of iterations, etc. Contrarily, if the photon is not absorbed and its position is inside the phantom, the algorithm simulates new scattering event and a new position is established, a new status is determined based on the phantom optical characteristics and the cycle is repeated as explained above.

The algorithm can be tailored to simulate inhomogeneous phantoms with air gap and reflecting objects located between the layers in the air gap. Figure 5.16 shows two colored boxes in the block diagram. The colored rectangles contain instructions about air gap and reflecting objects: they can be skipped depending on the phantom geometrical definition.

The Monte Carlo method implemented to determine the optical parameters of a material operates a simulation of a popolation of 100,000 photons starting from a photon source located on the surface of a 6 cm thick, 20 cm width and 20 cm length homogeneous medium with certain optical characteristics and no air gap.

The refractive index of the simulated medium is fixed at 1.4, while $\mu_s'$ and $\mu_a$ values are 0.5, 1, 2.5, 5, 10 $cm^{-1}$ and 0.05 and 0.1 $cm^{-1}$ respectively for different light diffusion simulations. As explained above, after every single simulation, different parameters can be obtained: number of photon back-reflected absorbed or and transmitted, exit angle, number of iterations, photon density at different distances from the light source, time of flight of back-reflected photons.

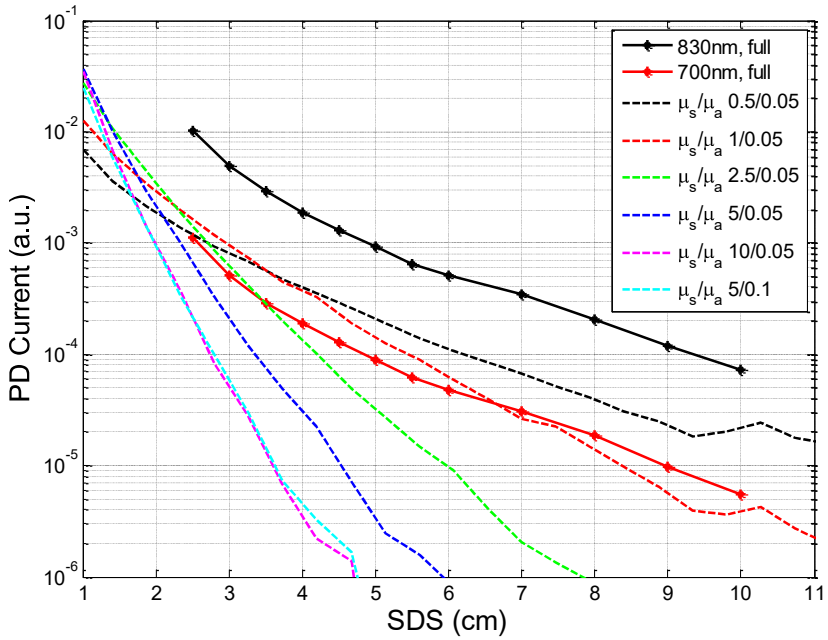


**Figure 5.17.** SiPM photocurrents measured on the phantom at multiple source detector separations (SDSs) under 700 nm and 830 nm illumination (connected points) and photon densities at multiple distances calculated by Monte Carlo simulations for different $\mu_s'$ and $\mu_a$.

Figure 5.17 shows the same measured data represented in figure 5.14 compared to the output of 6 Monte Carlo simulations related to 6 different scattering materials characterized by $\mu_s'$ and $\mu_a$. It can be seen that at $\frac{\mu_s'}{\mu_a}$ = 0.5/0.05 and $\frac{\mu_s'}{\mu_a}$ = 1/0.05, the Monte Carlo simulations fit quite well the slope of measured data.

However, figure 5.18 clearly shows that the simulated medium with $\mu_s'$ = 1 cm$^{-1}$ and $\mu_a$ = 0.05 cm$^{-1}$ has the best fit in terms of dependence of distance from the light source of the back-freflected photons time of flight.

The $\mu_s'$ and $\mu_a$ values of the EPE layer found by fitting the experimental data to the MC model, $\mu_s'$ = 1 cm$^{-1}$ and $\mu_a$ = 0.05 cm$^{-1}$, are quite different from those found by using the analytical models (modified Beer-Lambert and the TOF by Arridge), which are $\mu_s'$ ≈ 2.8 cm$^{-1}$ and $\mu_a$ ≈ 0.1 cm$^{-1}$. The reasons for such remarkable difference are probably due to the light injection: in this experiment the light source is not point-like and it is located on the surface instead of inside the material by means of optical fibers. However, such difference is unclear at the moment, and we are trying to deepen such issue.

In any case, compared to the parameters values of the human head tissues, the EPE phantom shows $\mu_a$ and a $\mu_s'$ about one order of magnitude lower, making the phantom relatively more "transparent" in the NIR range compared to the human tissues.

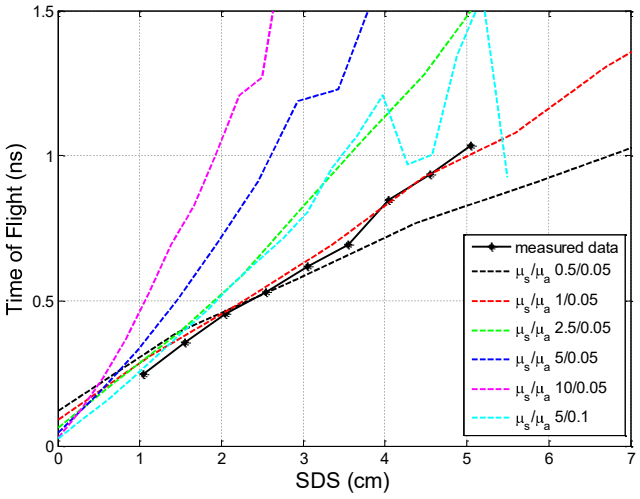


**Figure 5.18:** Average arrival time of photons measured in back diffusion configuration on the phantom (black connected points) and Monte Carlo simulation (colored dashed lines) for different $\mu_s'$ and $\mu_a$.

## *5.8 Monte Carlo simulation of the system response to the dynamic phantom*

The dynamic phantom described in section 5.4 is equipped with a stainless steel bar moved in the air gap by a stepper motor at a fixed angular velocity. The realized sensor system measures the back reflected light of 12 multiplexed double wavelength LEDs by means of 13 SiPMs. The system has to be able to detect and localize the bar by the measurement of back-scattered photons on the phantom surface. What is the expected system response to the bar motion?

The Monte Carlo simulation is useful to understand and forecast the trend of the sensor photocurrent signals. For this purpose, Monte Carlo simulations have been implemented by simulating a population of 100,000 photons starting from a photon source located on the surface of a 20 cm width and 20 cm length phantom with two 3 cm thick homogeneous layers with $\mu_s'$ = 1 cm$^{-1}$ and $\mu_a$ = 0.05 cm$^{-1}$, detached by a 3 cm thick air gap. For this purpose, the Monte Carlo code has been slightly complicated to take into account the presence of the mid air-gap. In particular, the simulation has been integrated with the instructions contained in the colored boxes shown in the block diagram in figure 5.16. If the photon is not absorbed neither scattered away from the phantom volume, after the determination of a new photon position, the algorithm controls if the photon has reached the interface between the scattering material and the air.

If the photon location is in the interface, the computation of reflection and refraction occurs in both cases: NIR photon moving from the EPE material toward

the air and from air toward the EPE. The reflectance is calculated taking into account the optical properties of the air and the medium and the photon incidence angle with respect to the line perpendicular to the interface at the point of incidence. We used the Fresnel equations, and we took the average of transverse magnetic (TM) and transverse electric (TE) modes since the light is unpolarized. An example of how the reflectance is calculated is shown in figure 5.19.

For example, in the case of a photon moving from the air towards the EPE, the algorithm generates a random number between 0 and 1 with uniform probability distribution (R = 0.5) and if this number is lower than the computed reflectance, and the angle of incidence is greater than the computed critical angle, then the photon is reflected.

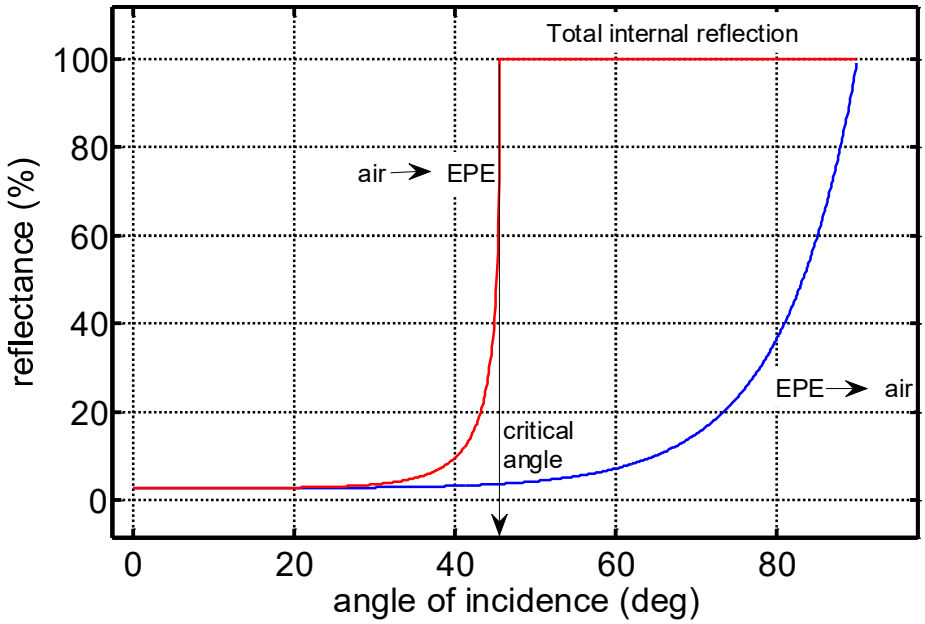


**Figure 5.19.** Reflectance in function of incidence angle for a NIR photon moving from air (refractive index = 1) towards EPE (refractive index = 1.4). In red is showed the reflectance for a photon moving from EPE to air.

On the other hand, if the random number is greater than the computed reflectance and the angle of incidece is smaller than the critical angle, then the photon is transmitted and refracted according to Snell and Fresnel laws. The implemented software is programmed to compute the reflection and its probability even in the case of a NIR photon moving from the EPE towards the air gap.

In the case of transmission in the air, the photon is projected forward to the opposite interface between air and EPE or to the surface of an object located in the air gap, if present in the phantom definition stored in memory.

When the computed position of the photon is located in the air gap, the algorithm determines if the photon impinges the bar. Instructions contained in the green box of the block diagram in figure 5.16 are executed. A NIR photon impinging the bar can be reflected or absorbed or scattered in horizontal direction in the air, outside the phantom volume. The algorithm manages all these possibilities taking into account the reflectivity of the object.

Two Monte Carlo simulations have been launched, considering the multilayered phantom with a source of photons located on the top of the EPE layer in the first case and a source of photons located in the middle of the air gap.

The multilayered phantom can be considered symmetrical along the two horizontal directions. Under this hypothesis, fixed a reference point on the surface, the location of a generic point of the phantom can be expressed in cylindrical coordinates: depth and radius. In figure 5.20 (a), the logarithm of the photon density extimated by the Monte Carlo simulation is shown in colormap in function of depth and radius with respect to the position of a LED located on the phantom surface. The effect of the air gap and the boundaries of the EPE layers on the photon density are clearly visible considering the depths of interest 3 cm and 6 cm: photons reflect on the surfaces and their density is higher. This effect is also visible at the phantom surface. In figure 5.20 (b) the logarithm of the average photon density is shown in cylindrical coordinates when the photon source is located in the middle of the air gap at radius 0 and depth 4.5 cm with respect to the origin.

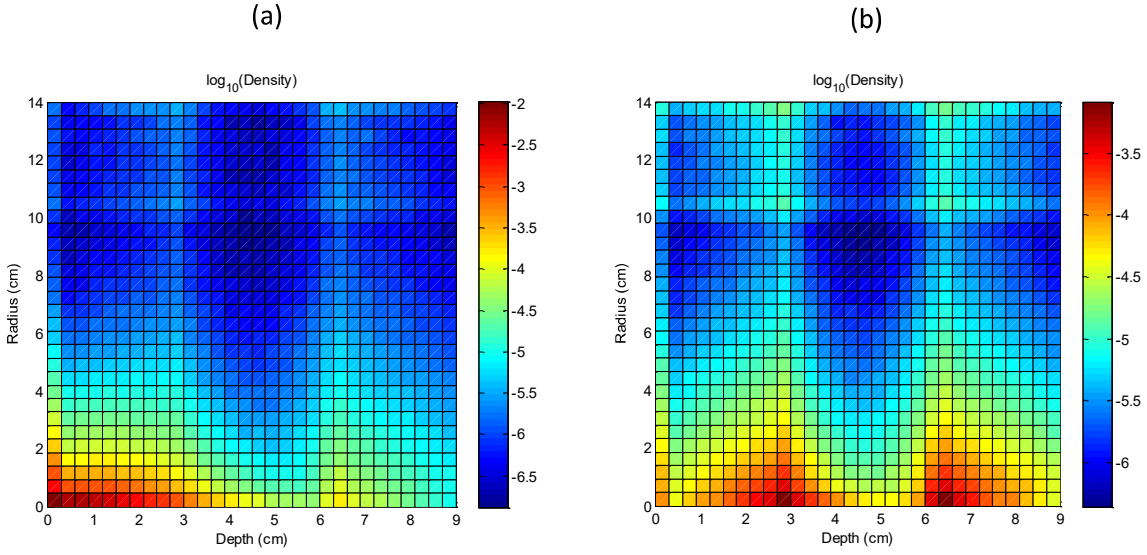


**Figure 5.20.** Photon density in function of depth and radius when:
a) a source of photons is located on the origin (0, 0) on the multilayered phantom surface,
b) a source of photons is located in the middle of the air gap.

Figure 5.21 shows the photon density at the surface obtained by a number of Monte Carlo simulations considering the light source on the top of the phantom and different objects in the air gap. The photon density at the phantom surface is a crucial parameter in the context of fNIRS and DOT, since the measured phenomena is the back reflection of light. It is evident that the average photon density at the surface of the phantom varies when different rods with different reflectivity and dimensions are placed under the light source in the air gap (depth = 4.5 cm, radius = 0). The larger is the bar, the larger is the variation of photon density.

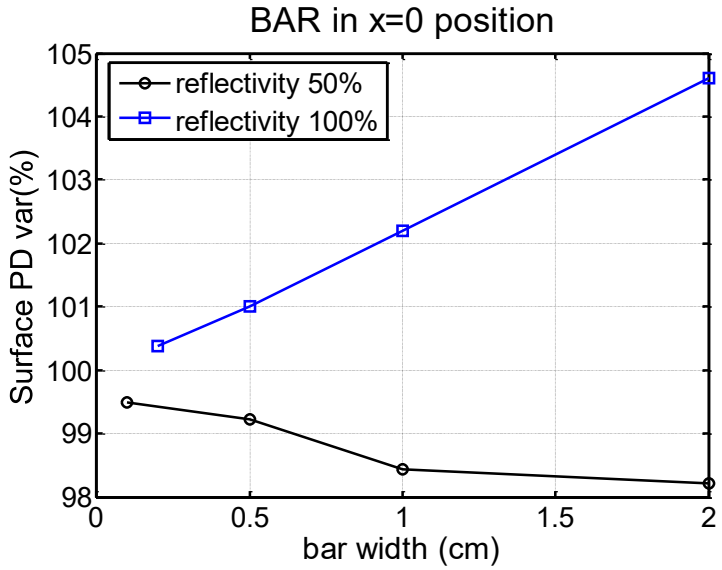


**Figure 5.21:** Monte Carlo simulation output:
average photon density on the phantom surface
when metal bars with 50% reflectivity and different dimensions
are located under the light source in the air gap (z = 4.5 cm)

The sign of this variation is related to the bar reflectivity: when the bar is characterized by a 100% reflectivity, the photons impinging its surface have a quite large probability of being back-reflected to the phantom surface. In this case, the photon density on the phantom surface has an increase with respect to the absence of the rod. Contrarily, photons impinging on a bar with a 50% reflectivity (and 50% absorbance) can be reflected, absorbed or scattered in horizontal directions, reducing the probability of being back scattered toward the phantom surface. A reflectivity of 50% - 60% is in fact that of the stainless steel (the material of the metal bar in our dynamic phantom) in the NIR range [88].

Another aspect, evaluable by implementing Monte Carlo simulations, is the combined effect of reflectivity and shading on photon density variation on the

surface and under the air gap of the inhomogeneous phantom with respect to the position of a partially reflecting object located in the air gap. The results of Monte Carlo simulations in figure 5.22 (a), despite the error bars (whose size is the numerical accuracy of our MC calculation), exhibit a particular trend in terms of photon density variations on the phantom surface: the presence a 50% reflectivity rod under the light source (radius = 0) causes a little decreasing of the average photon density. The effect of the movement of the bar in the air gap at fixed depth is a further decrease due to a shadow casted by the bar. When the bar reaches a distance large enough, the average photon density at phantom surface starts increasing again. At 6.5 cm depth, figure 5.22 (b) shows a low photon density level due to the shadow casted by the partially reflecting bar located under the light source. When the rod moves away from the initial position at radius = 0, the average photon density starts increasing reaching the reference level that characterizes the absence of objects in the air gap.

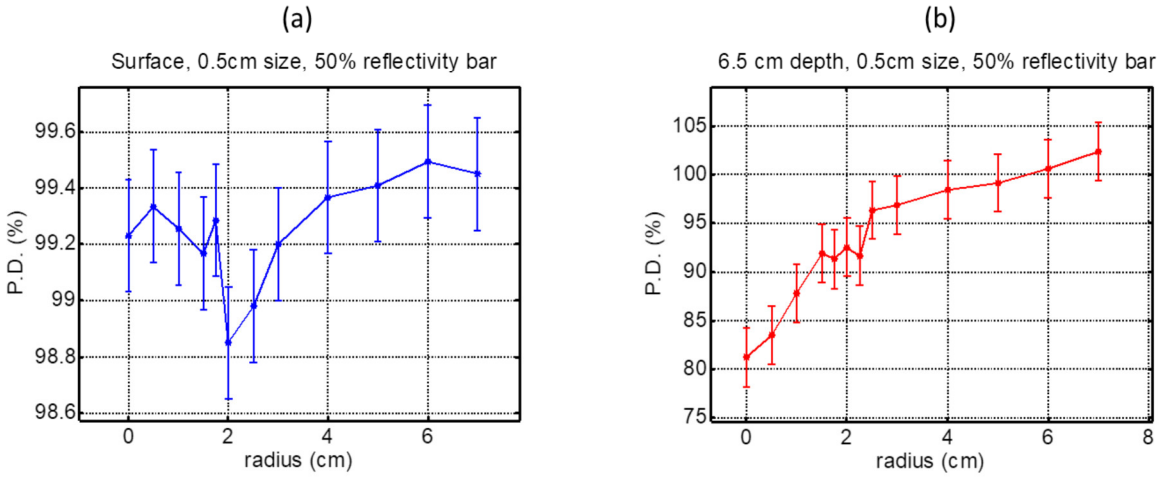


**Figure 5.22:** Monte Carlo simulation output:
(a) average photon density variations in the phantom on the surface
when a 5 mm width 50% reflecting bar is located in the air gap (z = 4.5 cm)
at different radiuses with respect the position of the light source;
(b) average photon density variations at 6.5 cm depth under the surface.

With these considerations, for each channel, consisting of a light source and a photodetector both located on the phantom surface, a reverse bell shaped time dependent signal is expected when a moving 50% reflectivity metal bar (R = 0.5) passes slowly through the air gap.

Nevertheless, the moving rod and its reflectivity are not the only phenomena that contribute to photodetectors signal formation: without any other consideration, a

small amount ($10^{-4} - 10^{-5}$) of percentage variation is expected at the sensors output, since the sensor only detect photons impinging its active area and cannot monitor the average photon density variation on the whole phantom surface.

As explained in the previous chapters, a perturbation method within the Diffusion Theory can assess the influence of a perturbing object located in a scattering medium [30]. Considering a light source and a negative perturbing object (i.e. a region with higher absorption) located in a homogeneous medium, the perturbation method asserts that in the region around the object, the photon fluence distribution is negatively perturbed by the object and a perturbing shadow is casted downstream from the light source, beyond the object. This effect is even more evident in an air gap with very low scattering effects, and it occurs even in the case of partially reflecting objects: photons impinging on the bar surface can be reflected again in the medium toward the sensor, or can be scattered in horizontal directions in the air gap or can be absorbed and never detected. In any case, a few photons can reach the second EPE layer under the rod and a shadow is casted. Photons coming from below scattered or reflected by the surface of the second EPE layer can be also absorbed or scattered horizontally far from the photodetectors matrix because of the presence of the bar. In short, the phantom volume portions affected by the shadow have a great impact on the number of photons that can return to the surface to be detected after scattering phenomena, and this "shadow effect" is the main cause of the photodetectors signals variation.

In order to reconstruct the photodetector signal, 52 time instants have been defined and the volume of the phantom has been divided into small *voxels*. A 5 mm width bar with 50% reflectivity (R = 0.5) completely covering the phantom length, is shifted by 1 voxel every instant in positive $x$ direction.

The method used to reconstruct the photodetectors signals is similar to the definition of the direct problem in the context of the Diffuse Optical Tomography [89]. In our simulation, a mesh of $N = 61731$ voxels, each one sized 5 mm × 5 mm × 5 mm is defined. The generic measurement $y_{sd}(t)$ that is related to a light source $s$ and to a photodetector $d$, both located at the boundary of the domain (on the phantom surface) at a fixed time instant $t$, is proportional to the sum of each contribute of each voxel $v_p$ to the photon density at the photodetector location:

$$y_{sd}(t) \propto \sum_{p=1}^{N} T_{s \to v_p}(t) \cdot T_{v_p \to d}(t) \tag{5.3}$$

where $T_{s \to v_p}$ is the transport factor from the source $s$ to the voxel $p$ and $T_{v_p \to s}$ is the transport factor from the voxel $v_p$ to the detector $d$. As seen in the previous chapters,

the transport $T$ equals $\varphi/P$ and at fixed $P$, $T$ is proportional to the concentration of optical energy. Therefore, the transport factors are evaluated by Monte Carlo simulation for each channel considering the photon densities expressed as a function of depth and radius shown in figure 5.20. Depending on the time related position of the rod in the phantom, each voxel can contribute in three different ways, as explained below:

1) The voxel $v_p$ is not involved in the presence of the bar. In this case, our software calculates two couples of cylindrical coordinates to determine the relative position of the voxel $p$ with respect to the light source position and with respect to the photodetector position. Known radius and depth of the voxel, the term $T_{s\to v_p}(t)$ is determined considering the photon density shown in figure 5.20 (a), calculated by Monte Carlo simulation in the case in which the light source is located on the phantom surface. Assuming the reciprocity principle within the adjoint method [Arridge part 2], the measurement of photon flux at voxel $p$ that is due to an isotropic source at position ($r_s$,$d_s$) is equal to the measurement of the photon density at ($r_s$,$d_s$) that is attributable to a source at the position of voxel $p$, provided that the source is created by the application of the adjoint operator. Under this hypothesis, the term $T_{v_p\to d}(t)$ can be determined by Monte Carlo simulation considering the photon density shown in figure 5.20 (a) in which the photodetector is located at the coordinates $r_d = 0$ and $d_d = 0$ instead of the light source.
2) The voxel $v_p$ is characterized by the presence of the partially reflecting bar. The transport from the photon source to the voxel position is calculated in the same way of the previous case. The perturbation method [30] asserts that a voxel with negative perturbing effect (absorber) in a homogeneous medium contributes to the total transport as a voxel with no changes in optical parameters and its transport has to be multiplied by its incremental change in absorption $\Delta\mu_a$. However, the metal rod is not a pure absorber and its changes in optical parameters are not incremental with respect to the medium. Therefore, a further Monte Carlo simulation has been implemented to evaluate the average photon density in function of depth and radius when a source of photons is located in the middle of the air gap, just as the metal bar is. In fact, a reflecting bar can be considered as a photon source and the term $T_{v_p\to d}(t)$ is determined by the Monte Carlo simulation considering the photon density shown in figure 5.20 (b) in which the photodetector is located on the phantom surface ($d_d = 0$) at a radius calculated by the software with

respect to each voxel. Then, the found value has to be multiplied by the reflectivity factor R = 0.5.

3) The voxel $v_p$ is located in the bar shadow. In this case the voxel contribution is evaluated as the case 1, considering the photon density shown in figure 5.20 (a) and assuming the reciprocity principle to calculate the two terms that express the total transport. Then, the resulting values are multiplied by a factor to reduce the contribution, because of the low amount of photons reaching the considered voxels and the low amount of photons returning to the surface at the photodetector. To determine which voxels are involved, geometrical considerations have been made taking into account the dimension and the position of the bar, in order to obtain qualitative prediction of photodetectors signals and the chosen factor is F = 0.8.

Figure 5.23 shows the output of three different simulations in which a photodetector signal is predicted in different cases characterized by the reciprocal position of light source and photodetector with respect to the moving bar. The red circle and the blue square represent the NIR light source and the photodetector respectively, both located on the phantom surface. The 0.5 cm width bar, moving from the left to the right in the air gap at 4.5 cm depth, is represented in grey. For each instant, corresponding to a position of the bar in the phantom, the variation of the photocurrent signal of a photodetector is calculated by means of equation (5.3).

The signal variation values obtained are resulting from assumptions and approximations about the evaluation of the geometrical extension of the casted shadow with respect to the bar dimensions, as well as the choice of F factor value. However, these considerations allow having a qualitative forecast of the photodetector signals trends in the presented system tested on a multilayered phantom with a partially reflecting bar moving in the air gap. The expected signals in function of the position of the bar are reverse bell shaped and when the bar is located at the same distance from the light source and from the detector, the minimum occurs. The value of the minimum peak and shape of the signal variation in function the bar position (or in function of time in case of uniform motion) change a little if the direction of the bar motion has different angle with respect the straight line passing through the light source and the photodetector. The reason is to be found in the different amount of space occupied by an object in a phantom region located between the light source and the photodetector.

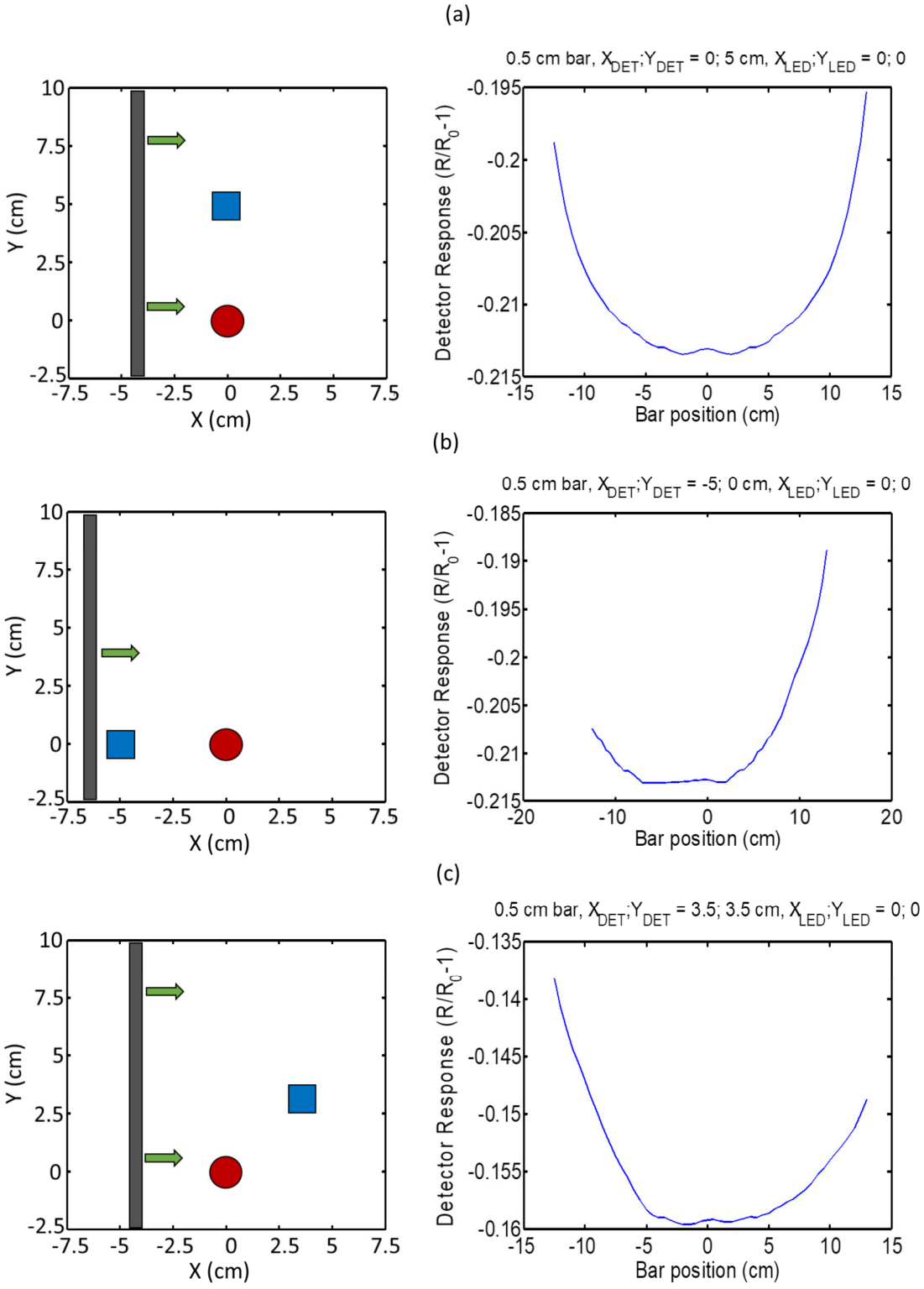


**Figure 5.23:** Reconstruction of a photodetector signal by Monte Carlo simulations. The NIR light source, and the photodetector located on the phantom surface are represented by the red circle and the blue square respectively. The 0.5 cm width bar, moving from the left to the right in the air gap at 4.5 cm depth, is represented in grey and occupies different amount of the space between the source and the detector in the 3 cases represented in a), b) and c).

## *5.9 Experimental system response to the bar motion in the dynamic phantom*

After the MC simulation of the system response reported in the previous section, in this section we report the experimental data of the system response to the bar motion in the dynamic phantom described in section 5.4. As mentioned in section 5.3, the equipment has been tested by measuring the back reflected light of 12 multiplexed double wavelength LEDs by means of 13 SiPMs. Three experiments with three different stainless steel bars of widths of 0.2, 0.5 and 1 cm were performed. The bars were moved in the air gap by a stepper motor at fixed angular velocity. 156 signals for each of the two wavelength (700 nm and 830 nm) were recorded by the system. Figure 5.24 shows the 156 calibrated signals resulting by the illumination at 830 nm when the 5 mm width bar passes in the phantom under the LEDs and SiPMs patch in the air gap. The output data file is structured in rows and columns. Each row is related to a time instant while columns are related to every single channel for both 700 nm and 830 nm illumination signals. Two further columns contain time data from the beginning of the experiment and the orientation angles of the moving bar for a total amount of data file columns of 314.

In figure 5.24 (a) the signals are shown as a function of time as they have been acquired. The minimum peaks are distributed in the test duration because of the geometry of the experiment.

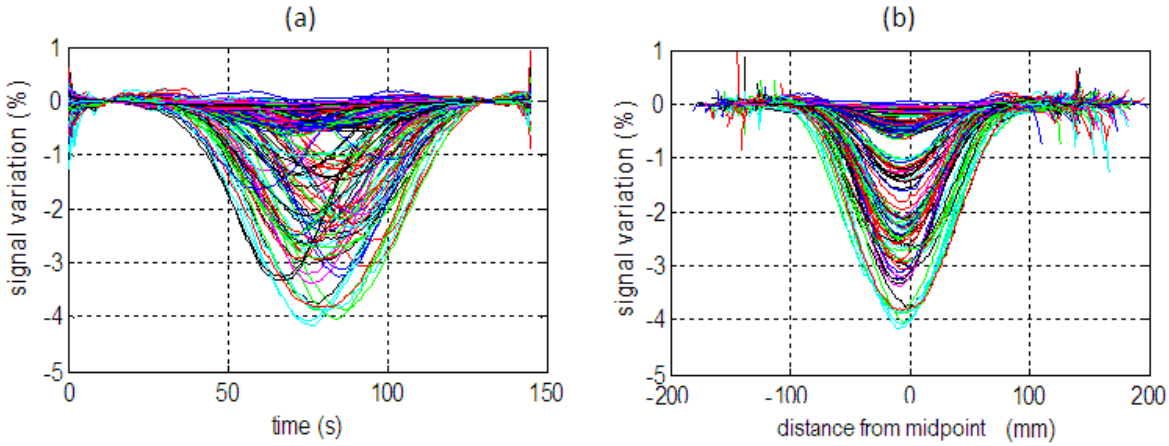


**Figure 5.24:** Plots of calibrated and filtered signals variation recorded at 156 channels:
a) signals in function of time of acquisition from the beginning of the experiment;
b) signals in function of the distance of the bar from
the mid-point between source and detector of each channel.

The previous section describes how Monte Carlo simulations have been used to foresee the qualitative signal trend of the photodetectors. The expected signals as a function of the position of the bar with respect to the optodes are reverse bell shaped with a minimum occurring when the bar passes under the mid-point between the NIR light source and the detector. By means of the angles stored in the data file, a software developed in MATLAB® reconstructs the geometry of the experiment and rearrange the signals in order to visualize them as a function of the distance of the bar from the projection of the mid-point between the source and the detector of each channel. The result is shown in figure 5.24 (b), while Figure 5.25 shows a frame of the animated graphic output of this software.

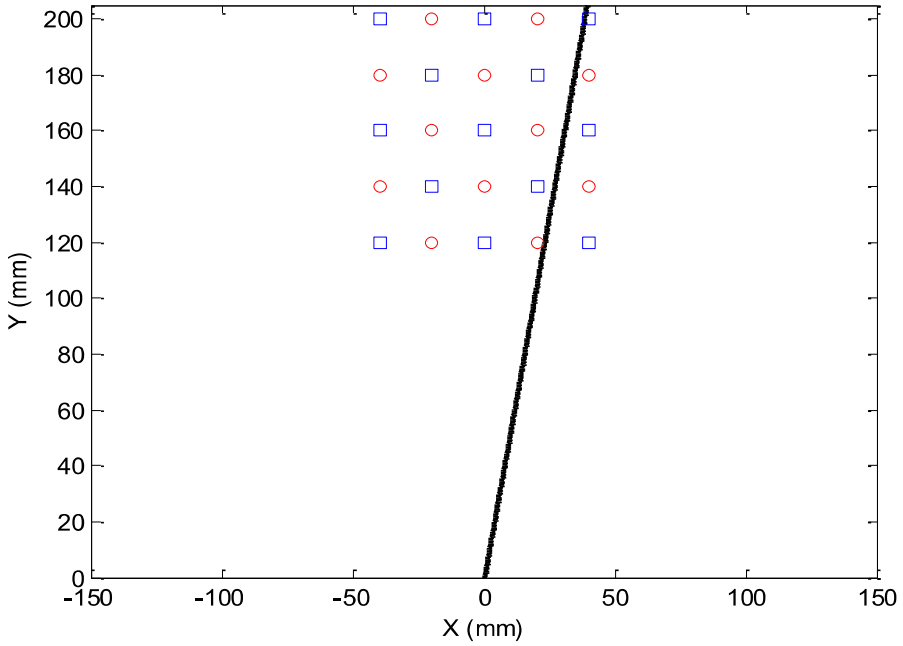


**Figure 5.25.** Frame of the animated graphic output of the MATLAB® software used to reconstruct the signals dependence by the distance of the bar from the projection of the mid-point between source and detector of each channel. Red circles represent the LEDs, while blue squares represent the SiPM detectors.

Figure 5.24 shows all the 156 channels of the system independently of their geometrical arrangement. The channels can be classified by SDS, since different behavior is expected for each SDS. In fact, when the SDS increases, the amount of photons reaching the photodetector decreases and the percentage of them that are affected by the presence of a perturbing object increases.

Figures 5.26, 5.27 and 5.28 show the calibrated and smoothed responses as a function of the distance from mid-points measured by the system channels when

three bars of the same material but of different sizes, rotate in the phantom air gap at the same angular velocity. The signals recorded by the system when a 2 mm width bar passes in the air gap are represented in figure 5.26. As intuitively expected and foreseen by the Monte Carlo simulations, the percentage variation of the signals is a reverse bell shaped, the minimum is reached when the bar is under the mid-point and the value of this minimum is related to the SDS and to the bar width. Figures 5.27 and 5.28 show the signal variations recorded when in the air gap rotate a 5 mm width bar and a 10 mm width bar respectively: the larger is the SDS, the larger is the photodetector signal percentage variation, while the larger is the bar witdth, the larger is the variation. Furthermore, the width of the reverse bell increases when the bar is larger because of the larger shadow casted.

It is important to underline that in a prototype system the output data can be considered consistent if the phenomenon that generated them is repeatable with the same results. The following images show the results of 156 independent channels observing the same phenomenon from different positions: the fact that, under the same conditions, the signals closely resemble each other and respect the predictions of the Monte Carlo simulations, assumes great importance.

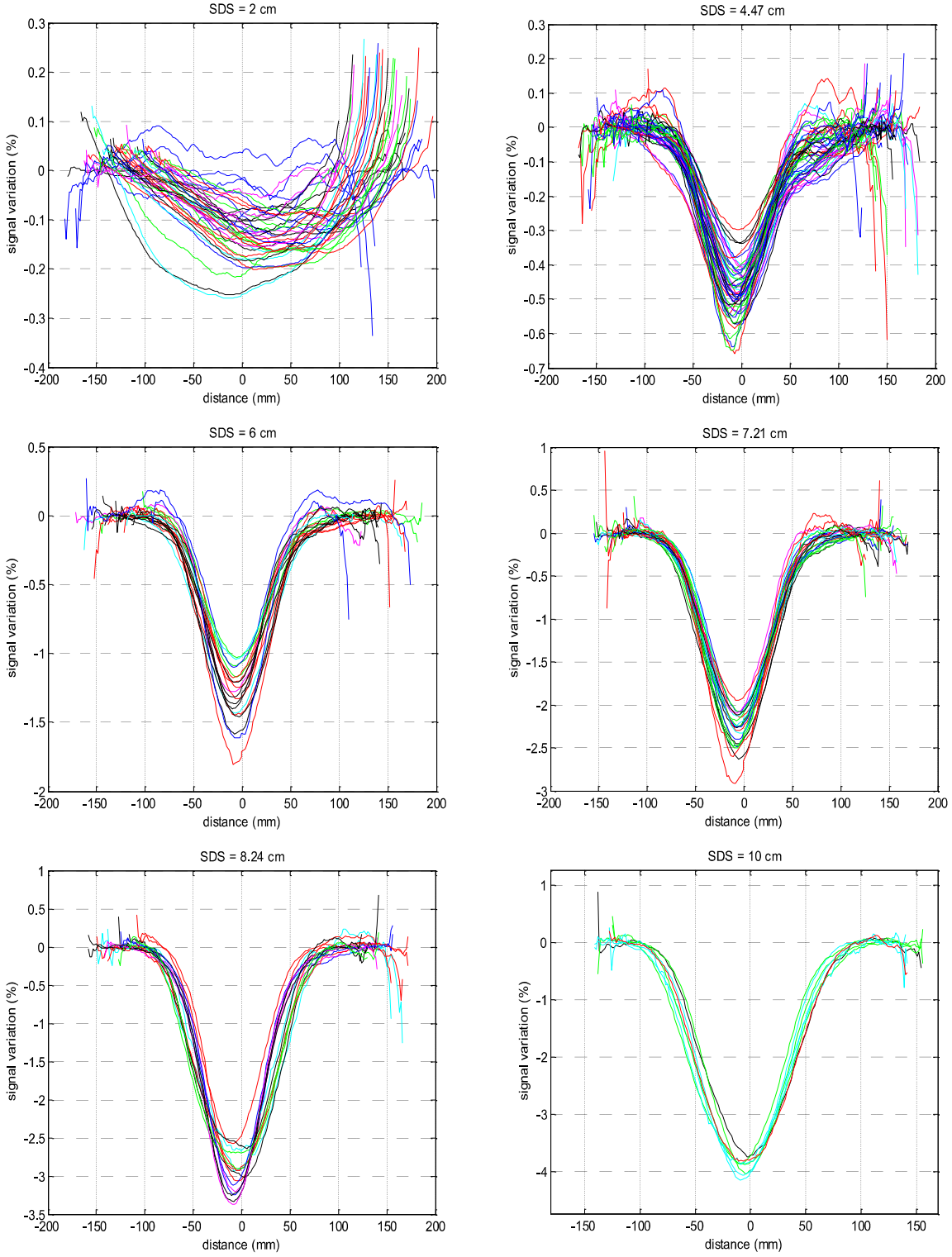


**Figure 5.26:** Signals recorded when a 2 mm width bar rotates in the air gap, classified by SDS.

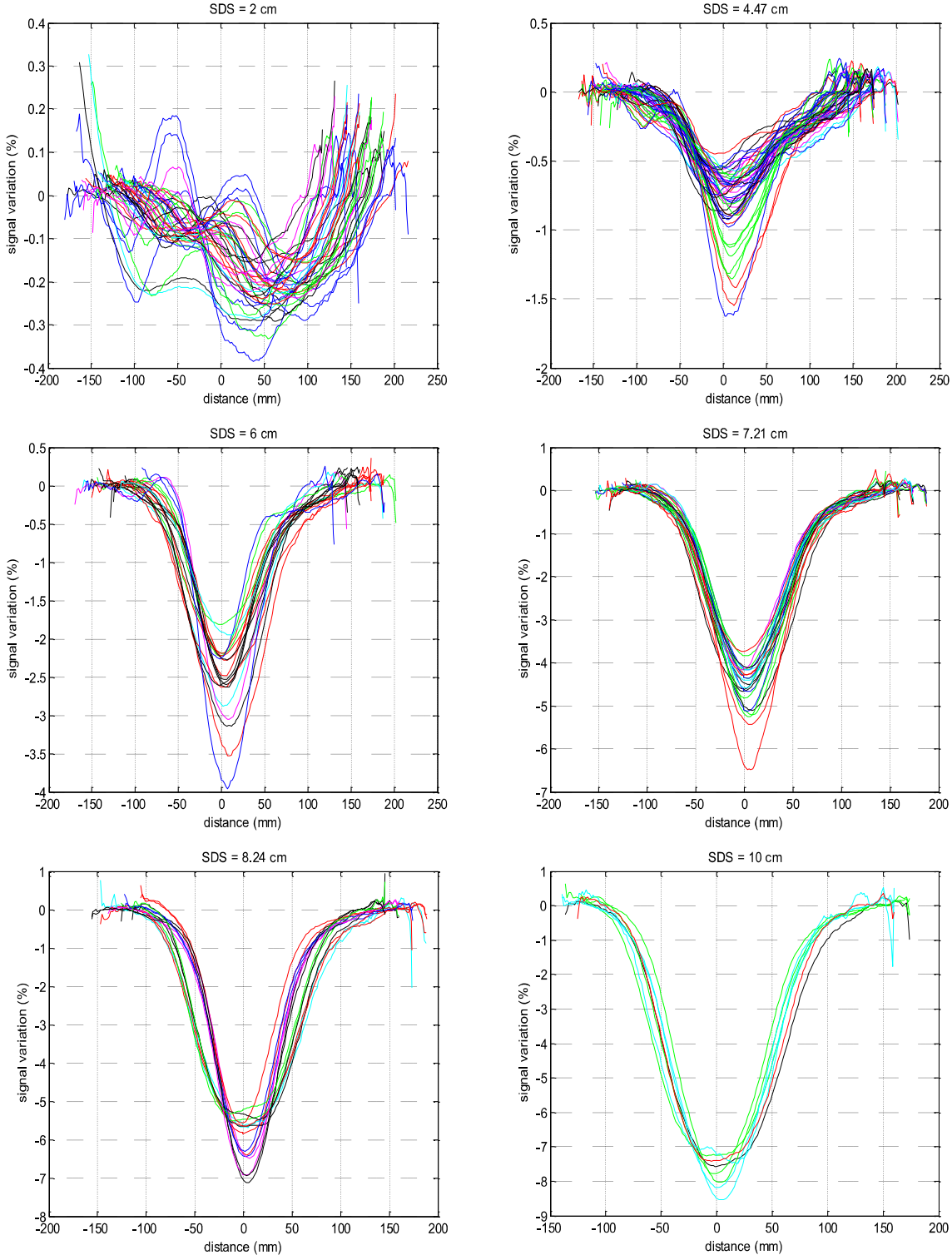


**Figure 5.27:** Signals recorded when a 5 mm width bar rotates in the air gap, classified by SDS.

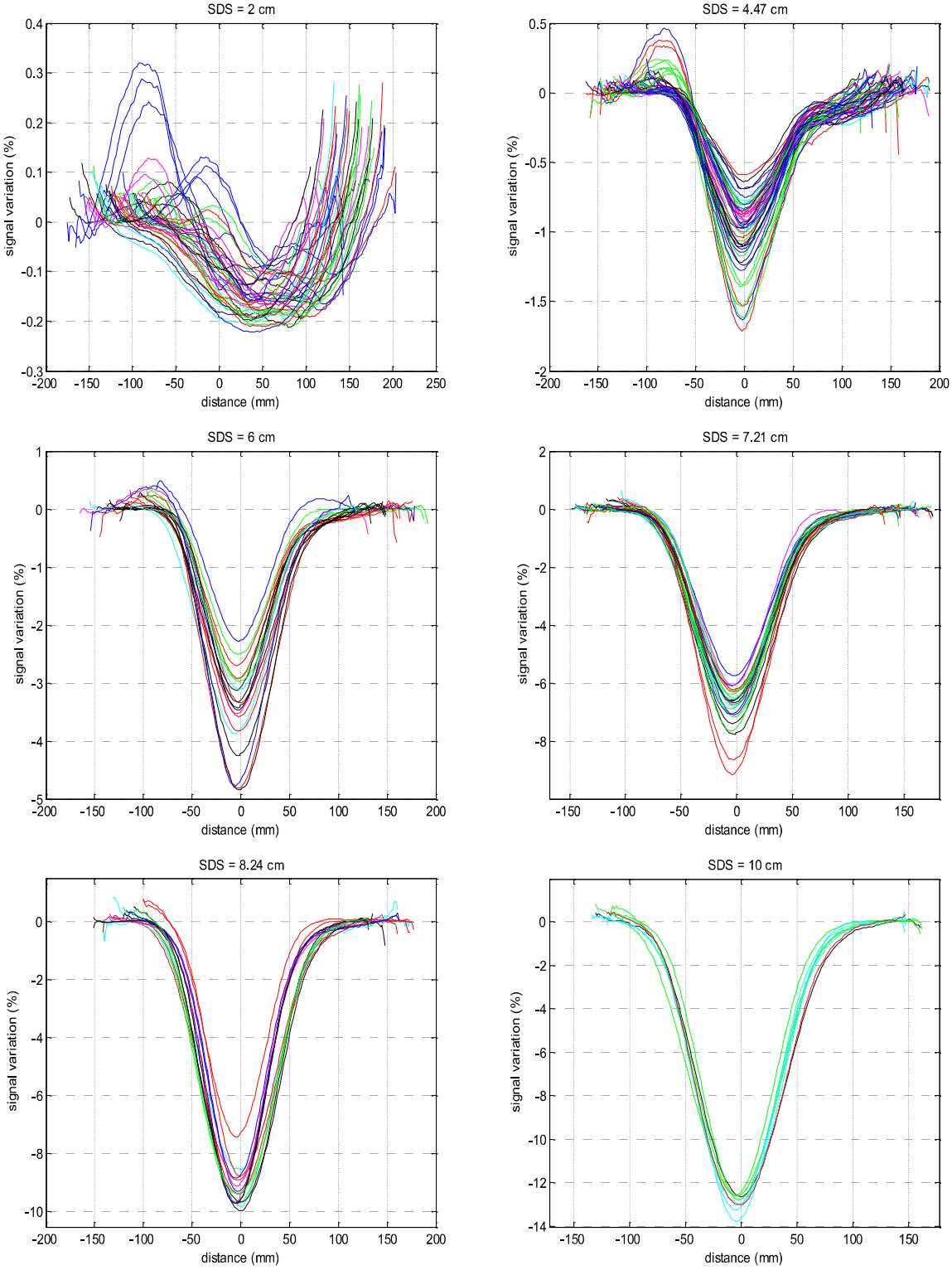


**Figure 5.28:** Signals recorded when a 10 mm width bar rotates in the air gap, classified by SDS.

The effect of light reflection is visible in figures 5.27 and 5.28 for larger bars at shorter SDSs. In case of SDS = 2 cm, the recorded photocurrents have an increase

when the bar enters in the region under illumination because of its reflectivity. However despite at SDS = 2 cm the light reflection is the main cause of the signal variation, the alteration is rather low. Considering the 5 mm and 10 mm width bars at SDS = 4.47 cm, the signals indicate a reflection effect when the bar start entering in the monitored region of the phantom, according to the Monte Carlo simulations outputs showed in figure 5.22 (a). This effect is lower and lower when the SDS increases whereas the effect of the shadow has a larger impact on the photocurrent signals.

## *5.10 Imaging*

When the medium in which light travels is not homogeneous and the volume under analysis contains air gaps, the light transport is not purely diffusive. Reflection and refraction effects can occur at internal edges and the light transport is free in the air gap. Moreover, a moving partially reflecting bar causes large variations in optical parameters in the volume under analysis. All these conditions do not respect the assumptions described in chapter 1 and 2 for the solution of the inverse problem to get tomographic images from measurements through the definition of a Jacobian.

When the variations on optical parameters are not incremental, a work around is needed to get images. The Monte Carlo simulations results and the consequent qualitative considerations on measured signals allow to state that the middle point between NIR source and detector of each channel is the space region monitored with higher sensitivity. This consideration agree with the study by Strangman, Li, and Zhang [90], asserting that for a given source-detector pair the maximum sensitivity region is located for the x and y coordinates at the mid-point, and deeper and deeper as the SDS increases. Consequently, this assertion is valid also in an inhomogeneous phantom with an air gap.

Considering the optodes configuration of the system, reported in Figure 5.1 (a), Figure 5.29 reports the x – y geometrical positions of the mid-points between the sources and the detectors involved in the measurements classified by the SDSs. For each SDS, a two-dimensional matrix is defined by using the assumptions mentioned above. Some of the source-detector paths identify the same point in the medium, to a total of 108 different observed points. In each map the observed points (black

circles), sources (red circles), and detectors (blue squares) involved in the definition of the channels are represented for each SDS.

To test the implemented imaging software, a fourth metal bar, of 1 mm width has been used, in an experiment similar to the previous ones.

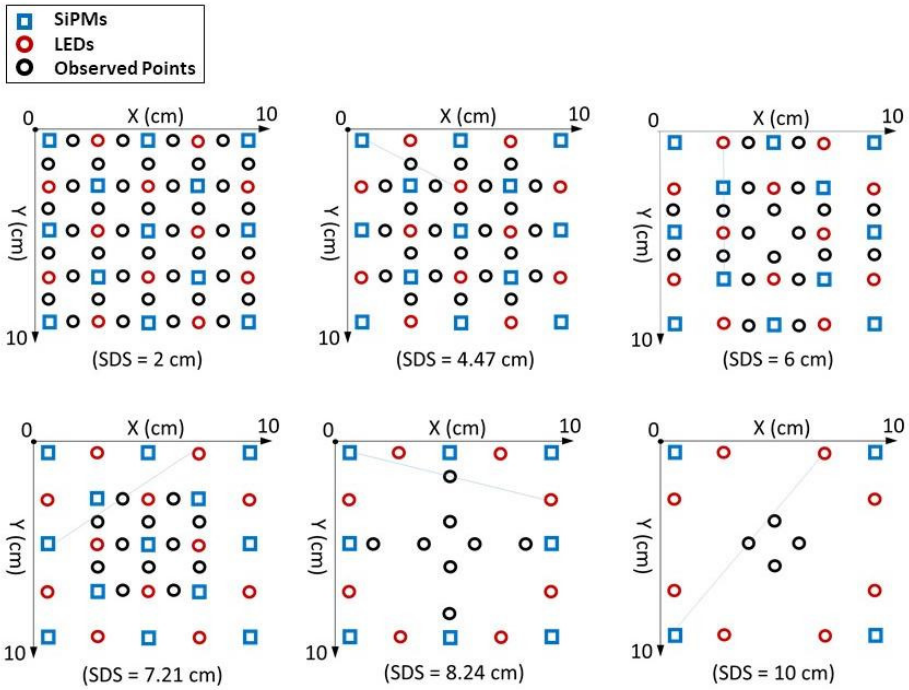


**Figure 5.29:** Maps of geometrical position of the channels mid-points (black circles) for the case of the checkerboard pattern of SiPMs (blue squares) and sources (red circles) reported in Figure 5.1.

A software developed in MATLAB® provides an arrangement of the collected photocurrents data at the two wavelengths and after the calibration. The data are displayed as a color change of pixels placed on planes classified by the SiPM / LED distances, and taking into account the geometrical positions of sources and detectors, as described above and in Figure 5.29, following a back-projection approach [91] that is a geometrical arrangement of the measurements graphic representation. Figures 5.30, 5.31, and 5.32 report examples of such images at three different time instants to give an idea of the temporal evolution of the images. The pixels represent the measured phantom regions, arranged in a two-dimensional (2D) map, and the pixel color represents the photocurrent normalized to the baseline: the green color represents the baseline, whose value is 1. The value of the color in each pixel at any time is the signal at that time divided by the baseline. Each plane is related to a particular SDS. Clearly, for the lowest SDS, since all the LED /

SiPM pairs are involved, the highest number of channels and image pixels is obtained. It should be noted that on each plane some of the pixels do not actually correspond to measurements. For such pixels, we attributed a color by performing a linear interpolation (i.e., by assigning them a color given by the average of the closest pixels). This is done only for the pixels with nearest neighbors actually measured. During the bar motion in the phantom, the photocurrents change and, as a consequence, the pixel colors change too. The time sequence of the images of a plane can be visualized as a movie, which provides the time evolution of the particular image plane. This can be repeated for each SDS and corresponding plane. Figures 9, 10, and 11 are, in fact, frames of such movies. From the figures, it is evident that the movies of each plane clearly show the localization of the metal bar, whose shape and position are smeared by its movement and by the light diffusion.

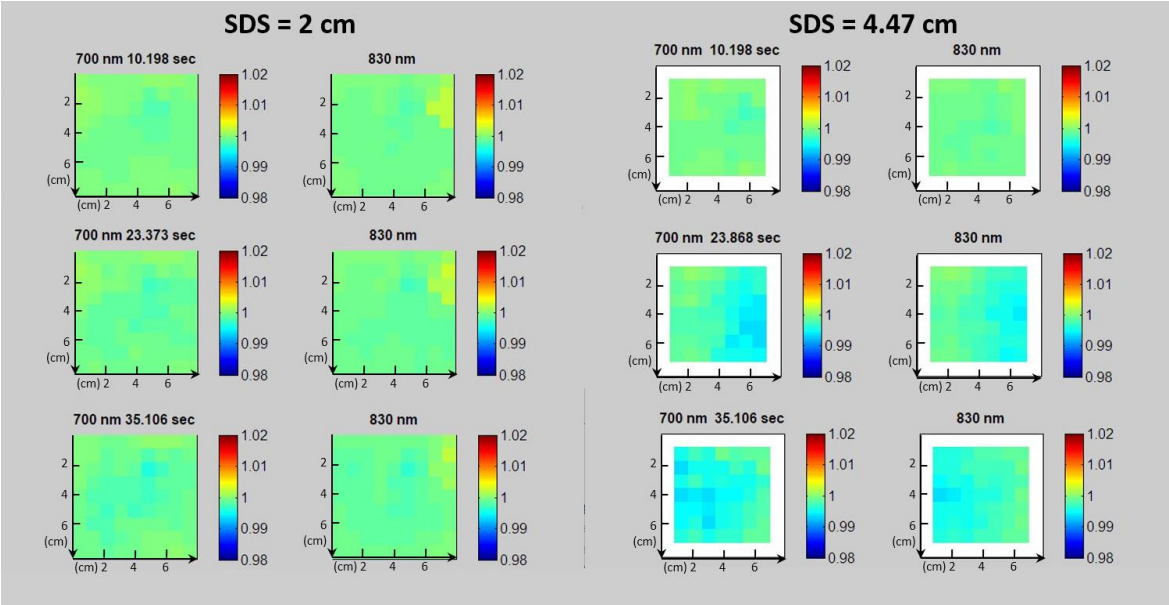


**Figure 5.30**: Back-projection images reporting the normalized photocurrents after 700 nm and 830 nm irradiation, related to three different instants for 2 cm and 4.47 cm SDSs.

For the planes defined by the SDS = 2 cm, no relevant variation is visible since the rod is moving in the phantom at a depth which is not reached by the average photons path. On the contrary, at SDS = 4.47 cm, the sequence starts to show the passage of a shadow in spatial correspondence with the bar, moving from the right to the left side of the plane. Starting from the 6 cm SDS, the sequence clearly shows the bar passage taking place in the air gap at a depth between 3 cm and 6 cm, below the first EPE layer. Moreover, since at larger SDS values the banana-shaped path of the detected light grows and becomes wider, the moving shadow of the metal bar

grows in size as the SDS increases. The signal due to the metal bar motion evidenced in Figures 5.30, 5.31, and 5.32, of the order of 1% of the baseline (i.e. 20 $log_{10}(0.01)$ = 40 dB or somewhat higher), is clearly well detected, although the bar is quite small.

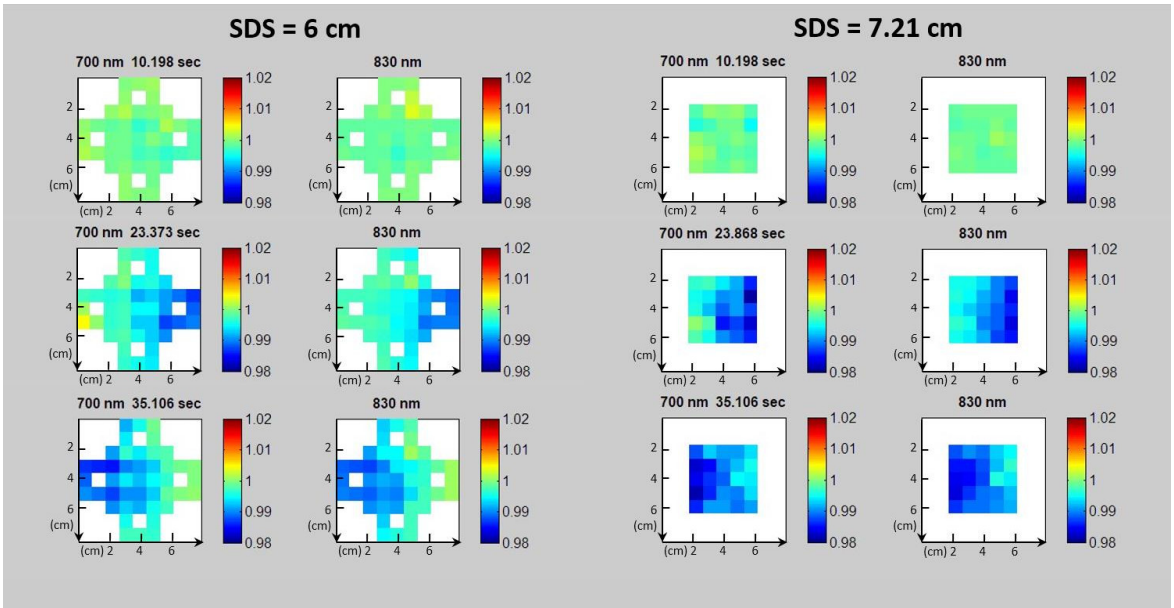


**Figure 5.31**: Back-projection images reporting the normalized photocurrents after 700 nm and 830 nm irradiation, related to three different instants for 6 cm and 7.21 cm SDSs.

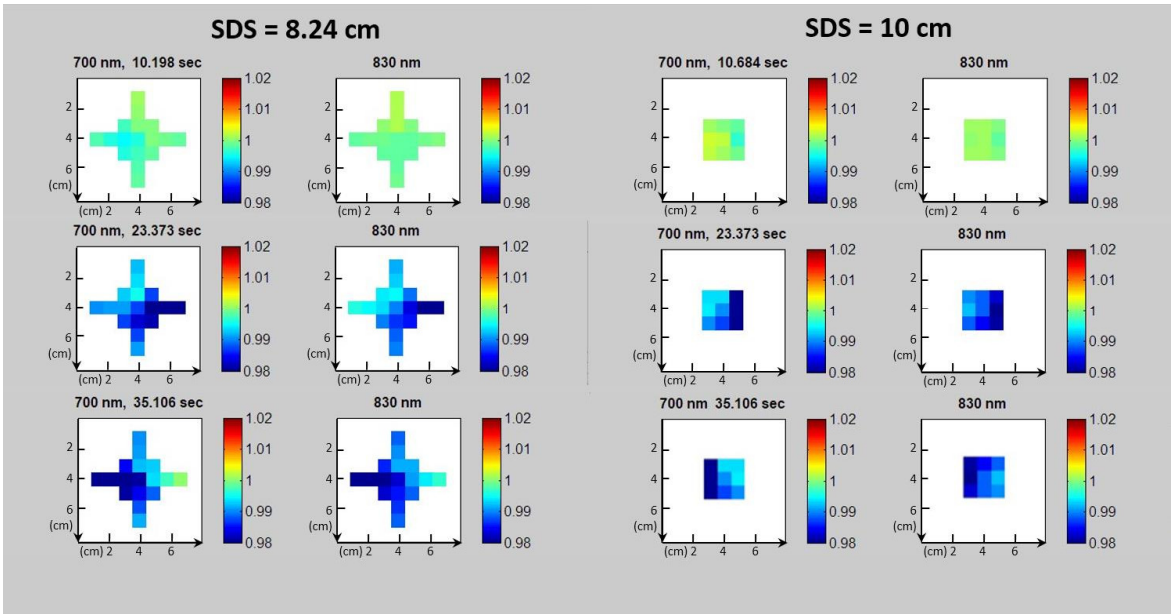


**Figure 5.32**: Back-projection images reporting the normalized photocurrents after 700 nm and 830 nm irradiation, related to three different instants for 8.24 cm and 10 cm SDSs.

In fact, it corresponds to a volume change of the order of $2 \times 10^{-4}$ (i.e., 0.02 %), estimated as the ratio of the metal rod volume divided by the total volume under test. The large ability to detect such a small volumetric change is due to the high system SNR values and the very effective calibration.

# Conclusions

The present thesis concerns a study on materials, devices, and systems for the real-time monitoring of the human cerebral cortex functional oxygenation by using Near Infrared Spectroscopy (NIRS). Such biomedical optical imaging technique is generally referred to in the literature as functional NIRS (fNIRS).

In the opening chapters of the work, considering the state of the art, a recently developed category of photodetectors has been studied, the Silicon Photomultipliers (SiPMs), capable to increase the portability and performances of fNIRS systems with the possibility of the realization of high-density light injection and collection probes, toward the development of portable and robust Diffuse Optical Tomography (DOT) systems.

The NIR light scattering and absorption are the mechanisms carrying the cortex oxygenation information, therefore the light transport in diffusive media has been studied using different approaches, from theory, to Monte Carlo simulations and experimental trials, involving steady state light intensity, and time-of-flight (TOF) measurements in different experimental conditions, using custom systems equipped with SiPMs.

This work presents simulations and characterizations of the materials constituting a multilayered inhomogeneous light scattering phantom with movable parts. The resulting considerations are the root of photodetector signals prediction in different experimental conditions, including the light transport in inhomogeneous media, in order to open the way for an extension of fNIRS and DOT techniques from human head to other areas of the human body, such as the chest, characterized by inhomogeneities and cavities similar to air gaps.

The final chapter presents the construction and characterization of a fiber-less CW imaging system prototype suitable for fNIRS/DOT imaging and equipped with 13 SiPMs and 24 LED sources capable of managing 156 double wavelength channels at six different SDSs, ranging from 2 cm to 10 cm. The SiPM signal drift is discussed proposing its compensation, and the SiPM linearity, the corrections to channel signal differences, and the SNR are the main focus of the system optimization presented in the chapter. The proposed system allows to reconstruct images representing the variations in scattering and absorption parameters at a refresh rate in the 2–5 Hz range, and to perform fNIRS analysis with a SNR between 53 dB and

70 dB within the considered SDSs. For a single channel system working at 1 Hz, the SNR can be extrapolated and according to the data reported in figure 4.12, it can be considered a value of 100 dB. That is, considering a 1 mA photocurrent recorded for 1 sec, corresponding to a current of about $6.25 \times 10^{15}$ electrons, the amount of equivalent noise electrons at 100 dB SNR is about $6 \times 10^{13}$. Considering a photodetector gain of $10^6$ and a PDE of 30% for NIR photons (according to the data showed in figure 3.7), the system noise is due to an equivalent number of photons impinging the sensors of about $2 - 3 \times 10^5$ at 1 Hz system refresh rate, a very low value.

These considerable results are due to the great performances of the used photodetectors and to the system optimizations carried out after the in-depth studies presented in this work.

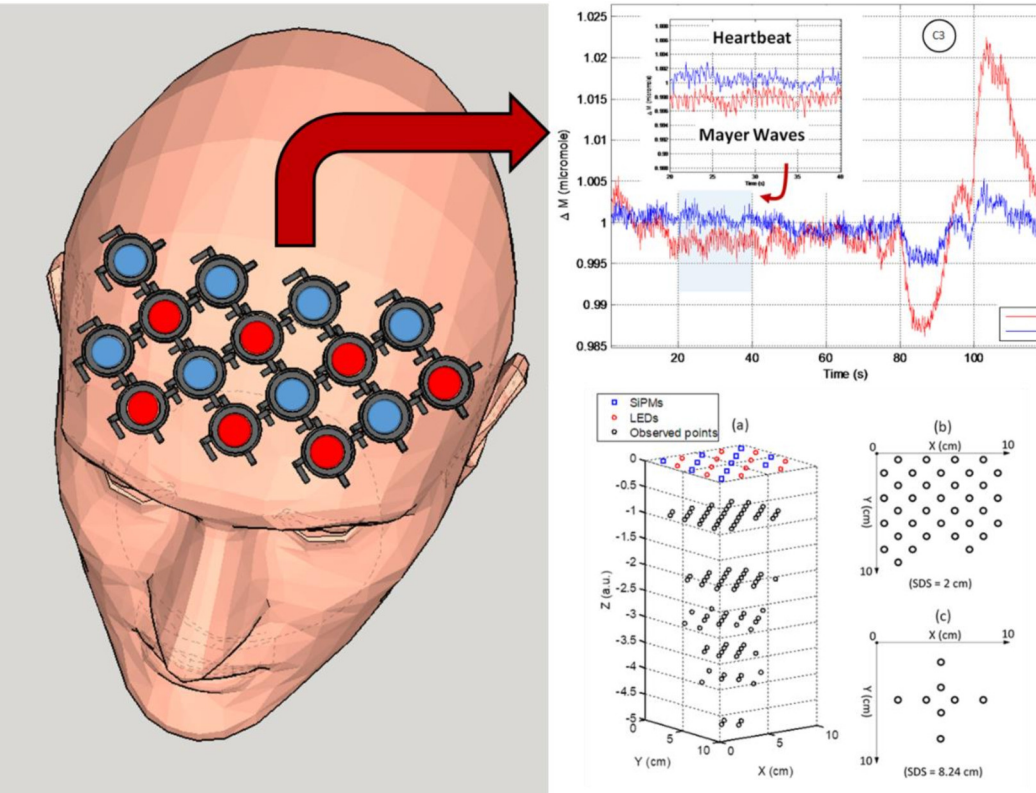


**Figure C.1:** Presentation of the proposed system published on Platinum magazine, https://platinum-online.com/post/il-caschetto-che-studia-il-cervello/ (accessed on line on Sep. 2020).

As a prerequisite for a continuation of the work in the future, a system with 18 detectors and 16 multi-wavelength light injection points has been realized, with a probe capable of covering a large area of the head and a software able to reconstruct tomographic images at different depths with a temporal resolution in the range of

2-5 Hz. Figure C.2 shows the probe prototype of this system: the sensors and LEDs holders constitute a conformable and comfortable modular cap.


**Figure C.2:** Modular High Density probe for the presented DOT system: (a) Bottom view, (b) Top view.

# Acknowledgements

Firstly, I would like to express my sincere gratitude to Dr. Salvatore Lombardo, for giving me the opportunity to work with him and his group, for putting his trust in me and in my competences, guiding me with his continuous support, patience, motivation and for teaching me some of his huge knowledge on Optics, Photonics and Semiconductor Materials.

I thank Dr. Sebania Libertino, for having involved me in important teaching activities, for encouraging me to participate in conferences, for supporting me in the drafting of papers.

A special thank goes to Dr. Giorgio Fallica from STMicroelectronics for his assistance, for the interesting scientific discussions about the development of Silicon Photomultipliers devices, and for making the photodetectors available for my work.

I want to thank Dr. Antonio Chiarelli and Dr. Arcangelo Merla, for the useful scientific discussions and for the hospitality during my visits at their institute in Chieti and Pescara in the framework of the ASTONISH project.

I would like to thank Dr. Gaetano Santoro for hosting my group in his doctor's office, for being interested in my project and for giving me an idea for the development of the graphic software interface.

I am grateful for the interest in my work shown by prof. Alfredo Ferro and his team and collaborators. During the meetings in his office, the preliminary conditions were set for a future medical experimentation of the instrument developed in this thesis.

I want to thank Dr. Giulio Bollino for assisting us with expertise in the submission of a patent conceived to exploit the best of the characteristics of the sensors used in this work.

I sincerely want to thank the Dr. Lombardo's research group and all the members of the Institute of Microelectronics and Microsystems of the Italian Research Council (CNR-IMM) of Catania. All the people have contributed to my personal and professional growth creating a profitable work environment, without renouncing to conviviality and sharing good times.

Thanks to the PhD students, post docs and fellows of the CNR-IMM for becoming my best friends and for sharing much more than a working environment.

Finally, I want to thank my parents, to whom this work is dedicated, for their help in building my future life. And thanks to my sister Alessandra, Emanuele, little Pietro and the little Flavia to make glad and delightful every day together with them.

# References


[1] Delpy, Cope, "Quantification in tissue near-infrared spectroscopy", Philos Trans R Soc Lond B Biol Sci. 1997 Jun 29; 352(1354): 649–659. doi: 10.1098/rstb.1997.0046

[2] Ito, H., Kanno, I., Fukuda, H., 2005. "Human cerebral circulation: positron emission tomography studies", Ann. Nucl. Med. 19, 65–74

[3] Scholkmann and Wolf, "General equation for the differential pathlength factor of the frontal human head depending on wavelength and age", Journal of Biomedical Optics 18(10), 105004 (October 2013)

[4] D. T. Delpy et al., "Estimation of optical pathlength through tissue from direct time of flight measurement," Phys. Med. Biol. 33(12), 1433–1442 (1988).

[5] Wray, Cope et al, "Characterization of the near infrared absorption spectra of cytochrome aa3 and haemoglobin for the non-invasive monitoring of cerebral oxygenation", Biochimica et Biophysica Acta, 933 (1988)184-192

[6] Strangman, G. E.; Li, Z.; Zhang. Q. Depth sensitivity and source-detector separations for near infrared spectroscopy based on the Colin27 brain template. PLoS One, 2013, 8(8), e66319, DOI:10.1371/journal.pone.0066319.

[7] Ferrari, Quaresima, "A brief review on the history of human functional near-infrared spectroscopy (fNIRS) development and fields of application", NeuroImage 63 (2012) 921–935

[8] Scholkmann et al. "A review on continuous wave functional near-infrared spectroscopy and imaging instrumentation and methodology", Neuroimage, 2014, 15;85 Pt 1:6-27. doi: 10.1016/j.neuroimage.2013.05.004

[9] Li, R.; Rui, G.; Chen, W.; Li, S.; Schulz, P.E.; Zhang, Y. Early Detection of Alzheimer's Disease Using Non-invasive Near-Infrared Spectroscopy. Front. Aging Neurosci., 2018, 10, 366, DOI: 10.3389/fnagi.2018.00366.

[10] Li, Y.; Jia, H.; Yu, D. Novel analysis of fNIRS acquired dynamic hemoglobin concentrations: application in young children with autism spectrum disorder. Biomed. Opt. Express., 2018, 9(8): 3694–3710, DOI: 10.1364/BOE.9.003694.

[11] Aries, M.J.; Coumou, A.D.; Elting, J.W.; van der Harst, J.J.; Kremer, B.P.; Vroomen, P.C. Near Infrared Spectroscopy for the Detection of Desaturations in Vulnerable Ischemic Brain Tissue: A Pilot Study at the Stroke Unit Bedside. Stroke, 2012, 43(4), 1134-6, DOI: 10.1161/STROKEAHA.111.636894.

[12] Stojanovic-Radic, J.; Wylie, G.; Voelbel, G.; Chiaravalloti, N.; DeLuca, J. Neuroimaging and cognition using functional near infrared spectroscopy (fNIRS) in multiple sclerosis. Brain Imaging Behav., 2015, 9, 302–311, DOI: 10.1007/s11682-014-9307-y.

[13] Obrig, H.; Villringer, A. Beyond the visible - imaging the human brain with light. J. Cerebr. Blood Flow Metab., 2003, 23, 1–18, DOI: 10.1097/01.WCB.0000043472.45775.29.

[14] White, B.R.; Culver, J.P. Quantitative evaluation of high-density diffuse optical tomography: in vivo resolution and mapping performance. J. Biomed. Opt., 2010, 15, 026006, DOI: 10.1117/1.3368999.

[15] Zeff, B. W.; White, B.R.; Dehghani, H.; Schlaggar, B.L.; Culver, J.P. Retinotopic mapping of adult human visual cortex with high-density diffuse optical tomography. Proc. Natl. Acad. Sci., 2007, 104, 12169–12174, DOI: 10.1073/pnas.0611266104.

[16] Joseph, D.K.; Huppert, T.J.; Franceschini, M.A.; Boas, D.A. Diffuse optical tomography system to image brain activation with improved spatial resolution and validation with functional magnetic resonance imaging. Appl. Opt., 2006, 45, 8142–8151, DOI: 10.1364/ao.45.008142.

[17] Koch, S. P.; Habermehl, C.; Mehnert, J.; Schmitz, C.H.; Holtze, S.; Villringer, A.; Steinbrink, J.; Obrig, H. High-resolution optical functional mapping of the human somatosensory cortex. Front. Neuroenerg., 2010, 2, 1–12, DOI: 10.3389/fnene.2010.00012.

[18] Arridge, S.R., Cope, M., van der Zee, P., Hilson, P.J., Delpy, D.T., 1985. Visualization of the oxygenation state of brain and muscle in newborn infants by near infrared transillumination. In: Bacharach, S.L. (Ed.), Information Processing in Medical Imaging. Martinus Nijhoff, Dordrecht, pp. 155–176.

[19] Arridge, S.R., van der Zee, P., Cope, M., Delpy, D.T., 1991. Reconstruction methods for infrared absorption imaging. Proc. SPIE 1431, 204–215.

[20] Eggebrecht et al., "Mapping distributed brain function and networks with diffuse optical tomography", Nat Photonics. 2014 June; 8(6): 448–454. doi:10.1038/nphoton.2014.107.

[21] Lu, Fei, "Medical hyperspectral imaging: a review", Journal of Biomedical Optics 19(1), 010901 (2014)

[22] Durduran et al., "Diffuse Optics for Tissue Monitoring and Tomography", Rep Prog Phys. 2010 July ; 73(7): . doi:10.1088/0034-4885/73/7/076701.

[23] Farina, A.; Tagliabue, S.; Di Sieno, L.; Martinenghi, E.; Durduran, T.; Arridge, S.; Martelli, F.; Torricelli, A.; Pifferi, A. and Dalla Mora, A. Time-Domain Functional Diffuse Optical Tomography System Based on Fiber-Free Silicon Photomultipliers. Appl. Sci. 2017, 7, DOI: 10.3390/app7121235.

[24] Re, R.; Martinenghi, E.; Dalla Mora, A.; Contini, D.; Pifferi, A.; and Torricelli, A. Probe-hosted silicon photomultipliers for time-domain functional near-infrared spectroscopy: phantom and in vivo tests, Neurophotonics 2016, 3, 045004, DOI: 10.1117/1.NPh.3.4.045004.

[25] Boas, D. A.; Chen, K.; Grebert, D. and Franceschini, M.A. Improving the diffuse optical imaging spatial resolution of the cerebral hemodynamic response to brain activation in humans. Opt. Lett., 2004, 29(13), 1506-1508, DOI: 10.1364/ol.29.001506.

[26] Chiarelli et al., "Combining energy and Laplacian regularization to accurately retrieve the depth of brain activity of diffuse optical tomographic data," J. Biomed. Opt. 21(3), 036008 (2016), doi: 10.1117/1.JBO.21.3.036008.

[27] Tikhonov, Arsenin, "Solutions of Ill-Posed Problems", New York: Winston, (1977).

[28] Martelli et al., "Light Propagation through biological tissue and other diffusive media", SPIE Press, USA, 2010

[29] ECE532 Biomedical Optics ©1998,2002 Steven Jacques, Scott Prahl Oregon Graduate Institute.

[30] Jacques, Pogue, "Tutorial on diffuse light transport", Journal of Biomedical Optics, 13(4), 041302 (2008)

[31] Ash et al., "Effect of wavelength and beamwidth on penetration in light-tissue interaction using computational methods", Lasers Med Sci (2017) 32:1909–1918 DOI 10.1007/s10103-017-2317-4

[32] Arridge et al., "The theoretical basis for the determination of optical pathlengths in tissue: Temporal and frequency analysis", Phys. Med. Biol. 1992, 37, 1531.

[33] Arridge et al., "Photon-measurement density functions. Part 2: finite-element-method calculations". Applied Optics. 1995; 34:8026–8037.

[34] Wang et al., "MCML-Monte-Carlo modeling of light transport in multilayered tissues", Comput. Methods Programs Biomed. 472, 131–146 1995

[35] Chiarelli et al., "Comparison of procedures for co-registering scalp-recording locations to anatomical magnetic resonance images," J. Biomed. Opt. 20(1), 016009 (2015).

[36] Von Luhmann et al., "M3BA: a mobile, modular, multimodal biosignal acquisition architecture for miniaturized EEG-NIRS based hybrid BCI and monitoring," IEEE Trans. Biomed. Eng. 64, 1199–1210 (2016).

[37] Particle Data Group, "Particle detectors for accelerator", http://pdg.lbl.gov/2009/reviews/rpp2009-rev-particle-detectors-accel.pdf.

[38] Muehlemann, Haensse, and Wolf, "Wireless miniaturized invivo near infrared imaging," Opt. Express 16(14), 10323–10330 (2008).

[39] Pinti et al., "Using fiberless, wearable fNIRS to monitor brain activity in real-world cognitive tasks," J. Visualized Exp. 106, e53336 (2015).
[40] Piper et al., "A wearable multi-channel fNIRS system for brain imaging in freely moving subjects," Neuroimage 85(Pt 1), 64–71 (2014).
[41] Di Sieno, et al., "A. Toward non-invasive assessment of flap viability with time-resolved diffuse optical tomography: a preclinical test on rats", J. Biomed. Opt., 2016, 21(2), 25004.
[42] Buzhan et al., "Silicon photomultiplier and its possible applications," Nucl. Instrum. Methods Phys. Res. Sect. A 504(1–3), 48–52 (2003).
[43] Santangelo et al., "Si photomultipliers for bio-sensing applications," IEEE J. Sel. Top. Quantum Electron. 22(3), 335–341 (2016).
[44] Zimmermann et al., "Silicon photomultipliers for improved detection of low light levels in miniature near-infrared spectroscopy instruments," Biomed. Opt. Express 4(5), 659–666 (2013).
[45] Re et al., "Probe-hosted silicon photomultipliers for time-domain functional near-infrared spectroscopy: phantom and in vivo tests," Neurophotonics 3(4), 045004 (2016).
[46] Pagano et al., "Improvement of sensitivity in continuous wave near infra-red spectroscopy systems by using silicon photomultipliers," Biomed. Opt. Express 7(4), 1183–1192 (2016).
[47] Sciacca et al., "Silicon Planar Technology for Single-Photon Optical Detectors", IEEE Transactions On Electron Devices, Vol. 50, No. 4, APRIL 2003
[48] Cova et al., "Avalanche photodiodes and quenching circuits for single photon detection," Appl. Opt., vol. 35, pp. 1956–1976, 1996.
[49] Hurkx et al., "A new analytical diode model including tunneling and avalanche breakdown," IEEE Trans. Electron Devices, vol. 39, Sept. 1992.
[50] Oldham et al., "Triggering phenomena in avalanche diodes," IEEE Trans. Electron Devices, vol. ED-19, pp. 1056–1060, 1972.
[51] Cova et al., "Trapping phenomena in avalanche photodiodes on nanosecond scale," IEEE Electron Device Lett., vol. 12, pp. 685–687, 1991.
[52] On Semiconductor, "Introdiction to the Silicon Photomultiplier (SiPM)", Available online: https://www.onsemi.com/pub/Collateral/AND9770-D.PDF (accessed on Aug, 30, 2020)
[53] Pagano et al., "Dark current in SiPM pixels: data and model", IEEE Transaction on Electron Devices 59(10):2410 (J. 2012)
[54] Du, Retrière, "After-pulsing and cross-talk in multi-pixel photon counters", Nuclear Instruments and Methods in Physics Research A 596 (2008) 396–401
[55] Pagano et al., "Improvement of sensitivity in continuous wave near infra-red spectroscopy systems by using silicon photomultipliers"Biomed. Opt. Expr. 7(4), 1183-1192, 2016

[56] Chiarelli et al., "Flexible CW-fNIRS system based on Silicon Photomultipliers: In-Vivo characterization of sensorimotor response", Neurophotonics, 4(3):035002, (2017) doi: 10.1117/1.NPh.4.3.035002
[57] Mazzillo et al., Electro-Optical Performances of p-on-n and n-on-p Silicon Photomultipliers. IEEE Trans. Electron Devices, vol. 59, pp. 3419–3425., 2012
[58] Mazzillo et al., "Noise Reduction in Silicon Photomultipliers for Use in Functional Near-Infrared Spectroscopy", IEEE Trans. Radiat. Plasma Med. Sci. vol 1, pp. 212-220, 2017.
[59] Mazzillo et al., "Electro-Optical Characterization of SiPMs With Green Bandpass Dichroic Filters", IEEE sensors Journal 17(13), 4075 – 4082, 2017 IEEE Trans. on Rad. and Med. Plasma Sci. 1(3), 212-220
[60] Wyser, et al., "Wearable and modular functional nearinfrared spectroscopy instrument with multidistance measurements at four wavelengths," Neurophotonics 4(4), 041413 (2017).
[61] M. Mazzillo, et al., "Electro-optical performances of p on n and n on p Silicon Photomultipliers," IEEE Trans. El. Dev. 59(12), 3419–3425 (2012).
[62] Nagy et al., "Afterpulse and delayed crosstalk analysis on a STMicroelectronics silicon photomultiplier," Nucl. Instrum. Methods Phys. Res. A 759, 44–49 (2014).
[63] Rosado et al., "Modeling crosstalk and afterpulsing in silicon photomultipliers," Nucl. Instrum. Methods Phys. Res. A 787, 153–156 (2015).
[64] Ward and Vacheret, "Impact of after-pulse, pixel crosstalk and recovery time in multi-pixel photon counter response," Nucl. Instrum. Methods Phys. Res. A 610(1), 370–373 (2009)
[65] Wêgrzecka et al., "Design and Properties of silicon avalanche photodiodes," Opto-Electron. Rev. 12(1), 95–104 (2004).
[66] A. Luque and S. Hegedus, Handbook of Photovoltaic Science and Engineering (Wiley, 2003)
[67] Roulston et al., "Modeling and measurement of minority carrier lifetime vs. doping in diffused layers of n+/p Si diodes," IEEE Trans. El. Dev. 29(2), 284–291 (1982).
[68] Klaassen, "A unified mobility model for device simulation - II Temperature dependence of carrier mobility and lifetime," Sol. St. Elect. 35(7), 961–967 (1992).
[69] Fossum and D. S. Lee, "A physical model for the dependence of carrier lifetime on doping density in nondegenerate Si," Sol. St. Electr. 25(8), 741–747 (1982).
[70] Dalla Mora, et al., "Memory effect in silicon time-gated single-photon avalanche diodes," J. Appl. Phys. 117(11), 114501 (2015).

[71] "Thermal Resistance Theory and Practice," Special Subject Book, January 2000, Infineon technologies, https://www.infineon.com/dgdl/smdpack.pdf?fileId=db3a304330f6860601311905ea1d4599 (accessed on line in Aug. 2020).
[72] Pagano et al., "Dark Current in Silicon Photomultiplier Pixels: Data and Model", IEEE Trans. Electron Devices, 2012, 59, 2410, DOI: 10.1109/TED.2012.2205689.
[73] Adamo, et al., "Silicon Photomultipliers Signal-to-Noise Ratio in the Continuous Wave Regime," IEEE J. Sel. Top. Quantum Electron. 20(6), 284 (2014).
[74] Mazzillo et al. "Noise Reduction in Silicon Photomultipliers for Use in Functional Near-Infrared Spectroscopy," IEEE Trans Radiat Plasma Med Sci. 1(3), 212–220 (2017).
[75] Maira et al., "Crucial aspects for the use of silicon photomultiplier devices in continuous wave functional near-infrared spectroscopy", Biomed Opt Express, 2018, 9(10): 4679–4688, DOI:10.1364/BOE.9.004679
[76] Zijlstra et al., "Visible and Near Infrared Absorption Spectra of Human and Animal Haemoglobin: Determination and Application", CRC Press: Zeist, The Netherlands, 2000.
[77] Maira et al., "Imaging System Based on Silicon Photomultipliers and Light Emitting Diodes for Functional Near Infra-Red Spectroscopy", Appl. Sci. 2020, 10, 1068; doi:10.3390/app10031068
[78] On Semiconductor MICROFJ-60035 Datasheet. Available online: www.onsemi.com/pub/Collateral/MICROJ-SERIES-D.PDF (accessed on Sep, 2020)
[79] Sá et al., "Junction Temperature Estimation for High Power Light-Emitting Diodes", Proceedings of the IEEE International Symposium on Industrial Electronics, Centro Cultural and Social Caixanova, Vigo, Spain, June 4-7, 2007, Piscataway, N.J.: IEEE. DOI: 10.1109/ISIE.2007.4375098.
[80] Waterworth et al., "Optical transmission properties of homogenized milk used as a phantom material in visible wavelength imaging," Australas. Phys. Eng. Sci. Med. 18(1), 39–44 (1995).
[81] Cubeddu et al., "A solid tissue phantom for photon migration studies", 1997 Phys. Med. Biol. 42 1971
[82] Becker, "Advanced time-correlated single-photon counting techniques", Springer, Berlin, Heidelberg, New York, 2005
[83] O'Connor, Phillips, "Time-correlated single photon counting", Academic Press, London (1984)
[84] Becker, "The BH TCSPC Handbook, Seventh edition", Becker & Hickl GmbH (2017)

[85] On Semiconductior, "Silicon Photomultipliers (SiPM), Red-Enhanced Second Generation" Semiconductor Components Industries, LLC, 2018, available on line: https://www.onsemi.com/pub/Collateral/MICRORB-SERIES-D.PDF (accessed on Sep.,2020)

[86] Chiarelli et al., "Low resolution mapping of the effective attenuation coefficient of the human head: A multi-distance approach applied to high-density optical recordings", Neurophotonics, 2017, 4, 021103, DOI: 10.1117/1.NPh.4.2.021103.

[87] Fang and Boas, "Monte Carlo simulation of photon migration in 3D turbid media accelerated by graphics processing units", Optics Express Vol. 17, Issue 22, pp. 20178-20190 (2009), DOI: 10.1364/OE.17.020178

[88] Marshall et al., "Characterization of the Reflectivity of Various Black Materials", Proceedings Volume 9147, Ground-based and Airborne Instrumentation for Astronomy V; 91474F (2014), DOI:10.1117/12.2056729

[89] Yao et al., "Direct approach to compute Jacobians for diffuse optical tomography using perturbation Monte Carlo-based photon "replay"", Biomedical Optics Express Vol. 9, Issue 10, pp. 4588-4603 (2018), DOI: 10.1364/BOE.9.004588

[90] Strangman, Li, and Zhang, "Depth sensitivity and source-detector separations for near infrared spectroscopy based on the Colin27 brain template".PLoS One, 2013, 8(8), e66319, DOI: 10.1371/journal.pone.0066319.

[91] Franceschini et al., "On-line optical imaging of the human brain with 160-ms temporal resolution", Opt. Express, 2000, 6(3), 49-57, DOI: 10.1364/OE.6.000049.